Anchoring Location of Triple Flame under Acoustic Oscillations
(音響振動を受けるTriple Flameの保炎位置)

January, 2015

Aerospace Engineering Major
Graduate School of Science and Technology
Nihon University
Masanori SAITO

Contents

1. Introduction

1.1. Review of studies

1.1.1. Combustion studies in oscillating field

Combustion instability is one of the harmful phenomena in combustion chambers of rockets or jet engines. Combustion instabilities lead to strong pressure oscillations. The oscillations can break engines or melt combustion chambers by strong pressure vibration forces or increase in heat transfer. The frequency differs with driving mechanisms and its range is from tens of hertz to several kilohertz [1]. For example, F-1 engine of Saturn rocket generates the combustion instabilities with amplitudes up to 100 % of the mean combustor pressure with frequencies in the 200-500 Hz range [2]. In the combustion chamber T-170/180 of the RD-216 engine with nitric acid/unsymmetric dimethylhydrazine (UDMH) generates acoustic oscillations of the first tangential mode with a frequency of 1200 Hz [3]. Reheater of the jet engine generates the reheat buzz which is a kind of low frequency (50-150 Hz) combustion instability [4].

The first combustion oscillation was reported by Higgins [5] as “Singing flame,” which is generated when the hydrogen diffusion flame was formed in a closed or open-ended vertical tube. Rijke [6] reported that the self- excited oscillation is generated by inserting heated metal gauze in open-ended tube, which is known as “Rijke tube.” He also found that the oscillation is generated if the location of the hot gauze is in the lower half of the tube. This implies that the heating position is an essential factor to determine the generation of self-excited oscillation.

The first criterion of the generation of combustion oscillation is propounded by

Rayleigh [7,8] as,

$$\int_V \int_T p'\dot{q}'dtdV > 0 \tag{1.1.1}$$

where p' is the pressure fluctuation, $\dot{q}'$ is the heat release rate fluctuation, V stands for the flow domain and T is the oscillation period. If the condition in the combustion chamber satisfies the criterion, the combustion instability occurs, otherwise it attenuates. Rayleigh criterion implies that the flame position in the combustion chamber signifies to predict the generation of combustion instability. Therefore, many researches about flame position, flame speed or heat release in pressure oscillating field have been conducted.

The first systematic experimental study of single-droplet combustion in oscillating field was conducted by Kumagai and Isoda [9]. They clarified that the burning velocity of single fuel droplet increases in vibrating air field. Tanabe et al. [10,11] observed the flame stretching toward the velocity node by standing acoustic wave with microgravity condition. They interpret their observation of flame deformation due to an acoustic radiation force driven by the interaction between the velocity fluctuation and the density difference between the hot gas and the cold surrounding medium. Further investigations of influence of acoustic waves on a fuel droplet or droplet pairs were conducted by some researchers [12–14]. As mentioned above, some reliable models about the effect of acoustic oscillations on the simple combustion systems such as a sustained fuel droplet exist.

Other researchers have investigated the combustion oscillation using burner flame. They considered the heat release, its response to the pressure fluctuation that is phase lag and so on. Schimmer and Vortmeyer [15] verified the self-excited acoustic oscillations using flat flame, focusing on the coupling of the heat loss fluctuation to the burner due to the oscillation of the flow velocity and pressure. They also have established the stability diagram of the combustion oscillations with different oscillation period and equivalence ratio of the mixture. Fleifil et al. [16] have constructed the analytical model to describe the heat release response of the laminar premixed flame in a velocity oscillating field. Durox et al. [17] investigated the the change in flame shape by using conical burner flame under oscillating flow. Rosdzimin et al. [18] clarified the flame response to the oscillating equivalence ratio.

Recently, Fujita et al. [19] proposed the transition criteria for the initiation of the transition to the instability. They apply the laser irradiation to the premixed flat flame and investigate the transition process from the disturbed flame structure to the corrugated flame structure.

As the improvement of the performance of computers has been accelerated in 2000s, the analysis of the combustion instabilities using computational fluid dynamics (CDF) is being conducted. Hantschk and Vortmeyer [20] simulated self-excited combustion oscillations by using CDF. They computed the self-excited pressure oscillation and calculated the local Rayleigh index.

There are many other studies [21–23] on the heat release response, flame shape, flame speed and others in the oscillating field by experiment or CFD. Rayleigh's theory, to some extent, contributes in the prediction of the combustion instabilities.

Purdue University's group investigate the combustion instability in a condition close to a practical rocket combustor applying the Continuously Variable Resonance Combustor (CVRC), which can vary the length of the oxidizer tube and resonance mode [24–28]. Yu et al. [24], for example, investigated the combustion instability mode shape with different gaseous fuels and oxidizer tube length. Huang et al. [27] analysed the self-excited longitudinal combustion instabilities using proper orthogonal decomposition (POD) and dynamic mode decomposition (DMD). Their researches mainly aim combustion oscillation mode or onset of it.

1.1.2. Triple flame

In actual combustors, triple flame is frequently observed. Triple flame is formed in a mixing layer between fuel and oxidizer, which has a broad flammability limit. Triple flame or triple flame-like structure is formed in the leading edge of lifted diffusion flames [29–32]. Besides, it is clarified that the triple flame is the base structure of the diffusion flames in the rocket combustor by numerical simulation [33–35].

Originally, the study on triple flame was launched to assess the likelihood of a coal-dust explosion which is initiated by layered methane gas at a roof of coal mines [38]. The schematic of the triple flame is shown in Fig. 1-1-1. The flame is constructed of an upward bending fuel-rich premixed flame, an bending fuel-lean premixed flame and diffusion flame between two premixed flames where the excess fuel and oxidizer cannot be consumed in the rich and lean premixed flame respectively. The burning velocity of the premixed flame is defined as the propagation speed of the flame relative to the unburned gas velocity. If the flame is steady in the coordinate system at rest, burning velocity is equal to the unburned gas velocity as shown in the figure. For the reason stated above, the burning velocity of the triple flame is generally defined as the unburned gas velocity just ahead of the leading edge of the triple flame [36]. Since the burning velocity of the premixed flame is the fastest with near the stoichiometric mixture, the mixture fraction of the unburned gas flowing into the leading edge, whose location is the most upstream, is near stoichiometry [37]. A number of experimental investigations on the burning velocity of the triple flame have been done.

The early experimental investigation has been conducted by Phillips [38] who investigated the influence of the depth of methane gas layer on the flame propagation speed with laboratory scale models of coal mine's roof to obtain information the mine explosions. Liebman et al. [40] investigated the flame speed including the effect of the gallery confinement. Since the leading edge of the triple flame is premixed flame, the theoretical analysis have been basically conducted as a propagating premixed flame which is subject to the flow divergence due to heat release and flame curvature [41] with the mixture fraction along the flame surface changes. Dold [42] demonstrated that a relationship exists between the propagation velocity of a triple flame and the transverse mixture gradient by asymptotic analysis with one-step reaction. Kioni et al. [43] investigated the strain rate effect by directing a fuel and oxidizer stream towards each other.

Another unique characteristic of triple flame is flame interaction between premixed flame and diffusion flame [37, 44]. Hirota et al. noted that the steeper fuel concentration gradient yields the heat interaction between diffusion flame and premixed flame since the distance between two flames becomes close [44]. This is also presented by numerical simulation [45]. There are many other preceding studies on the flame propagation speed of triple flame associated with flame curvature or fuel concentration gradient [36, 39, 46–54].

Recent studies [39, 50–55] show that the critical concentration gradient at which the burning velocity of triple flame is maximized exists. Hirota et al. [39] measured the flow field by PIV and theoretically clarified that the critical flame curvature (or fuel concentration gradient) can be explained by overall stretch rate which is divided into a hydrodynamic effect and a curvature effect [56].

The study on the triple flame is mainly to investigate the basic characteristics such as burning velocity, flame curvature, structure including reaction [57–60]. However, the investigations of acoustical influence on the triple flame have not been conducted.

1.1.3. Studies on the mixing layer, jet and transport under acoustic excitation

When the triple flame is formed in acoustic field, upstream jet is also oscillated and fuel concentration gradient is also affected by oscillation. There are some studies on the effect of acoustic excitation on the upstream flow. Chao and Jeng [61] investigated the flame base positions of the lifted jet diffusion flame under acoustic excitation. They noted that the lift-off height of the flame base can vary due to change in the position of the roll-up vortex by acoustic excitation. Hirota et al. [62] examined the applying a high-frequency (20 kHz) standing wave to a methane-air coaxial jet upstream of a lifted jet flame. They found that the jet is inclined by the standing wave and the stability limit of the lifted flame is improved. Suzuki et al. [63, 64] found the bifurcation of the jet diffusion flames and they suggested that the flame bifurcation occurs by bifurcation of the jet, which can be explained by the probability density distribution of the oscillating jet [65]. However, these works do not reveal the effect of sound on fuel concentration gradient and flame curvature, which are the basic characteristics determining the propagation speed of the triple flame. Although some other studies about the effect of oscillation on the jet or its mixing layer [66–71] have been conducted, no reliable and beneficial models for predicting the triple flame behavior in acoustic field are demonstrated.

1.2. Objectives

This study aimed to clarify the effect of the fluid oscillation yielded by acoustic oscillation on the lift-off height of triple flame, focusing on the shape of mixing layer and fuel concentration gradient. As shown in the classical theory [72], the lift-off height is determined by the balance between burning velocity and unburned gas velocity. Therefore, the unburned gas velocity of cold flow is uniform along the streamwise, the lift-off height can be controlled by change only in fuel concentration gradient. This condition is appropriate for the validation of the effect of the acoustic oscillation on the lift-off height change yielded by change in the fuel concentration gradient. Besides, two-dimensional mixing layer is necessary for simple analysis. To satisfy these requirements, multi-slot burner whose configuration is designed based on the Hirota's work [39] is employed. The present study is conducted along with the following process.

1. I confirm the lift-off height change without sound by change in the fuel concentration gradient to confirm the lift-off height of the triple flame to be determined only by fuel concentration gradient in this experimental environment.

2. The lift-off height change with sound is measured with various sound pressures. The tendency of the lift-off height response to the sound pressure is clarified.

3. The shape of the mixing layer and fuel concentration gradient are modeled and the trend of lift-off height change is predicted with various sound pressures and frequencies. The shape of the mixing layer is observed by introducing schlieren technique. The validity of the model is investigated to compare the fuel concentration gradient calculated by the model with that calculated by numerical simulation.

1.3. Organization

This thesis consists of seven Chapters. The motivation of this study and the review of the preceding studies are dealt with here in Chapter 1, which illustrates how this thesis contains its originality and novelty in the field of combustion instability.

In Chapter 2, experimental set up and procedures are described. The basic characteristics of the experimental apparatus such as flow distributions and turbulence intensities are described. Each definition method is also explained.

The numerical simulation is carried out to investigate the detail of change in the fuel concentration gradient. Two types of simulation are performed. One is to give the flow and pressure oscillation of sine function, which is simulates the similar situation of the experiment; the other is not to give the flow as an initial condition. The oscillation of the mixing layer is simulated by setting the sine wave boundary between the mixture and air initially. In Chapter 3, computational domain, numerical method and the relation used for calculation of each transport coefficient are presented.

Investigation of the lift-off height and flame curvature without sound is conducted in Chapter 4. The lift-off height and flame curvature of triple flame are investigated by some researchers and it was found that the lift-off height is determined by the flow speed and fuel concentration gradient. If the flow speed does not change along streamwise, the lift-off height should be determined only by fuel concentration gradient. In this Chapter, I confirm whether the multi-slot burner can also demonstrate the same tendencies shown in the previous studies or not.

The lift-off height and flame curvature is investigated with various sound pressures in Chapter 5. PIV measurement is conducted to confirm the burning velocity change.

In Chapter 6, the shape of the mixing layer is modeled and the fuel concentration with a potential to change in the lift-off height of the triple flame is calculated by established model. Numerical simulation is performed simultaneously and the validity of the model is investigated.

Chapter 7 concludes the present study.

2. Experimental setup and procedures

It has been clarified that the flame speed of the triple flame has strong correlation with the curvature of the leading edge of the premixed flame front, which has correlation with fuel concentration gradient in the front of the premixed flame front. To investigate the influence of acoustic oscillation on the mixing layer, a multi-slot burner is employed in order to form two-dimensional flames in a mixing layer with a laminar flow and no shear condition. The experimental apparatus consists of a multi-slot burner, a resonance tube, sound systems and fuel supply systems. The detail of the experimental setup is explained below.

2.1. Experimental setup

2.1.1. Multi-slot burner

A multi-slot burner, referred to in Hirota's work [39], is shown in Fig. 2-1-2. It consists of a diffusion chamber, a convergent nozzle, a settling chamber and a test section. Its interior is separated into four sections by splitter plates. Splitter plates are grooved into the wall and its junctions are filled by caulking agent to prevent gases from leaking into other sections. The splitter plates have sandwich construction which consists of three plates. The center plate's thickness is 0.1 mm in order to prevent the thickness of the mixing layer and the flow velocity from variation due to vortex. The outer two plates whose thickness is 0.4 mm in order to improve the stiffness sandwich the center plate. Each outer plates ends at 10 mm upstream of the center plate edge in order to expose the edge. The difference in level at the corner, which is made by the center and the outer plates, is infilled by resin and smoothen to make the smooth surface. Each sections of the central two has 8 fuel and air intake ports respectively at the bottom of the diffusion section, and fuel/air mixture is supplied to the one section and air is supplied to the other section in order to make concentration gradient. Steel balls whose sizes are 5/32 inches and quantity is 2.4×10^4 are put into the diffusion section to promote the mixing well. Nozzle section has a convergent nozzle. A honeycomb ceramics (NGK INSULATORS, Ltd., HONEYCERAM 2.5/900HEX), whose wall thickness is 0.064 mm and cell pitch is 0.91 mm, is inserted into the end of the settling section in order to straighten the flow and make flow distribution uniform. This also contributes to prevent flashback. Each side of the settling section has co-flow nozzles. These nozzles eject nitrogen to prevent the main flow, where flame is formed, from vortex generation in shear layer. The co-flow section also has steel balls whose sizes are 1.5 mm and quantity is 5.2×10^4 in order to equalize the distribution of the flow speed. Quarts windows are set in front and back side of the test section. East and west side of the test section is open so that the sound can propagate through the test section. The multi-slot burner is installed in a resonance tube in order to place the flame at the position corresponds with the velocity anti-node, as shown in the Fig. 2-1-3.

2.1.2. Sound and sound measurement systems

To oscillate the flow, a monotone sine wave signal of frequency f is generated by function generator. The formed sine wave is amplified into required amplitude by the power amplifier (BEHRINGER, EP 2000) and resonated in a resonance tube. The resonance tube which is made of stainless steel is shown in Fig. 2-1-3. Its length is 400 mm; the inner diameter is ϕ261 mm; and the thickness is 3 mm. There are two opposed openings whose width are 100 mm at the wall of the tube. The burner is inserted through one opening and burned gas is exhausted from the other opening.

The flame can be observed through this opening section. Two loud speakers (Peavey, 1008-8 HE BWX) are aligned face to face at the both end of the resonance tube. A pressure gauge port is placed at the tube end. A gauge pressure sensor (KELLER corporation, PR-10) is employed to measure the sound pressure. Sound pressure is converted into electric signal by signal converter (KELLER corporation, ET-95KS).

2.1.3. Gas supply system

Fuel, air and nitrogen are brought through the gas supply system which is shown in Fig. 2-1-4. To make the premixed gas of fuel and air, mass flow controllers (HORIBA, Ltd., model SEC-N100 series) are employed. Mass flow controllers contributes easy control of equivalence ratio and flow rate simultaneously. Air flow rate and nitrogen flow rate are controlled by area flow meters with precision needle valve (KOJIMA INSTRUMENTS Inc., model RK1200 series). Fuel can be switched by three-way valve. The mixture and air are supplied to the multi-slot burner through hoses. To supply gases to the multi-port of the burner, the hose is branched off into 1-2-4-8 layout. The length of each branched off hoses are the same to make pressure drop identical for each hose and to supply gases evenly.

2.1.4. Schlieren optics

In order to visualize the mixing layer, Z-type schlieren configuration which is shown in Fig. 2-1-5 is employed. A xenon lamp (Hamamatsu Photonics K. K., L2423) is employed for light source. The light is focused by collimating lens. The focused light is collimated by the concave mirror. The collimated light passes through the test section and the light is re-focused by the other concave mirror. Focal length of the concave mirror is 1,507 mm and 1,510 mm. The partially shaded light by knife edge is re-collimated by the collimating lens and enters the high-speed camera (nac

Image Technology, Inc., HX-5).

2.1.5. PIV configuration

Burning velocity of the flame is measured by Particle Image Velocimetry(PIV). PIV arrangement is shown in Fig. 2-1-6. The stainless wall is mounted on the opposite side of the loud speaker. The acrylic window which is mounted in the wall makes a laser sheet (λ = 532 nm) possible to reach the test section. The laser sheet is generated by LD excitation YVO_4 laser (KATOKOKEN Co., Ltd., G200). TiO_2 whose diameter is 20 $\sim$ 30 μm is employed for a tracer. Hydrophobizing agents whose average diameter is 4 μm are mixed with TiO_2 particles. Raw images are taken by the high speed camera (nac Image Technology, Inc., HX-5).

2.2. Procedure

First, nitrogen whose flow rate is controlled by area flow meters is supplied to the co-flow nozzle. Fuel/air mixture and air are supplied to the mixture and air port respectively. After ejection of the mixture and air, a mixing layer is formed between mixture and air. Flame is formed in the mixing layer at room temperature and atmospheric pressure. After stabilization of the flame, the standing acoustic field is generated. Speakers are driven with monotone sine wave in the opposite phase of around 0.5 kHz to resonate in a half wave length. Since the resonance frequency shifts due to the change in sound speed which depends on the gas temperature during combustion, frequency is readjusted to keep the resonance. The amplitude of the medium is controlled by the power amplifier's gain. Direct photos of the flame are acquired by a digital still camera (Nikon corporation, D7000). Mixing layer is observed by schlieren technique. The sound pressure is measured at the pressure anti-node. The peak sound pressure P_{max} is read by the oscilloscope and RMS value of the sound pressure P_S is calculated by following relation,

$$P_S = \frac{P_{max}}{\sqrt{2}} \tag{2.2.1}$$

2.3. Experimental conditions and their accuracies

2.3.1. Experimental conditions

Experimental conditions are shown in Table 2-1-1. Methane and propane are the employed fuel. Their purities are greater than 99.9 % of methane and 99.5 % of propane. Their one-dimensional adiabatic laminar flame speeds are close with each other. If the laminar flame speed is high, the high flow velocity is needed to keep the higher lift-off height so that the lift-off height change can be valified in the wider range of the lift-off hight. It yeilds the high Reynolds number condition. Their flame speeds are low compared with other hydro carbon fuels and hydrogen, which contributes for varification with laminar condition. On the other hand, their diffusivities are different. Because of these characteristics, the diffusion effect can be investigated at the same lift-off height with laminar flow condition. The mean flow velocities of methane and propane are set to 1.0 m/s and 1.3 m/s respectively so that the change in the lift-off height can be investigated in a broad height range of the test section without blow-off. Calculated Reynolds number is shown in table 2-1-2. Equivalence ratio ϕ of methane/air mixture is calculated assuming that air is composed of 21 % oxygen and 79 % nitrogen.

2.3.2. Distribution of local flow speeds and turbulence intensity

Distribution of local flow speeds and turbulent intensities are measured by a hot-wire anemometer (KANOMAX Japan, Inc., CTA:Model1010, Linearizer:Model1013). An I type probe (KANOMAX Japan, Inc., 0251R-T5) is employed. The probe is mounted along streamwise. The element of a hot wire is set parallel to the splitter plate. The output voltage depending on the flow speed is calibrated by probe calibrator (KANOMAX Japan, Inc., Model1065). Measured flow speeds and intensities with various height are shown in Fig. 2-3-1 through 2-3-5, where x denotes the transverse axis of the flow. The data of the local flow speeds are averaged over 2.4 sec. It is found that the wider potential core exists below the height of approximately y = 100 mm. The turbulence intensities of the main flow are below 2 $\%$ below the height of y = 75 mm. The distribution of the flow speed at the nozzle center along the streamwise axis is shown in Fig. 2-3-6. As seen, the flow speed in the vicinity of flame forming position is uniform along both streamwise and transverse direction. Thus, the concentration gradient is the only variable in the experimental system.

2.4. Definition and evaluation method

2.4.1. Fuel concentration gradient

Fuel concentration gradient is defined as follow,

$$\nabla Y_F = \left| \frac{Y_u - Y_l}{x_u - x_l} \right| \tag{2.4.1}$$

where Y_u and Y_l stand for the fuel mass fraction of the upper and lower flammability limit respectively. These values calculated from the mole fraction of the other work

[73] are shown in table 2-1-3. The location of upper and lower flammability limits are expressed by x_u and x_l respectively.

2.4.2. Measurement method of flame curvature and lift-off height

Direct photos of flame are taken by the digital still camera at exposure time of 1/30 s, aperture value of 6.3 and ISO sensitivity of 800. Approximately 16 acoustic cycle averaged image of the flame is obtained exposure in the case of 0.5 kHz. The spatial resolution is 0.023 mm/pix. Acquired images are converted into binary images by image processing. The coordinates of the flame leading edge which are defined by the threshold of the luminosity are obtained by binary images. The obtained coordinates are approximated by quadratic function using least-square method with determination coefficient of 0.99 or greater. The parabolic flame path approximation have been conducted by other workers [47]. The flame curvature, that is the curvature of the quadratic curve's vertex, can be expressed as follow formula,

$$1/R_f = 2a \tag{2.4.2}$$

where R_f is the curvature radius of the flame's leading edge, a is the coefficient of the acquired quadratic function's second-order term. The lift-off height h [mm] is defined as the y coordinate of the quadratic curve's vertex.

2.4.3. PIV analysis method and definition of the burning velocity

The particle images with various sound pressure is acquired by the high speed camera at frame rate of 5,000 fps, exposure time of 199.3 μs and aperture value of 2.8. The spatial resolution of each images is 0.067 mm/pix. The PIV processing algorithm is Fluere [74] developed by the group of Delft University, which is based on the

Scarano and Riethmuller's work [75]. Multi-pass processing of 4 steps is employed. Multi-pass processing uses the large interrogation window first and changes to the smaller window size to remove the error vector with high spatial resolution. The first interrogation window size is 64×64 pixels with 50 % overlap and the final is 32×32 with 87.5 % overlap. Figure 2-4-1 shows a raw image and flow speed distribution in the vicinity of the leading edge of triple flame. Burning velocity is defined as the minimum velocity along streamwise velocity thorough a leading edge of visible flame surface [36]. In the case of with sound, the location of the leading edge moves with fluid motion. The burning velocity is defined as the following procedure. First, the y coordinate, where streamwise velocity is minimized, is found along streamwise axis with various x coordinates. The velocity at the minimum y coordinate, i. e. the most upstream coordinate, is defined as the burning velocity. I also confirmed that the y coordinate is the unique coordinate where the streamwise velocity is minimum in the analyzed areas of 100 images along both the streamwise and the transverse directions as shown in the Fig. 2-4-1. Acquired burning velocities are averaged over 1,024 images which include approximate 100 acoustic cycles.

3. Numerical simulations

To conduct detail analysis, I conduct numerical simulations of two method about the mixing layer's development. One is to solve the pressure fluctuation and the convection of the flow as experimental condition (Case1). The mixing layer's development including the influence of the vortex in the mixing layer induced by convection or pressure can be investigated by this calculation condition. The computational domain should be large since its size is governed by the acoustic wave length. Therefore, computational cost is expensive. The other is to give the initial boundary shape between mixture and air (Case 2). In this case, the flow is not apply as boundary condition. In the case 1, the boundary should be sinusoidally-deformed by the normal sine-wave fluid oscillation streamwise. Therefore, the initial boundary between mixture and air is given by sine function. This sinusiodally-deformed initial boundary is set as the initial condition in the case 2. In this calculation, the influences of the vortex can not simulated. The computational domain can be small. This contributes the calculation with fine grid to accurately resolve the thin mixing layer.

3.1. Diffusion in standing acoustic fields (Case 1)

The computational domain and the boundary condition are shown in Fig. 3-1-1. The grid sizes in the vicinity of the mixing layer are 0.4 mm × 0.2 mm in order to resolve the thin layer. The number of the nodes is 3.0×10^5. The calculation code is FLUENT 14.5 (ANSYS, Inc.). SIMPLE scheme [76] which is one of the pressure based decoupled algorithm is employed for coupling of velocity and pressure with unsteady calculation. The spatial discretization scheme is second-order upwind for pressure and third-order MUSCL [77] for others. First order implicit method is employed for time integration. The species and the heat transport are solved by molecular kinetic theory. Lennerd-Jones potential parameters shown in table 2-1-8 are taken from other work [78]. Four velocity inlets whose size is 10 mm in each are set at the center bottom boundary of the computational domain. As with the case of experiment, mixture and air enter the computational domain from the central two inlets and nitrogen enters from the outer two inlets. The standing acoustic fields are generated by moving the east and the west moving wall in the same phase. Time step is 2.3×10^{-5} s. Initial conditions are shown in table 2-1-4.

3.2. Diffusion of the meandered mixing layer (Case 2)

I conducted the numerical calculation of diffusion of the meandering mixing layer by setting the meandering boundary in the calculation domain in advance. The boundary shape is formed by lateral fluid oscillation. In this calculation, the initial boundary shape which is made by streamwise convection and lateral fluid oscillation is set up. Since the meandering mixing layer can be simulated without oscillation, the pressure effect, e. g. baroclinic torque, and influences of the vortex do not work. The calculation load is quite low. The computational domain and the boundary conditions are shown in Fig. 3-1-2. All surrounding boundaries are pressure outlet. The domain size is 20 mm × 5.2 mm. The meandered boundary's shape is set as sine function and it's wave length λ is given by the follow formula,

$$\lambda = \frac{U_u}{f} \tag{3.2.1}$$

The grid size is 0.01 mm square. The number of the nodes is 1.1×10^6. Time step is 1.0×10^{-5} s. Second order implicit is employed for time integration. Other conditions are based on the numerical simulation of case 1. Initial conditions are shown in table 2-1-5.

3.3. Conservation equation

Mass conservation:

$$\frac{\partial \rho}{\partial t} + \nabla \cdot (\rho \overrightarrow{v}) = 0 \tag{3.3.1}$$

Momentum conservation:

$$\frac{\partial \rho \overrightarrow{v}}{\partial t} + \nabla \cdot (\rho \overrightarrow{v}\,\overrightarrow{v}) = -\nabla p + \nabla \cdot (\tau_{ij}) + \rho \overrightarrow{g} \tag{3.3.2}$$

where $\overrightarrow{g}$=(0, -9.81) [m/s^2] (Case 1), $\overrightarrow{g}$=(0, 0) (Case 2).

Species conservation:

$$\frac{\partial \rho Y_i}{\partial t} + \nabla \cdot (\rho \overrightarrow{v} Y_i) = -\nabla \cdot \overrightarrow{J}_i \tag{3.3.3}$$

Energy conservation:

$$\frac{\partial \rho E}{\partial t} + \nabla \cdot (\overrightarrow{v}(\rho E + p)) = \nabla \cdot (\lambda_m \nabla T - \sum_i h_i \overrightarrow{J}_i) \tag{3.3.4}$$

3.4. Properties

3.4.1. Thermodynamic properties

Heat capacity (Pure):

$$c_{p,i}/R = a_1 + a_2 T + a_3 T^2 + a_4 T^3 + a_5 T^4 \tag{3.4.1}$$

(a_1 to a_5, see table 2-1-6)

Heat capacity (Mixture):

$$c_p = \sum_i Y_i c_{p,i} \tag{3.4.2}$$

3.4.2. Transport properties

Viscosity of pure gas i (Chapman and Enskog [79]):

$$\eta_i = 2.67 \times 10^{-6} \frac{\sqrt{M_i T}}{\sigma^2 \Omega_\eta} \tag{3.4.3}$$

(M_i, see table 2-1-7. σ, see table 2-1-8.)

$$\begin{aligned}\Omega_\eta = [1.16145(T^*)^{-0.14874}] + 0.52487[\exp(-0.7732\,T^*)] \\ +2.16178[\exp(-2.43787\,T^*)]\end{aligned} \tag{3.4.4}$$

$$\text{where} \quad T^* = \frac{kT}{\epsilon} \tag{3.4.5}$$

(ϵ/k, see table 2-1-8.)

Viscosity of mixture gas (Wilke):

$$\eta_m = \sum_{i=1}^{n} \frac{X_i \eta_i}{\sum\limits_{j=1}^{n} X_j \phi_{ij}} \tag{3.4.6}$$

$$\phi_{ij} = \frac{[1 + (\eta_i/\eta_j)^{1/2}(M_j/M_i)^{1/4}]^2}{[8(1 + M_i/M_j)]^{1/2}} \tag{3.4.7}$$

$$\phi_{ji} = \frac{\eta_j M_i}{\eta_i M_j} \phi_{ij} \tag{3.4.8}$$

Heat conductivity of pure gas (Eucken):

$$\lambda_i = \frac{15}{4} \frac{R}{M_i} \eta_i \left(\frac{4}{15} \frac{c_p M_i}{R} + \frac{1}{3} \right) \tag{3.4.9}$$

Heat conductivity of mixture gas (Wassiljewa):

$$\lambda_m = \sum_{i=1}^{n} \frac{X_i \lambda_i}{\sum\limits_{j=1}^{n} X_j \phi_{ij}} \tag{3.4.10}$$

Diffusion coefficient for binary gas systems (binary diffusivity) at low pressures (Chapman and Enskog [79]):

$$D_{ij} = 0.00188 \frac{\left[T^3 \left(\frac{1}{M_i} + \frac{1}{M_j}\right)\right]^{1/2}}{P \sigma_{ij}^2 \Omega_D} \tag{3.4.11}$$

$$\epsilon_{ij} = (\epsilon_i \epsilon_j)^{1/2} \tag{3.4.12}$$

$$\sigma_{ij} = \frac{\sigma_i + \sigma_j}{2} \tag{3.4.13}$$

$$\begin{aligned} \Omega_D = \frac{1.06036}{T_D^{*0.1561}} + \frac{0.19300}{\exp(0.47635\, T_D^*)} + \frac{1.03587}{\exp(1.52996\, T_D^*)} \\ + \frac{1.76474}{\exp(3.89411\, T_D^*)} \end{aligned} \tag{3.4.14}$$

$$\text{where} \quad T_D^* = \frac{kT}{\epsilon_{ij}} \tag{3.4.15}$$

4. Lift-off height and flame curvature without sound

As mentioned in section 2.3.2, the distribution of the streamwise flow velocity in the test section is uniform. Therefore, fuel concentration gradient is the only control factor in this experiment. If the fuel concentration gradient changes, the flame curvature changes and burning velocity also changes. Since the flow velocities are same at any height, the flame should stabilize at the lift-off height where the fuel concentration gradients are the same. To confirm this characteristics, the lift-off height and flame curvature without sound are investigated.

4.1. Relationship between equivalence ratio and lift-off height

Figure 4-1-1 and 4-1-2 show the direct photos of the methane and the propane triple flame without sound respectively. The bottom end of the photos correspond with the nozzle exit plane. All photos are trimmed in the size of 80 mm × 20 mm and center of the photo corresponds with the position of the center splitter plate which divides fuel/air mixture from air. The flame speed at the leading edge of the triple flame is the fastest since the leading edge is located at the most upstream location. Since the flame speed decreases with distance from the leading edge along the premixed flame surface, both fuel rich and lean premixed flame wing bend to the downstream. The diffusion flame is formed from the leading edge by reaction of excess fuel and oxidizer which cannot be consumed in the premixed flame. Figure 4-1-3 and 4-1-4 show the measured lift-off height and flame curvature as function of ϕ. Both in the case of methane and propane, it was found that the lift-off height increases with increase in the equivalence ratio whereas no significant change was found in the flame curvature.

4.2. Discussion

The solution of one-dimensional diffusion equation is expressed by using error function as

$$Y_F(x,t) = \frac{Y_{F,0}}{2}\left[1 + \mathrm{erf}\left(\frac{x}{\sqrt{4D_{ij}t}}\right)\right] \tag{4.2.1}$$

where $Y_F(x,t)$ denotes fuel mass fraction at elapsed time t from the initiation of diffusion at site x. $Y_{F,0}$ is the fuel mass fraction of the mixture. D_{ij} is the binary diffusivity calculated by Eq.(3.4.11). The binary diffusivity of the fuel and nitrogen which is the major gas in this system is employed for calculation. Because of no sound and no reduction of streamwise flow velocity, flow proceeds to y in time t. Therefore, t can be expressed as

$$t = \frac{y}{U_u} \tag{4.2.2}$$

Thus, Eq. (4.2.2) can be rewritten with following formula.

$$Y_F(x,y) = \frac{Y_{F,0}}{2}\left[1 + \mathrm{erf}\left(\frac{x}{\sqrt{4D_{ij}(y/U_u)}}\right)\right] \tag{4.2.3}$$

The calculated distributions of fuel concentration gradient and experimental results of the lift-off height are shown in Fig. 4-2-1 and 4-2-2. The lines are the calculated fuel concentration gradients using Eq. (2.4.1) with various equivalence ratios and the plots are the experimental results of the lift-off height. The experimental results are ploted on the calcurated lines of the fuel concentration gradient, so that the equivalence ratios of the experimental results correspond with that of for the calculation of the lines. Since the diffusion flux is proportional to the fuel concentration gradient, fuel diffuses rapidly after immediate ejection of gases. As increase in the height, the fuel concentration gradient approaches asymptotically to zero. In the case of the methane, the fuel concentration gradients at the lift-off heights are the same regardless of the heights and these values are approximately 0.04 mm^{-1}. Similar results were found in the case of propane and these values are approximately 0.06 mm^{-1}. Since the local flow velocities of the cold flow along streamwise are constant, the burning velocity of the triple flame should be constant regardless of the lift-off heights. The burning velocity of the triple flame is determined by the flame curvature, which is determined by fuel concentration gradient [39]. Since the equivalence ratio at the leading edge of the triple flame is constant of approximately stoichiometric [37], the flame curvature should be constant as long as the burning velocity is constant. Therefore, no significant change of the flame curvature and fuel concentration gradients at the various lift-off heights means that the lift-off height of the triple flame determined by the only fuel concentration gradient in the case of this experimental setup. That is to say, the fuel concentration gradient becomes steeper with increase in the equivalence ratio and flame moves to the downstream from the original lift-off height. The flame is re-stabilized at another lift-off height where the fuel concentration gradient is equal to the original one.

5. Lift-off height and flame curvature with sound

I confirmed that the lift-off height of the triple flame is determined only by the fuel concentration gradient in § 4. In this section, I investigate the lift-off height and flame curvature with various sound pressures. It is thought that the burning velocity does not change as long as the lift-off height decreased to the height where the fuel concentration gradient is equal to that without sound. PIV is conducted to confirm the burning velocity change.

5.1. Relationship between sound pressures and lift-off height

Direct photos of the triple flame with various sound pressures are shown in Fig. 5-1-1 to 5-1-8. In the case of both methane and propane, the lift-off height decreased with increase in the sound pressure with equivalence ratio range of 2.8 to 3.4. Measured lift-off heights and flame curvatures are shown in Fig. 5-1-9 to 5-1-16. In the case of both methane and propane, the lift-off height decreased with increase in the sound pressure. As increase in the sound pressure, the lift-off height approaches asymptotically to the constant lift-off height. The flame curvature tend to change only slightly with the increase in the sound pressure. The slope of the lift-off height locus with respect to sound pressure is gradual in the range of P_S=0 to approximate 0.04 kPa. The slope of the lift-off height becomes gradually steeper with increase in sound pressure after $P_S \approx$ 0.04 kPa. It becomes gradual again in the higher sound pressure region.

5.2. Burning velocity of the triple flame with sound

The raw images of PIV are shown in Fig. 5-2-1. The bottom of each image is the nozzle exit location. The tracer particles in the flame radiate the strong light due to increase in the temperature. The location of the visible flame surface moves to upstream with increase in the sound pressure similar to the experiment of §5-1. Burning velocity of the triple flame with various sound pressures is shown in Fig. 5-2-2. The location where the burning velocity is taken is shown in the figure with second axis. As shown in the figure, the minimum velocity location without sound apploximately agree with the lift-off height without sound which is shown in §5-1. It is found that the burning velocity does not show significant change with sound and are approximately 0.6 m/s. The measured burning velocity is higher than one-demensional adiabatic laminar burning velocity which is 46.3 cm/s of propane [81]. This tendency is reported in previous works [39, 82].

5.3. Discussion

As mentioned in §4, the lift-off height is determined by the fuel concentration gradient of the leading edge of the triple flame. At this time, it is found that the lift-off height is lower with lower fuel concentration gradient. Considering above, I discuss the mechanism of lift-off height reduction in acoustic field.

The schematic of the relation between mixing layer and lift-off height is shown in Fig. 5-3-1. Δx and h denotes the original width of mixing layer and lift-off height without sound. If the width of the mixing layer becomes $\Delta x'$, the flame curvature decreases due to increase in the width and flame speed changes. On the other hand, the unburned gas velocity ahead of the leading edge does not change. Therefore, the flame moves to the lift-off height h' where the flame speed corresponds with the unburned gas velocity.

If the lift-off height is determined only by fuel concentration gradient just as in the no sound experiment, the flame curvature should not change if the burning velocity does not change. As shown in Fig. 5-1-9 to 5-1-16, slight change in the flame curvature is found, however, the remarkable correlation with the sound pressure was not found and there are some dispersion of this level in the measurement of the flame curvature without sound. As shown in Fig. 5-2-2, the burning velocity does not show the significant change. Therefore, the lift-off height of the triple flame changes by change in the fuel concentration gradient by sound.

6. Model of fuel concentration gradient with sound

The detail analysis of the mixing layer in acoustic fields by schlieren images and numerical simulations are conducted to clarify the mechanism of the lift-off height reduction, which is observed in §5. It was confirmed that the lift-off height is determined only by fuel concentration gradient in this experimental environment in §4. To clarify the lift-off height reduction mechanism, The model which can describe the shape of the mixing layer was established with simple numerical expression under acoustical oscillations. The fuel concentration gradient of the modeled mixing layer was calculated. By observation of the shape of the actual mixing layer by schlieren technique, the modeled mixing layer is compared with the experimental observed mixing layer. To compare the calculated fuel concentration gradients of the modeled mixing layer with the numerical simulated results, I investigate the validity of the model. Finally, The dominant parameter of the shape and fuel concentration gradient are established. The model assumes that no vortex is generated. Therefore, the vorticity is calculated by numerical simulation of case 1.

6.1. Experimental observation of the mixing layer using schlieren technique

Mixing layer in acoustic fields was observed by schlieren technique in order to establish the mixing layer's shape and obtain the fuel concentration gradient.
Schlieren images of the mixing layer without sound are shown in Fig. 6-1-1. The left image is methane and the right is propane. View sizes of each images are 60 mm × 40 mm. The lateral size of the image corresponds with the nozzle width. Equivalence

ratio is 3.0 for each fuel. The center shadow corresponds with the mixing layer. The mixing layers are straight without sound. The width of the mixing layer increases with distance from the nozzle exit. The mixing layers with sound are shown in Fig. 6-1-2 and 6-1-3. The mixing layer was meandered by transverse fluid motion. The valleys of each meandered mixing layer become cusp. In the case of methane, the downstream shadow becomes faint. In the case of propane, the dark hue does not show the significant change, whereas the dark region broaden out due to meandering.

6.2. Diffusion and Brownian motion

Diffusion occurs as a result of Brownian motion which is stated by Einstein [83]. It is well known that diffusion coefficient is expressed as follow formula,

$$D \approx \frac{\langle x^2(t) \rangle}{2t} \tag{6.2.1}$$

where $\langle x^2(t) \rangle$is the second moment of the Gaussian distribution which means the probability of being at site x and time t [84]. The speed of the diffusion denotes the alteration of x from moment to moment. Therefore, the diffusion speed v_D is given as

$$v_D \propto \sqrt{\frac{D_{ij}}{t}} \tag{6.2.2}$$

or

$$v_D = \sqrt{\frac{a_D D_{ij}}{t}} \tag{6.2.3}$$

where a_D is a constant of proportion. The isoline of mass fraction is given as

$$Y_F(t) = \sqrt{a_D D_{ij} t} \tag{6.2.4}$$

or

$$Y_F(y) = \sqrt{\frac{a_D D_{ij} y}{U_u}} \tag{6.2.5}$$

6.3. Modeling of the meandering mixing layer's shape and fuel concentration gradient

6.3.1. Calculated shape of the mixing layer

I established the model of the mixing layer. When the fuel concentration gradient is calculated, the width of the mixing layer is needed. However, as we show in the § 4, the diffusion is described by error function of the particular solution of the diffusion equation. Consequently, the width of the mixing layer cannot be calculated algebraically, which is inconvenient for modeling. Therefore, The distribution of the mixing layer is calculated using Eq. (4.2.1) and the width of the mixing layer is obtained numerically in advance. The calculated distributions of the mixing layer's width by error function and their fitting curves are shown in Fig. 6-3-1 and 6-3-2. The function of the fitting curves are the following formula,

$$\Delta x_{l,t} = \sqrt{a_l D_{ij} t} \tag{6.3.1}$$

$$\Delta x_{u,t} = \sqrt{a_u D_{ij} t} \tag{6.3.2}$$

where $\Delta x_{l,t}$ and $\Delta x_{u,t}$ are the distance of the upper and lower flammability limits from the initial boundary. The location of the initial boundary corresponds with the location of the initial contact plane between the mixture and air. In other words, the location corresponds with the location of the center splitter plate in this experiment. Moreover, the fuel mass fraction along this boundary is $Y_{F,0}/2$ as Eq. 4.2.1 have shown. a_l and a_u are the proportional constants of the boundary's development toward to the lower and the upper flammability limit boundary respectively. As a result, $a_l D_{ij}$ is 44.07 and $a_u D_{ij}$ is 3.67 in the case of methane, and $a_l D_{ij}$ is 16.47 and $a_u D_{ij}$ is 25.72 in the case of propane with equivalence ratio of 3.0 and determination coefficient of 1.00. In this study, the mixing layer is defined as the width between upper and lower flammability limit. Difference in these constants are larger with greater difference of Y_u, Y_l and $Y_{F,0}/2$. Since the flammability limit of methane is narrower, the difference in the width of the mixing layer of methane and propane is not significant, although the diffusion coefficient of methane is approximately twice as much as that of propane.

The schematic of the meandered mixing layer with no advection is shown in Fig. 6-3-3. The chain line shows the meandered initial boundary. The geometry of the mixing layer at time $t + \Delta t$ which is shown in the figure by dashed line is expressed as follow formulas neglecting the advection term,

$$\mathbf{F}_{l,t+\Delta t} = \mathbf{F}_{l,t} + \left[\sqrt{a_l D_{ij}(t + \Delta t)} - \sqrt{a_l D_{ij} t}\right] \hat{\mathbf{n}}_{l,y} \tag{6.3.3}$$

and

$$\mathbf{F}_{u,t+\Delta t} = \mathbf{F}_{u,t} + \left[\sqrt{a_u D_{ij}(t + \Delta t)} - \sqrt{a_u D_{ij} t}\right] \hat{\mathbf{n}}_{u,y} \tag{6.3.4}$$

where $\hat{\mathbf{n}}_{l,t}$ and $\hat{\mathbf{n}}_{u,t}$ denote the unit normal vector of the boundary surface toward the fuel lean boundary and the fuel rich boundary respectively. Equation (6.3.3) and (6.3.4) can be written as

$$\frac{\mathbf{F}_{l,t+\Delta t} - \mathbf{F}_{l,t}}{\Delta t} = \frac{\left[\sqrt{a_l D_{ij}(t+\Delta t)} - \sqrt{a_l D_{ij} t}\right]}{\Delta t}\hat{\mathbf{n}}_{l,y} \tag{6.3.5}$$

and

$$\frac{\mathbf{F}_{u,t+\Delta t} - \mathbf{F}_{u,t}}{\Delta t} = \frac{\left[\sqrt{a_u D_{ij}(t+\Delta t)} - \sqrt{a_u D_{ij} t}\right]}{\Delta t}\hat{\mathbf{n}}_{u,y} \tag{6.3.6}$$

Taking the limit of both sides of each Eq. (6.3.5) and (6.3.6), these are written as

$$\lim_{\Delta t \to 0} \frac{\mathbf{F}_{l,t+\Delta t} - \mathbf{F}_{l,t}}{\Delta t} = \lim_{\Delta t \to 0} \frac{\left[\sqrt{a_l D_{ij}(t+\Delta t)} - \sqrt{a_l D_{ij} t}\right]}{\Delta t}\hat{\mathbf{n}}_{l,y} \tag{6.3.7}$$

and

$$\lim_{\Delta t \to 0} \frac{\mathbf{F}_{u,t+\Delta t} - \mathbf{F}_{u,t}}{\Delta t} = \lim_{\Delta t \to 0} \frac{\left[\sqrt{a_u D_{ij}(t+\Delta t)} - \sqrt{a_u D_{ij} t}\right]}{\Delta t}\hat{\mathbf{n}}_{u,y} \tag{6.3.8}$$

From the definition of the defferential, Eq. (6.3.7) and (6.3.8) are expressed as

$$\frac{\partial \mathbf{F}_{l,t}}{\partial t} = \frac{1}{2}\sqrt{\frac{a_l D_{ij}}{t}}\hat{\mathbf{n}}_{l,y} \tag{6.3.9}$$

and

$$\frac{\partial \mathbf{F}_{u,t}}{\partial t} = \frac{1}{2}\sqrt{\frac{a_u D_{ij}}{t}}\hat{\mathbf{n}}_{u,y} \tag{6.3.10}$$

In particular, we assume that the initial boundary of the lower flammability limit corresponds with that of the upper flammability limit at $t = 0$ and follow relation is given.

$$\mathbf{F}_{l,0} = \mathbf{F}_{u,0} \tag{6.3.11}$$

In the case of with sound, the boundary moves perpendicular to the streamwise. Since the sound is generated as the sine wave function, the initial shape of the boundary can be expressed as

$$\mathbf{F}_{l,0} = \mathbf{F}_{u,0} = \left(A\mathrm{sin}\frac{2\pi f y}{U_u}, y \right) \tag{6.3.12}$$

By using Eq. (6.3.12), the unit normal vectors can be expressed as followings,

$$\hat{\mathbf{n}}_{u,y} = -\hat{\mathbf{n}}_{l,y} = \frac{1}{\sqrt{1 + \frac{4\pi^2 f^2 A^2}{U_u^2}\cos^2\frac{2\pi f y}{U_u}}} \left(-1, \frac{2\pi f A}{U_u}\cos\frac{2\pi f y}{U_u} \right) \tag{6.3.13}$$

Above model assumes that $\Delta x_{l,t}$ and $\Delta x_{u,t}$ are the function of only time with no advection because of simplification. Actually, $\Delta x_{l,t}$ and $\Delta x_{u,t}$ changes with height because of advection. Therefore, using the relation of Eq. (4.2.2) and the result conducted by Eq. (6.3.9) and (6.3.10), the shape of the mixing layer whose width changes in the height with convection is obtained. The calculated shapes of the mixing layer with various amplitudes are shown in Fig. 6-3-4 to 6-3-9. In the case of the amplitude of 0 mm, that is without sound, the mixing layer is straight. In the case of with sound, the mixing layer is meanders. The valley's shape becomes cusp progressively with distance from the nozzle exit, increase in the amplitude and advance of time from diffusion initiation.

6.3.2. Calculated fuel concentration gradient using the model of the mixing layer's shape

The fuel concentration gradient which is obtained numerically from the calculated shape using Eq. (6.3.9) and (6.3.10) is shown in Fig. 6-3-10. Figure 6-3-11 shows the taking position of the effective width of the mixing layer which is defined in the figure. The effective widths of the mixing layer are obtained at (a) to (d) shown in Fig. 6-3-11. The obtained effective widths are averaged over (a) through (d). The fuel concentration gradients are calculated by the averaged effective width. As shown in the graph, the fuel concentration gradient becomes gentle with increase in the amplitude of the initial boundary.

6.4. Numerical simulation of the meandered mixing layer

6.4.1. Growth of the mixing layer (Case 1)

The fuel concentration gradients with various sound pressures are calculated by numerical simulations. This calculation is conducted considering the flow in the oscillating field. The calculated fuel concentration gradients with various sound pressures are shown in Fig. 6-4-1 and 6-4-2. In the case of the methane, the sound is generated after 1.3 s from the ejection of the gas. The data are obtained after 1.6 s from sound generation. In the case of the propane, the sound is generated after 1.0 s from the ejection of the gas. The data are obtained after 1.3 s from sound generation. The data are averaged in a cycle, and averaged fuel concentration gradients are further averaged in 10 cycles. The calculated fuel concentration at the upstream mixing layer decreased with increase in the sound pressure. On the other hands, a little difference compared with the upstream mixing layer was found at the downstream mixing layer.

6.4.2. Growth of the mixing layer (Case 2)

Calculated fuel concentration gradients which are obtained by numerical calculation without convection are shown in Fig. 6-4-3 and Fig. 6-4-4. Figure 6-4-3 shows the result of λ=2.6 mm and Fig. 6-4-4 is that of λ=1.3 mm. The fuel concentration gradients are averaged like in the case of §6.3.2. To coincide with the topological position where the data are obtained in the §6.3.2., sample positions for average are y=3.9, 4.55, 5.2 and 5.85 mm in the case of λ=2.6 mm and y=2.275, 2.6, 2.925 and 3.25 mm in the case of λ=1.3 mm. Since the flow speed of experiment is 1.3 m/s in the propane case, λ=2.6 mm corresponds with the frequency of 0.5 kHz and λ=1.3 mm corresponds with the frequency of 1 kHz respectively. As shown in the figures, the fuel concentration gradients become gentle with increase in the amplitude of the initial boundary. The tendency corresponds with the result of model. The fuel concentration gradient of λ=1.3 mm is smaller than that of λ=2.6 mm compared with the same height and the same amplitude, which means that the higher frequency yields the smaller fuel concentration gradient.

6.5. Discussion

From the schlieren images, it is found that the mixing layer is meandered under acoustic oscillations. Meanwhile, it is also found that the shape of the valley of the meandered mixing layer progressively becomes cusp. The species diffuse to the direction of the concentration gradient according to Fick's law. The meandering of the mixing layer yields the streamwise component of the fuel concentration gradient. It is thought that the streamwise diffusion exceeds the lateral diffusion from the valley due to meandering and the cusp is formed. The visible shadow of the schlieren image does not correspond with the mixing layer since the shadow is visualized as the change in the luminosity which changes in proportion to the density gradient and the proportional constant is determined by the focal length of the concave mirror, the depth of the measurement field and so on. Since quantitative calibration is not be conducted in this experiment, the width of the visible shadow does not correspond with the calculated width of the mixing layer. However, the calculated shape corresponds with the shape observed by schlieren images qualitatively. Especially, we demonstrate the formation of cusp by our model. The cusp is formed as a result of earlier filling of the valley by streamwise diffusion than lateral diffusion. This means that the development speed of the mixing layer at the valley of the meandering layer is faster than that of straight layer without sound. This yields the wider mixing layer at position (b) and (d) shown in Fig. 6-3-11 with sound compared with the mixing layer without sound. In the case of the position (a) and (c) which are located in the middle between peak and peak, the effective width of the mixing layer which is defined as the width of x direction component also becomes wide since the boundary inclines to the y direction. The calculated fuel concentration gradients from the model are shown in Fig. 6-3-10. As shown in Fig. 6-3-10, the fuel concentration gradient decreases with increase in the amplitude. As a result of meandering, fuel concentration gradient becomes gentle due to forming the cusp and incline of the mixing layer. Similar result is obtained by numerical simulation. Although the fuel concentration gradient of numerical simulation gradually show a difference from that of model as time progresses, these results agree with each other.

I investigate the effect of the amplitude of the fluid motion. The boundary curve's shape can be described as the angle θ and amplitude A of the fluid motion. The slope of the tangent of the boundary can be described by the following formula which can be obtained by first order differential of Eq. (6.3.12).

$$\frac{\partial \mathbf{F}_0}{\partial y} = \left(\frac{2\pi f A}{U_u} \cos \frac{2\pi f y}{U_u}, 1 \right) \tag{6.5.1}$$

Acoustic Strouhal number St is defined as follow formula,

$$St = \frac{fA}{U_u} \tag{6.5.2}$$

then, the maximam angle between tangent and streamwise can expressed as

$$\theta_{max} = \tan^{-1} 2\pi St \tag{6.5.3}$$

Therefore, if the St is same, the boundary geometry becomes similar. St=0 donates the condition without sound.

Here, I will mention the time to form the cusp. Figure 6-5-1 shows the diffusion until cusp formation. Cusp starts when the diffusion from the inclined boundary advances to the curve radius R_c of vertex of sinusoidally-deformed boundary. The curve radius of the function $y = f(x)$ can be expressed as follow formula,

$$R_c = -\frac{\{1 + (dy/dx)^2\}^{\frac{3}{2}}}{d^2y/dx^2} \tag{6.5.4}$$

and if the right value is positive, the function is convex upward, if the right value is negative, the function is convex downward. Therefore, if the convex direction is not considered, the curve radius at the vertex of the boundary can be expressed as follow formula,

$$R_c = \frac{U_u^2}{4\pi^2 f^2 A} \tag{6.5.5}$$

Thus,the time to form the cusp t_c can be described as follow formula using Eq. (6.2.2) and (6.3.12),

$$t_c = \frac{U_u^4}{16\tilde{a}\pi^4 D_{ij} f^4 A^2} \tag{6.5.6}$$

which can also be expressed using St,

$$t_c = \frac{1}{16\tilde{a}\pi^4 D_{ij} St^2} \left(\frac{U_u}{f} \right)^2 \tag{6.5.7}$$

where $\tilde{a}$ is a_u or a_l whichever greater. Consequently, the cusp is not formed if $t < t_c$ is satisfied and following condition holds,

$$\sqrt{\tilde{a} D_{ij} t} \left(\frac{f}{U_u} \right) < \frac{1}{4\pi^2 St} \tag{6.5.8}$$

This equation can be expresses using Eq. (3.2.1),

$$\frac{\lambda}{\sqrt{\tilde{a} D_{ij} t}} > 4\pi^2 St \tag{6.5.9}$$

$\sqrt{\tilde{a} D_{ij} t}$ denotes the diffusion length in time t and St denotes the sharpness of the boundary's peak in a physical sense. Therefore, Eq. (6.5.9) means that the sharper the peak is, the shorter the time by forming of the cusp is. Figure 6-5-2 shows the boundary shape with low Strouhal number and thin mixing layer compared with the distance between peak and peak. Here, I define a new normalized parameter K which is defined as follow formula,

$$K = \frac{\lambda}{\sqrt{\tilde{a} D_{ij} t}} \tag{6.5.10}$$

Therefore, in the case of Fig. 6-5-2, $K > 4\pi^2 St$ is satisfied. As shown in the figure, the effective width of the mixing layer Δx_e at the middle between peak and peak at time t can be expressed as

$$\Delta x_e \approx \frac{\Delta x_{u,t} + \Delta x_{l,t}}{\cos\theta_{max}} \tag{6.5.11}$$

Therefore, the effective width at the middle between peak and peak broaden proportion to $1/\cos\theta_{max}$ because of meandering. Thus, the effective width is determined by St in the case of low St and thin mixing layer, which means that the $K > 4\pi^2 St$ is satisfied. In this condition, normalized fuel concentration gradient $\nabla Y_F / \nabla Y_F^0$ can be expressed as follow formula,

$$\frac{\nabla Y_F}{\nabla Y_F^0} \approx \cos(a\tan^{-1} 2\pi St) \tag{6.5.12}$$

where Y_F^0 is the fuel concentration gradient without sound. Since ∇Y_F is the averaged fuel concentration gradient at (a) to (d) in Fig. 6-3-11 whereas St represents the maximum angle θ_{max}, the proportional constant a is included for description of $\nabla Y_F / \nabla Y_F^0$ by St.

With increase in St and thickness of the mixing layer, the difference between the calculated $\nabla Y_F / \nabla Y_F^0$ by Eq. (6.5.12) and actual width occurs since the effective width is calculated including extra width due to the curve of the boundary as shown in Fig. 6-5-3.

In the case of $K \ll 4\pi^2 St$, $\nabla Y_F / \nabla Y_F^0$ can no longer be connected with St since the gap between peak and peak is filled by streamwise diffusion as shown in Fig. 6-5-4. It is thought that the effective width is subjected not to St but the amplitude of the fluid motion. This means that the normalized fuel concentration gradient can be expressed as follow in the case of $K \ll 4\pi^2 St$,

$$\frac{\nabla Y_F}{\nabla Y_F^0} \approx \frac{\Delta x_{u,t} + \Delta x_{l,t}}{2A + \Delta x_{u,t} + \Delta x_{l,t}} \tag{6.5.13}$$

The shapes can be summarized with St and K as shown in the Fig. 6-5-5. In other words, the shape of the mixing layer become similar with same St and K.

On the other hand, it is known that the pressure gradient and density change yields the vortex due to baroclinic torque in a binary-density field [85]. Since the sound yield the pressure gradient, the vortex is possible to induced with higher P_S condition in a binary-density field. The investigation of baroclinic torque caused by sound pressure on the flame wrinkling has been conducted [86], whereas the effect of the sound pressure on the small density change such like the mixing layer of this experiment is not sure. Since above estimation method can be applicable only in the condition of without vortex, I confirmed the vorticity magnitude.

Figure 6-5-6 and 6-5-7 show the one cycle averaged vorticity magnitude around the mixing layer of methane and propane respectively with P_S of 0.1 kPa. These data are obtained by numerical simulations with convection and its numerical conditions are same as that of §6.4.1. x =0.2 corresponds with the location of the splitter plate. In both cases, the significant vorticity is not found in the vicinity of the mixing layer compared with outer mixing layer with P_S = 0.1 kPa. Therefore, the estimation method as mentioned above is applicable in the experimental condition.

Figure 6-5-8 shows that the relation between normalized fuel concentration gradient $\nabla Y_F / \nabla Y_F^0$ and St in the case of low St condition. Both in the case of $t = 0.005$ s and $t = 0.04$ s, which correspond with K = 7.25 and K = 2.56 respectively, the normalize fuel concentration gradients are almost same. The solid line is the fitting function of $\cos(0.802 \tan^{-1} 2\pi St)$. The coefficient of 0.802 is determined by least square method. As shown in the graph, these results well correspond each other by set of appropriate coefficient of arctangent. It is thought that since the estimation formula of the width at the cusp is also included the St, the calculated $\nabla Y_F/\nabla Y_F^0$ also correspond with the function of $\cos(a\tan^{-1}2\pi St)$ approximately even if the cusp is formed. Therefore, the normalized fuel concentration gradient can be described by function of St for K slightly above $4\pi^2 St$ if appropriate constant is given.

As shown in the Fig. 6-5-8 to 6-5-11, $\nabla Y_F/\nabla Y_F^0$ is higher with lower K in the case of same St. The lower K compared with amplitude of the meandering, that is the thicker mixing layer, reduces the effect of meandering on the reduction of the fuel concentration gradient.

As increase in St and t, the boundary shape becomes as shown in Fig. 6-5-3. As shown in the figure, difference occurs between the effective width and $(\Delta x_{u,t} + \Delta x_{l,t})/\cos\theta_{max}$. On the other hands, the effective width at the valley of the meandered mixing layer broaden with larger θ_{max} due to formation of the cusp as shown in the figure.

The normalized fuel concentration gradient of higher St condition is shown in Fig. 6-5-9. The range of the figure covers the frequency up to 1 kHz and amplitude up to 1.0 mm. The normalized fuel concentration gradient of 0.04 s is slight difference from that of 0.005 s. In the case of high S_t, the normalize fuel concentration gradient after long elapsed time from diffusion initiation makes a difference from that after short elapsed time. Besides, in the case of the low St, since arctangent approaches to $\pi/2$ asymptotically, the fuel concentration gradient also approaches to 0 asymptotically from Eq. (6.5.12). In the case of high St, the asymptotic solution of the normalized fuel concentration gradient is 0 from Eq. (6.5.13). Therefore, both in the case of low and high St, the fuel concentration gradient approaches to 0 asymptotically in principle.

The relationships between St and $\nabla Y_F/\nabla Y_F^0$ arranging on K are shown in Fig. 6-5-12 to 6-5-19. Figure 6-5-12 to 6-5-15 are the results which are obtained by my model and Fig. 6-5-16 to 6-5-19 are the CFD results. In all cases, $\nabla Y_F/\nabla Y_F^0$ can be determined uniquely regardless of the wave length λ, that is frequency f by arranging on K. Therefore, $\nabla Y_F/\nabla Y_F^0$ can be estimated by St in the same K condition. Figure 6-5-20 shows the contour of the normalized fuel concentration gradient on the K-St plane. These data are employed from 6-5-12 to 6-5-15. The lacking data which are (K, St)=(1.81, 0.10) and (1.28, 0.10) are extrapolated for making the contour by linear function. Data other than the obtained data are interpolated by spline function. As shown in the contour, $\nabla Y_F/\nabla Y_F^0$ decreases with increase in St and K.

I will discuss the relation between $\nabla Y_F/\nabla Y_F^0$ and St extending to the prediction of the lift-off height. Equation 6.5.10 can be described using Eq. 4.2.2 as

$$K = \lambda\sqrt{\frac{U_u}{\tilde{a}D_{ij}y}} \tag{6.5.14}$$

From this equation, higher y yields lower K. Thus, if the amplitude and the frequency are constant, $\nabla Y_F/\nabla Y_F^0$ is lower with higher y. In other words, the effect of acoustic oscillation on making the fuel concentration gradient gentle of the mixing layer at high location is smaller than that of the mixing layer at low location. This tendency can be seen in Fig. 6-4-3, 6-3-10, 6-4-1 and 6-4-2.

Figure 6-5-21 shows the relation between St and the locus of the iso-fuel concentration gradient with various initial lift-off height. The iso-fuel concentration gradient is calculated by the model. As shown in the graph, the rates of iso-fuel concentration gradient change are small with increase in St in the small St region. They increase gradually in the higher St region. In the much higher St region, they decrease again. The behavior of the change in height, where the fuel concentration gradient is same, can be classified into three regions. This tendency corresponds with the change in the lift-off height of the flame with sound. Finally, the lift-off height approaches to zero with St in principle, which is shown in Eq. (6.5.12) and Eq. (6.5.13). The lift-off height change is explained by change in the fuel concentration gradient by acoustic oscillation from here onwards.

The locus of the iso-fuel concentration gradient with various initial lift-off height on the $K - St$ diagram is shown in Fig. 6-5-22. The height shown in Fig. 6-5-21 is converted into K using Eq. (6.5.14). As increase in St, the cusp is formed earlier with higher initail lift-off height.

7. Conclusion

I conducted the experimental observation and numerical modeling of the lift-off height and the shape of the upstream mixing layer in standing acoustic fields, and followings are concluded.

The lift-off height of the triple flame decreases with increase in the sound pressure. At this time, the flame curvature and the burning velocity of the flame are almost constant with change in the sound pressure. Therefore, the flame moves to the new height where the unburned gas velocity corresponds with the flame speed which is determined by flame curvature, i. e. fuel concentration gradient. The behavior of lift-off height change is classified into three region by the range of the sound pressure. In the low sound pressure region, the rate of change in the lift-off height with respect to sound pressure is small. In the middle sound pressure region, it becomes sudden. In the higher sound pressure region, it becomes small again.

From Schlieren image, it is found that the mixing layer meanders by the lateral fluid motion to streamwise in acoustic fields and cusp is formed. The shape of the mixing layer can be reproduced by the simple model which is created by the solution of one-dimensional diffusion which occurs from sinusoidally-deformed boundary. Since the boundary can be described by sine function, the geometric similarity can be described by acoustic Strouhal number St.

The effective width of the mixing layer broaden since the mixing layer makes an angle with the streamwise direction. Therefore, the broadening of the mixing layer can be described by S_t. At this time, there is restrictions for evaluations depending on the St and K, which is the ratio of the diffusion length $\sqrt{\tilde{a}D_{ij}t}$ and wave length of the boundary λ.

In the case of $K > 4\pi^2 St$, the cusp is not formed at the valley of the sinusoidally-deformed boundary. Besides, the normalized fuel concentration gradient $\nabla Y_F/\nabla Y_F^0$ is a function of $\cos(\mathrm{atan}^{-1} 2\pi St)$. $\nabla Y_F/\nabla Y_F^0$ decreases with increase in St and approaches to a constant asymptotically. That is to say, the fuel concentration gradient decreases with increase in the sound pressure and frequency in this range.

In the case of $K < 4\pi^2 St$, the cusp is formed. Moreover, the effective width calculated as a function of $\cos(\mathrm{atan}^{-1} 2\pi St)$ is wider than the width which is obtained numerically. From above reasons, $\nabla Y_F/\nabla Y_F^0$ cannot no longer be described $\cos(\mathrm{atan}^{-1} 2\pi St)$.

In the case of $K \ll 4\pi^2 St$, the gap between peak and peak is already filled and it is thought that $\nabla Y_F/\nabla Y_F^0$ is subjected not to St but the amplitude of the fluid motion.

It is notable that $\nabla Y_F/\nabla Y_F^0$ can be determined uniquely by St with same K regardless of the boundary's wave length λ, that is frequency f.

The iso-fuel concentration gradient decreases with increase in the sound pressure. The rate of the change in the height of iso-fuel concentration gradient is classified into three region. In the low St region, the rate of the iso-fuel concentration gradient change is small. In the middle St region, it shows drastic change and it becomes small again in the higher St region. This tendency corresponds with the reduction of the lift-off height with sound pressure. Therefore, the lift-off height decreases with decrease in the fuel concentration gradient with sound.

Summarizing above, it is found that the shape of the mixing layer can be described by new normalized parameter K and acoustic Strouhal number St. It is also found that the fuel concentration gradient decreases with increase in acoustic Strouhal number St and the lift-off height decreases with increase in St due to reduction of fuel concentration gradient. As a future application, this model leads to predict the anchoring location of the flame by employing the concept of the apparent diffusivity which is connected with St.

Nomenclature

ϵ/k^0	Lennard-Jones potential well depth
λ	wave length of meandering boundary
λ_i	heat conductance of species i
$\hat{\mathbf{n}}_{l,y}$	normal unit vector of initial boundary toward to the lean boundary
$\hat{\mathbf{n}}_{u,y}$	normal unit vector of initial boundary toward to the rich boundary
$\mathbf{F}_{l,t}$	boundary shape of fuel lean boundary at time t
$\mathbf{F}_{u,t}$	boundary shape of fuel rich boundary at time t
μ_i	viscosity of species i
Ω	collision integral
$\overrightarrow{g}$	gravitational acceleration
$\overrightarrow{J}_i$	diffusion flux of species i
$\overrightarrow{v}$	velocity
ϕ	equivalence ratio
ρ	gas density
τ_{ij}	stress tensor
$\tilde{a}$	proportional constant of the faster diffusion speed toward to lean or rich boundary

A	amplitude
a	coefficient of the squared term of the fitting curve of the leading edge
a_D	proportional constant of the diffusion speed
a_l	proportional constant of the boundary's development toward to the lower flammability limit boundary
a_u	proportional constant of the boundary's development toward to the upper flammability limit boundary
c_p	heat capacity at constant pressure
D_{ij}	binary diffusivity of species i in species j
E	total energy
f	frequency
h	lift-off height
h_i	enthalpy of species i
K	ratio of mixing layer thickness and wave length of meandering boundary
M_i	molecular weight of species i
p	static pressure
P_S	effective sound pressure
R	gas constant
R_c	curve radius at the peak of the boundary

R_f	curvature radius of the flame's leading edge
St	acoustic Strouhal number
T	temperature
t	time
t_c	time to form the cusp from diffusion initiation
u	local transverse flow velocity
U_u	cross-sectional average flow velocity of unburned gas
v	local streamwise flow velocity
v_D	diffusion speed
v_f	burning velocity
x	transverse coordination to the streamwise direction
X_i	mole fraction of species i
y	streamwise coordination
Y_F	fuel mass fraction
Y_i	mass fraction of species i
Y_l	fuel mass fraction of lower flammability limit
Y_u	fuel mass fraction of upper flammability limit

Acknowledgment

I would like to express my deepest gratitude to Professor Mitsuaki Tanabe, who is the supervisor throughout this study, for the opportunity to conduct this research. I would never achieve my work without his guidance and advices. I would also like to express my sincerest appreciation to Professor Takuo Kuwahara, Professor Akinori Muramatsu of Nihon University and Professor Keiichi Okai of the University of Tokyo who reviewed my thesis. This work was supported by the "Symbolic Project" promoted by College of Science and Technology, Nihon University. I wolud like to thank Professor Mitsutomo Hirota of Muroran Institute of Technology for his great advices on developement of the multi-slot burner and triple flame. I would like to acknowledge Dr. Takamasa Kikuchi of Nihon University for his assistance of schlieren measurement. I would like to thank Mr. Fuminori Nakamura, Assistant Professor of Nihon University, for instruction in writing my thesis. I would also like to thank all the members of Tanabe Laboratory; particularly Mr. Nobuaki Sugiu, Mr. Kazunori Motohashi, Mr. Yuki Yamamoto, Mr. Shigefumi Akita and Mr. Kota Ishii who helped to conduct the experiments and make this work. I am very grateful to my familly for hearty support in all aspects.

References

[1] Sutton, G. P. and Biblarz, O., Rocket Propulsion Elements (Seventh Edition), John Wiley & Sons, Inc., New York, p. 348(2001).

[2] Ben T. Zinn and Timothy C. Lieuwen, Combustion Instabilities: Basic Concepts, Combustion Instabilities in Gas Turbine Engines, Progress in Astronautics and Aeronautics, Vol. 210, AIAA, Reston, VA, p. 6(2005).

[3] Dranovsky, M. L., Yang, V., Culick, F. E. C. and Talley, D. G., Combustion Instabilities in Liquid Rocket Engines, Progress in Astronautics and Aeronautics, Vol. 221, AIAA, Reston, VA, p. 11(2007).

[4] Langhorne, P. J., Reheat Buzz: An Acoustically Coupled Combustion Instability. Part 1. Experiment, J. Fluid Mech., Vol. 193, pp. 417-443.(1988).

[5] Higgins, B., Nicholson's Journal, Vol. 1, p.130(1802).

[6] Rijke, P. L., On the Vibration of the Air in a Tube Open at Both Ends, Philosophical Magazine, Vol. 17, pp. 419-422(1859).

[7] Rayleigh, J. W. S., The Explanation of Certain Acoutical Phenomena1, Nature, Vol. 18, pp. 319-321 (1878).

[8] Rayleigh, J. W. S., The Theoty of Sound, Dover, New York, Vol. 2, p. 226(1945).

[9] Kumagai, S. and Isoda, H., Combustion of Fuel Droplet in a Vibrating Air Field, Proceedings of Fifth Symposium (International) on Combustion, Vol. 5, pp. 129-132(1955).

[10] Tanabe, M., Morita, T., Aoki, K., Satoh, M., Fujimori, T. and Sato, J., Influence of Standing Sound Waves on Droplet Combustion, Proceedings of the Combustion Institute, Vol. 28, pp. 1007-1013(2000).

[11] Tanabe, M., Kuwahara, T., Satoh, K., Fujimori, T., Sato, J. and Kono, M., Droplet Combustion in Standing Sound Waves. Proceedings of the Combustion Institute, Vol. 30, pp. 1957-1964(2005).

[12] Okai, K., Moriue, O., Araki, M., Tsue, M., Kono, M., Sato, J., Dietrich, D. L. and Williams, F. A., Combustion of Single Droplet and Droplet Pairs in a Vibrating Field under Microgravity, Proceedings of the Combustion Institute, Vol. 28, pp. 977-983(2000).

[13] Dattarajan, S., Lutomirski, A., Lobbia, R., Smith, O. I. and Karagozian, A. R., Acoustic Excitation of Droplet Combustion in Microgravity and Normal Gravity, Combustion and Flame, Vol. 144, pp. 299-317(2006).

[14] Sevilla-Esparza, C. I., Wegener, J. L., Teshome, S., Rodriguez, J. I., Smith, O. I. and Karagozian, A. R., Droplet Combustion in the Presence of Acoustic Excitation, Combustion and Flame, Vol. 161, pp. 1604-1619(2014).

[15] Schimmer, H. and Vortmeyer, D., Acoustical Oscillation in a Combustion System with a Flat Flame, Combustion and Flame, Vol. 28, pp. 17-24(1977).

[16] Fleifil, M., Annaswamy, M., Ghoneim, A. and Ghoniem, A. F., Response of a Laminar Premixed Flame to Flow Oscillations: A Kinematic Model and Thermoacoustic Instability Results, Combustion and Flame, Vol. 106, pp. 487-510(1996).

[17] Durox, D., Baillot, F., Searby, G. and Boyer, L., On the Shape of Flames under Strong Acoustic Forcing: A Mean Flow Controlled by an Oscillating Flow, Journal of Fluid Mechanics, Vol. 350, pp.295-310(1997).

[18] Rosdzimin, A. R. D., Yokomori, T. and Ueda, T., The Response of a Conical Laminar Premixed Flame to Equivalence Ratio Oscillations in Rich Conditions, Journal of Thermal Science and Technology, Vol. 8, No. 1, pp. 28-43(2013).

[19] Taniyama, Y. and Fujita, O., Initiation and Formation of the Corrugated Structure Leading to the Self-Turbulization of Downward Propagating Flames in a Combustion Tube with External Laser Absorption, Combustion and Flame, Vol. 161, pp. 1558-1565(2014).

[20] Hantschk, C. -C. and Vortmeyer, D., Numerical Simulation of Self-Excited Combustion Oscillations in a Non-Premixed Burner, Combustion Science and Technology, Vol. 174, pp. 189-204(2002).

[21] Baillot, F., Durox, D. and Proud'homme, R., Experimental and Theoretical Study of a Premixed Vibrating Flame, Combustion and Flame, Vol. 88, pp. 149-168(1992).

[22] Kornilov, V. N., Schreel, K. R. A. M and de Goey, L. P. H., Experimental assessment of the Acoustic Response of Laminar Premixed Bunsen Flames, Proceedings of the Combustion Institute, Vol. 31, pp. 1239-1246(2007).

[23] Kashinath, K., Hemchandra, S. and Juniper, M. P. Nonlinear Thermoacoustics of Ducted Premixed Flames: The Influence of Perturebation Convection Speed, Combustion and Flame, Vol. 160, pp. 2856-2865(2013).

[24] Yu, Y. C., Koeglmeier, S. M., Sisco, J. C. and Anderson, W. E., Combustion Instability of Gaseous Fuels in a Continuously Variable Resonance Chamber

(CVRC), Proceedings of 44th AIAA/ASME/SAE/ASEE Joint Propulsion Conference, AIAA 2008-4657, pp. 1-12(2008).

[25] Yu, Y. C., O'Hara, L., Sisco, J. C. and Anderson, W. E., Experimental Study of High-Frequency Combustion Instability in a Continuously Variable Resonance Combustor (CVRC), Proceedings of 47th AIAA Aerospace Sciences Meeting, AIAA 2009-234, pp. 1-12(2009).

[26] Feldman, T. W., Harvazinski, M. E., Merkle, C. L. and Anderson, W. E., Comparison Between Simulation and Measurement of Self-Excited Combustion Instability, Proceedings of 48th AIAA/ASME/SAE/ASEE Joint Propulsion Conference, AIAA 2012-4088, pp. 1-8(2012).

[27] Cheng Huang, Anderson, W. E., Harvazinski, M. E. and Sankaran, V., Analysis of Self-Excited Combustion Instabilities Using Decomposition Techniques, Proceedings of 51st AIAA Aerospace Sciences Meeting, AIAA 2013-1007, pp. 1-18(2013).

[28] Hester, S., Feldman, T. and Anderson, W. E., High Frequency Signal Analysis Methods for Acoustic Modal Onset in a Continuously Varying Resonance Combustor, Proceedings of 50th AIAA/ASME/SAE/ASEE Joint Propulsion Conference, AIAA 2014-3773, pp. 1-11(2014).

[29] Chung, S. H. and Lee, B. J., On the Characteristics of Laminar Lifted Flames in a Nonpremixed Jet, Combustion and Flame, Vol. 86, pp. 62-72(1991).

[30] Muñiz, L. and Mungal, M. G., Instantaneous Flame-Stabilization Velocities in Lifted-Jet Diffusion Flames, Combustion and Flame, Vol. 111, pp. 16-31(1997).

[31] Chen, M., Herrmann, M. and Peters, N., Flamelet Modeling of Lifted Turbulent Methane/Air and Propane/Air Jet Diffusion Flames, Proceedings of the Combustion Institute, Vol. 28, pp. 167-174(2000).

[32] Mizobuchi, Y., Tachibana, S., Shinio, J., Ogawa, S. and Takeno, T., A Numerical Analysis of the Structure of a Turbulent Hydrogen Jet Lifted Flame, Proceedings of the Combustion Institute, Vol. 29, pp. 2009-2015(2002).

[33] Garby, R., Selle, L. and Poinsot, T., Large-Eddy Simulation of Combustion Instabilities in a Variable-Length Combustor, Comptes Rendus Mecanique, Vol. 341, pp. 220-229(2013).

[34] Harvazinski, M. E., Huang, C., Sankaran, V., Feldman, T. W., Anderson, W. E., Merkle, C. L. and Talley, D. G., Combustion Instability Mechanism in a Pressure-coupled Gas-gas Coaxial Rocket Injector, Proceedings of 49th AIAA/ASME/SAE/ASEE Joint Propulsion Conference, AIAA 2013-3990, pp. 1-21(2013).

[35] Srinivasan, S., Ranjan, R. and Menon, S., Flame Dynamics During Combustion Instability in a High-Pressure, Shear-Coaxial Injector Combustor, Flow, Turbulence and Combustion, (2014).

[36] Nagai, Y., Hirota, M. and Mizomoto, M., Effect of the Flame Curvature on the Burning Velocity of Triple Flame, Transactions of the Japan Society of Mechanical Engineers, B70-691, pp. 780-788(2004).

[37] Plessing, T., Terhoeven, P., Peters, N. and Mansour, M. S., An Experimental and Numerical Study of a Laminar Triple Flame, Combustion and Flame, Vol. 115, pp. 335-353(1998).

[38] Phillips, H., Flame in a Buoyant Methane Layer, Proceedings of Tenth Symposium (International) on Combustion, Vol. 10, pp. 1277-1283(1965).

[39] Hirota, M., Yokomori, T., Yasuda, K., Nagai, Y., Mizomoto, M and Masuya, G., Burning Velocity of Triple Flames with Gentle Concentration Gradient, Proceedings of the Combustion Institute, Vol. 31, pp. 893-899(2007).

[40] Liebman, I., Corry, J. and Perlee, H. E., Flame Propagation in Layered Methane-Air Systems, Combustion Science and Technology, Vol. 1, pp. 257-267(1970).

[41] Law, C. K., Dynamics of Stretched Flame, Proceedings of Tenty-Second Symposium (International) on Combustion, Vol. 22, pp. 1381-1402(1988).

[42] Dold, J. W., Flame Propagation in a Nonuniform Mixture: Analysis of a Slowly Varying Triple Flame, Combustion and Flame, Vol. 76, pp. 71-88(1989).

[43] Kioni, P. N., Rogg, B. and Bray, K. N. C., Flame Spread in Laminar Mixing Layers: The Triple Flame. Combustion and Flame, 95, pp. 276-290(1993).

[44] Hirota, M., Matsuo, A. and Mizomoto, M., Flame Interaction at Leading Edge of a Triple Flame Regarded from the Burning Velocity, Transactions of the Japan Society of Mechanical Engineers, B67-661, pp. 2353-2360(2001).

[45] Guo, H., Liu, F. and Smallwood, G. J., A Numerical Study of Laminar Methane/Air Triple Flames in Two-dimensional Mixing Layer, International Journal of Thermal Sciences, Vol. 45, pp. 586-594(2006).

[46] Ko, Y. S. and Chung, S. H., Propagation of Unsteady Tribrachial Flames in Laminar Non-Premixed Jets, Combustion and Flame, Vol. 118, pp. 151-163(1999).

[47] Ghosal, S and Vervisch, L., Theoretical and Numerical Study of a Symmetrical Triple Flame Using the Parabolic Flame Path Approximation, Journal of Fluid Mechanics, Vol. 415, pp. 227-260(2000).

[48] Qin, X., Puri, I. K. and Aggarwal, S. K., Characteristics of Lifted Triple Flames Stabilized in the Near Field of a Partially Premixed Axisymmetric Jet, Proceedings of the Combustion Institute, Vol. 29, pp. 1565-1572(2002).

[49] Lee, J., Won, S. H., Jin, S. H., Chung, S. H, Fujita, O. and Ito, K., Propagation Speed of Tribrachial (Triple) flame of Propane in Laminar Jets under Normal and Micro Gravity Conditions, Combustion and Flame, Vol. 134, pp. 411-420(2003).

[50] Kim, N. I., Seo, J. I., Oh, K. C and Shin, H. D., Lift-off Characteristics of Triple Flame with Concentration Gradient, Proceedings of the Combustion Institute, Vol. 30, pp. 367-374(2005).

[51] Kim, N. I., Seo, J. I., Guahk, Y. T. and Shin, H. D., The Propagation of Tribrachial flames in a Confined Channel, Combustion and Flame, Vol. 146, pp. 168-179(2006).

[52] Noda, S. and Yamamoto, S., Identification of Triple Flame Based on Numerical Data for Laminar Lifted Flames, JSME International Journal Series B, Vol. 49, pp. 847-855(2006).

[53] Seo, J. I., Kim, N. I. and Shin, H. D., An Experimental Study of Fuel Dilution Effect on the Propagation of Methane-Air Tribrachial flames, Combustion and Flame, Vol. 153, pp. 355-366(2008).

[54] Mulla, I. A. and Chakravarthy, S. R., Propagation Velocity and Flame Stretch Measurement in Co-Flowing Partially Premixed Flames with Widely Varying Premixedness, Combustion and Flame, Vol. 160, pp. 1345-1356(2013).

[55] Mulla, I. A. and Chakravarthy, S. R., Flame Speed and Tangential Strain Measurements in Widely Stratified Partially Premixed Flames Interacting with Grid Turbulence, Combustion and Flame, Vol. 161, pp. 2406-2418(2014).

[56] Chung, S. H. and Law, C. K., An Inveriant Derivation of Flame Stretch, Combustion and Flame, Vol. 55, pp. 123-125(1984).

[57] Echekki, T. and Chen, J. H., Structure and Propagation of Methane-Air Triple Flame, Combustion and Flame, Vol. 114, pp. 231-245(1998).

[58] Im, H. G. and Chen, J. H., Structure and Propagation of Triple Flames in Partially Premixed Hydrogen-Air Mixtures, Combustion and Flame, Vol. 119, pp. 436-454(1999).

[59] Briones, A. M.n Aggarwal, S. K. and Katta, V. R., Effects of H_2 Enrichment on the Propagation Characteristics of CH_4-Air Triple Flames, Combustion and Flame, Vol. 153, pp. 367-383(2008).

[60] Owston, R. and Abraham, J., Structure of Hydrogen Triple Flames and Premixed Flames Compared, Combustion and Flame, Vol. 157, pp. 1552-1565(2010).

[61] Chao, Y. and Jeng, M., Behavior of the Lifted Jet Flame under Acoustic Excitation, Proceedings of Tenty-Forth Symposium (International) on Combustion, Vol. 24, pp. 333-340(1992).

[62] Hirota, M., Hashimoto, K., Oso, H. and Masuya, G., Improvement of Laminer Lifted Flame Stability Excited by High-Frequency Acoustic Oscillation, Journal of Thermal Science and Technology, Vol. 4, pp. 169-177(2009).

[63] Masuda, W., Hishida, M., Hori, T. and Yamane, K., Characteristics of Methane Jet-Diffusion Flame Excited by an Acoustic Wave, Nensho no Kagaku to Gijyutsu, Vol. 6, pp. 263-272(1999).

[64] Suzuki, M., Atarashi, T. and Masuda, W., Behavior and Structure of Internal Fuel-Jet in Diffusion Flame under Transverse Acoustic Excitation, Combustion Science and Technology, Vol. 179, pp. 2581-2597(2007).

[65] Suzuki, M., Umeda, T., Hamatani, T. and Masuda, W., Velocity Profile of Bifurcating Jet Inside Diffusion Flame under Acoustic Excitation, Journal of the Combustion Society of Japan, Vol. 51, pp. 217-222(2009).

[66] Oster, D. and Wygnanski, I., The Forced Mixing Layer Between Parallel Streams, Journal of Fluid Mechanics, Vol. 123, pp. 91-130(1982).

[67] Davis, M. R. and Lin, L. H., Structures Induced by Periodic Acoustic Excitation of a Diffusion Flame, Combustion and Flame, Vol. 103, pp. 151-160(1995).

[68] Chao, Y., Wu, C. and Yuan, T., Stabilization Process of a Lifted Flame Tuned by Acoustic Excitation, Combustion Science and Technology, Vol. 174, pp. 87-110(2002).

[69] Demare, D. and Baillot, F., Acoustic Enhancement of Combustion in Lifted Nonpremixed Jet Flames, Combustion and Flame, Vol. 139, pp. 312-328(2004).

[70] Ichimiya, M., Kamada, S., Okajima, A and Osaki, T., Effect of Local Periodic Disturbance on Mixing Layer Downstream of Two-Dimensional Jet, Transactions of the Japan Society of Mechanical Engineers, B77-779, pp. 48-62(2011).

[71] Ichimiya, M., Kato, T. and Morimoto, T., Effect of Local Periodic Disturbance on Mixing Layer at Exit of Two-Dimensional Jet, Journal of Fluid Science and Technology, Vol. 6, No. 6, pp. 887-901(2011).

[72] Vanquickencborne, L. and Tiggelen, A. V., The Stabilization Mechanism of Lifted Diffusion Flames, Combustion and Flame, Vol. 10, pp. 59-69(1966).

[73] Lewis, B and von Elbe, G., Combustion, Flame and Explosions of Gases, Academic Press, New York & London, pp. 692-694(1961).

[74] Giepman, R., Lynch, K., Schrijer, F and van Oudheusden, B., Investigation of a transitional Oblique Shock Wave Reflection Using PIV, 17th International Symposium on Applications of Laser Techniques to Fluid Mechanics, pp. 1-17(2014).

[75] Scarano, F. and Riethmuller, M. L., Advances in Iterative Multigrid PIV image Processing, Experiments in Fluids, Vol. 29, pp. 51-60(2000).

[76] Patankar, S. V. and Spalding, D. B., A Calculation Procedure for Heat, Mass and Momentam Transfer in Three-dimensional Paraboric Flows, International Jounal of Heat Mass Transfer, Vol. 15, p. 1787(1972).

[77] Leer, B. V., Toward the Ultimate Concervative Difference Scheme. IV. A Second Order Sequel to Godunov's Method, Journal of Computational Physics, Vol. 32, pp. 101-136(1979).

[78] Law, C. K., Combustion Physics. Cambridge University Press, New York, pp. 152-153(2006).

[79] Poling, B. E., Prausnitz, J. M. and O'Connel, J. P., The Property of Gases and Liquids, Fifth Edition, McGraw-Hill, New York, pp. 11.5-11.7(2001).

[80] The U. S. Standard Atmosphere, National Oceanic and Atmospheric Administration, U. S. Goverment Printing Office, p. 3(1976).

[81] Glassman, I. and Yetter, R. A., Combustion Forth Edition, Academic Press, Burlington, MA, p. 169(2008).

[82] Wang, W. and Lyons, K. M., Leading-Edge Velocities and Lifted Methane Jet Flame Stability, Journal of Combustion, Vol. 2010, pp. 1-10(2010).

[83] Einstein, A., Investigations on the Theory of the Brownian Movement, Dover Publications, Inc., New York, p. 17(1956).

[84] Shlesinger, M. F., Klafter, J. and Zumofen, G., Above, Below and Beyond Brownian Motion, American Journal of Physics, Vol. 67, p. 1253(1999).

[85] Ishino, Y., Saiki, Y., Kataoka, M., Inaba, K. and Ohiwa, N, Micro-Gravity Experiment on a Baroclinique Torque Generated by 2D Vortex-Pair Penetration into a Binary-Density Stratified Planar Boundary, Transactions of the Japan Society of Mechanical Engineers, B76-762, pp. 319-325(2010).

[86] Hirosawa, T., Kusakawa, H., Yamada, H., Takizawa, W., Mano, Y., Kuwahara, T. and Tanabe, M., Roles of Baroclinic Torque by Acoustic Oscillation on Structure of Premixed Flame, Proceedings of 50th AIAA Aerospace Sciences Meeting, AIAA 2012-0341, pp. 1-9(2012).

Tables

Table 2-1-1 Experimental conditions

ϕ	Methane	Propane
Equivalence ratio ϕ	2.8 - 3.4	
Flow velocity U_u [m/s]	1.0	1.3
Sound pressure P_S [kPa]	0 - 0.12	
Frequency f [kHz]	0.5	

Table 2-1-2 Reynolds number of the jets (298.15 K, 1 atm)

Gas	Methane/air		Propane/air		Air		Nitrogen	
Equivalence ratio ϕ	2.8	3.4	2.8	3.4				
Flow speed U_u [m/s]	1.0		1.3		1.0	1.3	1.0	1.3
Re	6.21×10^2	6.18×10^2	9.61×10^2	9.70×10^2	6.36×10^2	8.27×10^2	6.36×10^2	8.27×10^2

Table 2-1-3 Fuel mass fractions of flammability limits

Fuel	CH_4	C_3H_8
Y_u	0.0894	0.1383
Y_l	0.0284	0.0320

Table 2-1-4 Initial conditions for numerical calculation of case 1

Fuel	Methane	Propane
Equivalence ratio ϕ	3.0	
Flow velocity U_u [m/s]	1.0	1.3
Sound pressure P_S [kPa]	0.06, 0.10	
Frequency f [kHz]	0.5	

Table 2-1-5 Initial conditions for numerical calculation of case 2

Fuel	Propane
Equivalence ratio ϕ	3.0
Amplitude A [mm]	0.25, 0.5, 1.0
Wave length of boundary λ [mm]	0.65, 1.3, 2.6

Table 2-1-6 Thermodynamic coefficients of polynomial for calculation of specific heat

Species	a_1	a_2	a_3	a_4	a_5
CH_4	4.035847×10^{2}	9.057335	-1.442509×10^{-2}	1.580519×10^{-5}	-6.343051×10^{-9}
C_3H_8	1.691106×10^{2}	5.032259	-1.024072×10^{-3}	-4.008482×10^{-6}	1.74279×10^{-9}
N_2	9.79043×10^{2}	0.4179639	-1.176279×10^{-3}	1.67439×10^{6}	$-7.256297 \times 10^{-10}$
O_2	8.348265×10^{2}	0.292958	-1.495637×10^{-4}	3.413885×10^{-7}	$-2.2783587 \times 10^{-10}$

Table 2-1-7 Molecular weight

Species	M
CH_4	16.04303 [80]
C_3H_8	44.09
N_2	28.0134 [80]
O_2	31.9988 [80]

Table 2-1-8 Lennerd-Jones potential

Species	ϵ/k	σ
CH_4	141.000	3.746
C_3H_8	266.800	4.982
N_2	97.530	3.621
O_2	107.400	3.458

Figures

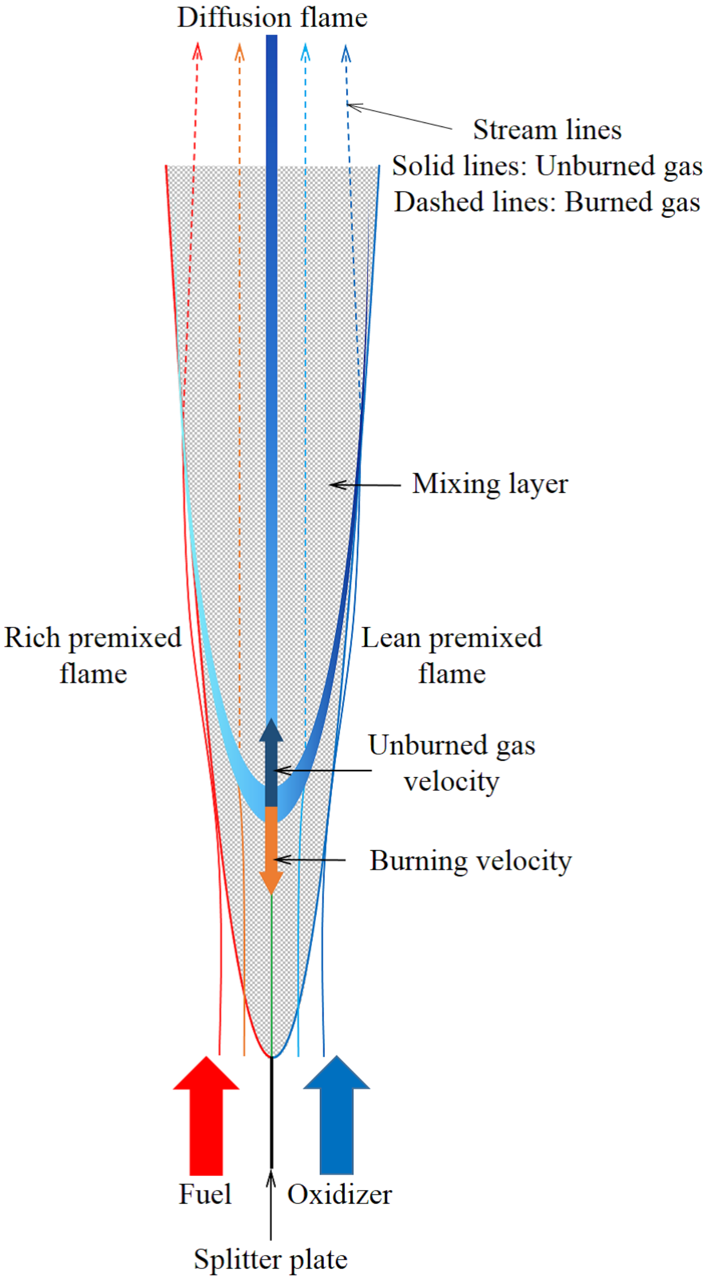

Figure 1-1-1 Schematic of triple flame

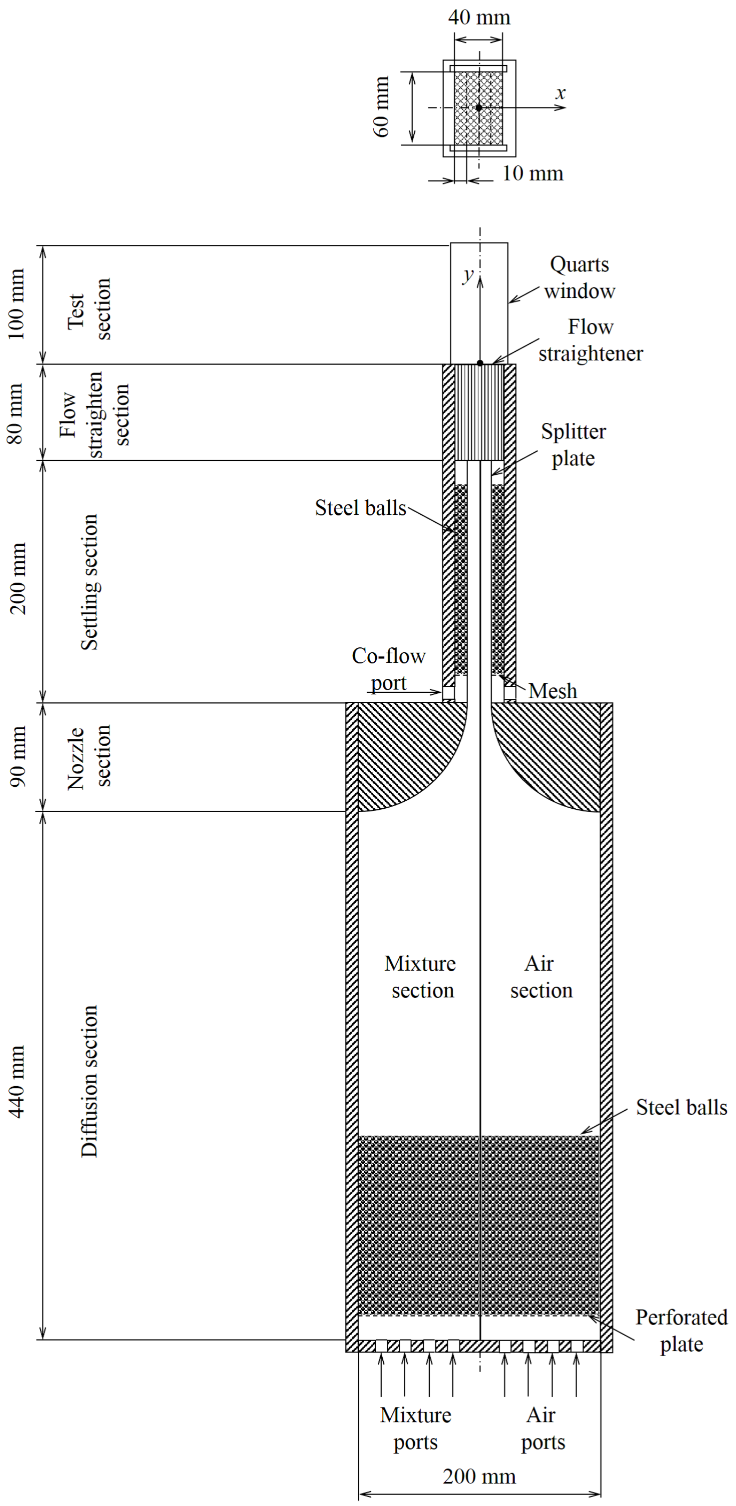

Figure 2-1-2 Multi-slot burner

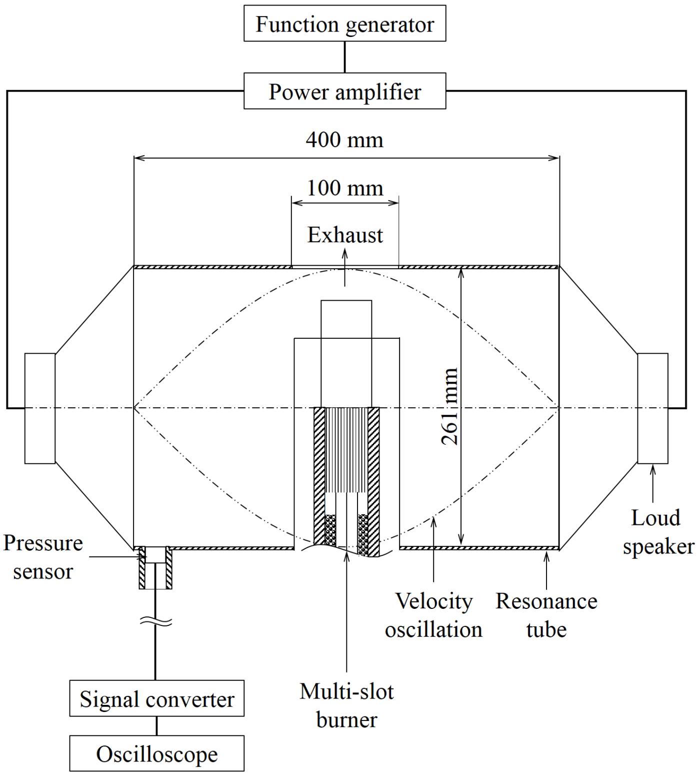

Figure 2-1-3 Schematic of the sound system

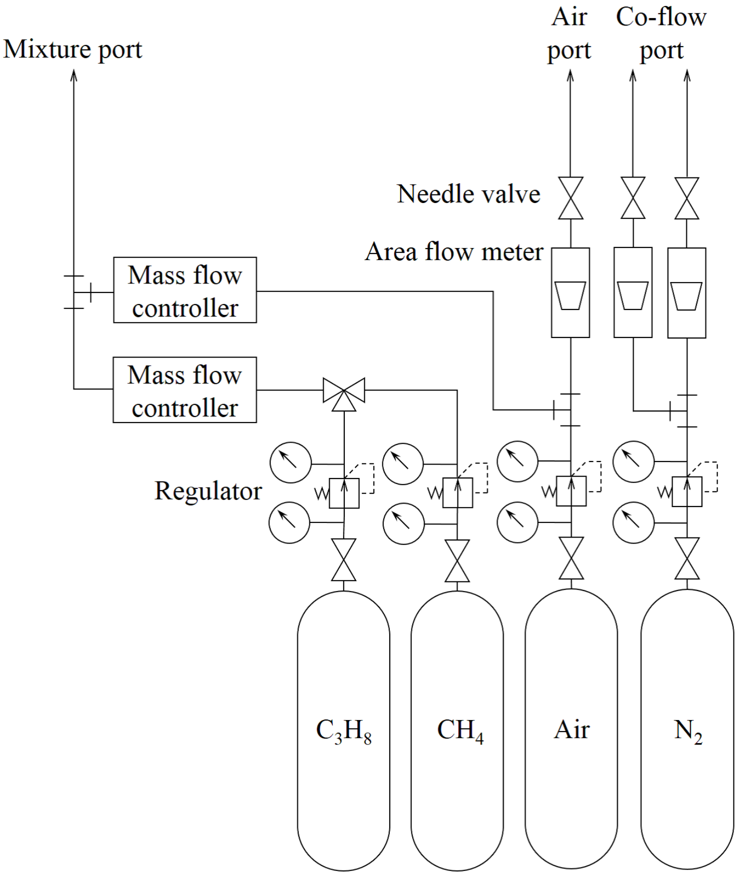

Figure 2-1-4 Gas supply system

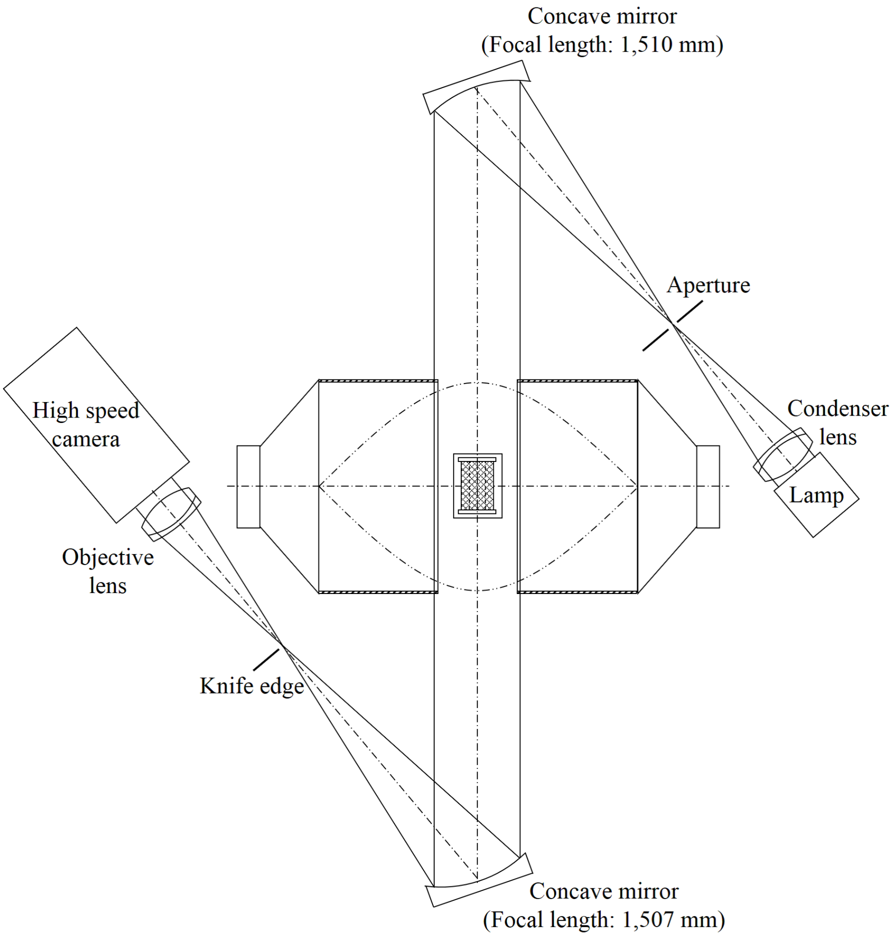

Figure 2-1-5 Schematic of schlieren optics arrangement (top view)

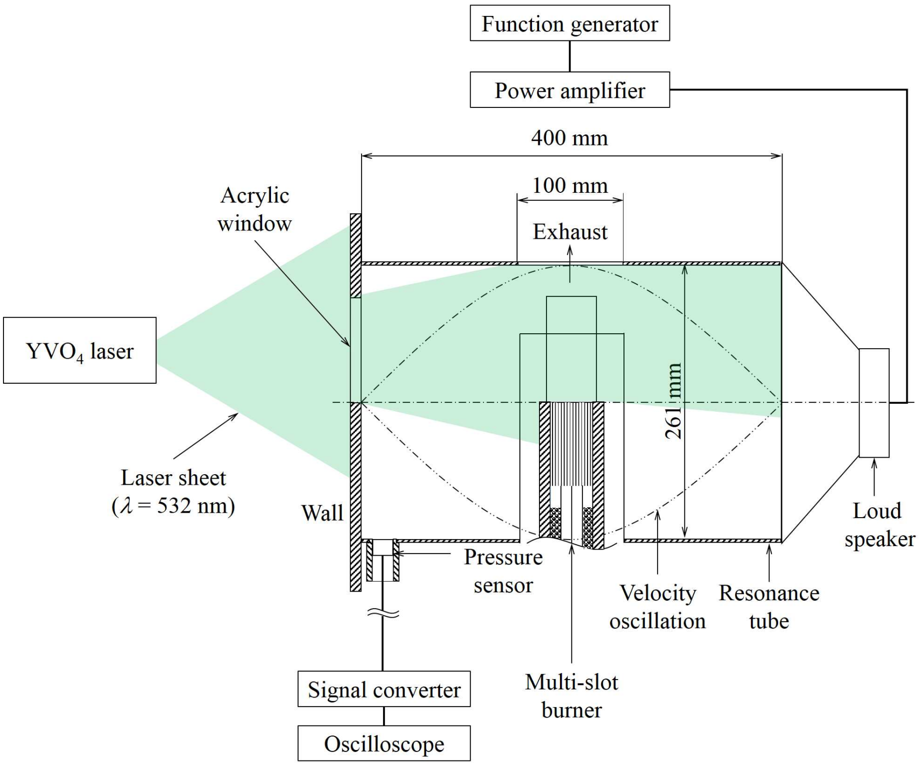

Figure 2-1-6 Schematic of PIV arrangement

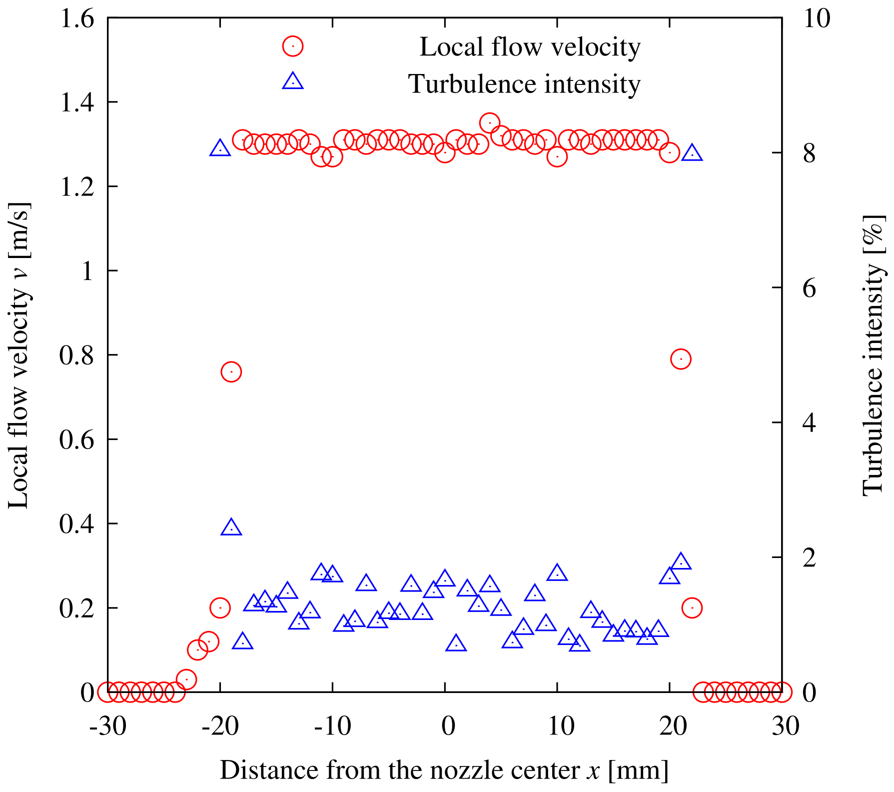

Figure 2-3-1 Distribution of local flow speed and turbulence intensity (y =5 mm)

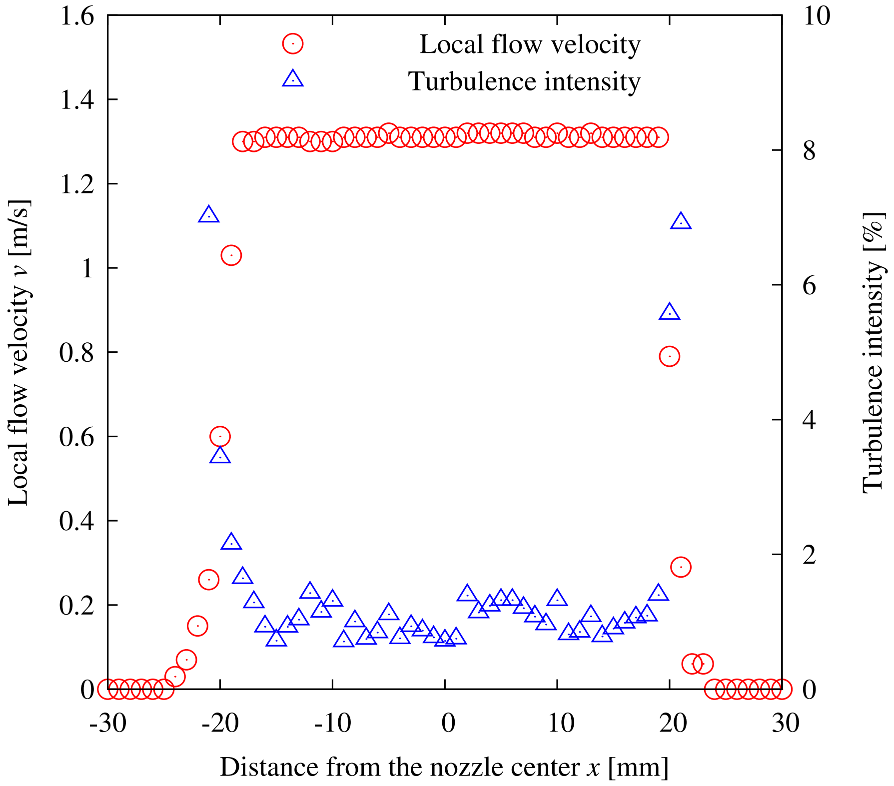

Figure 2-3-2 Distribution of local flow speed and turbulence intensity (y =25 mm)

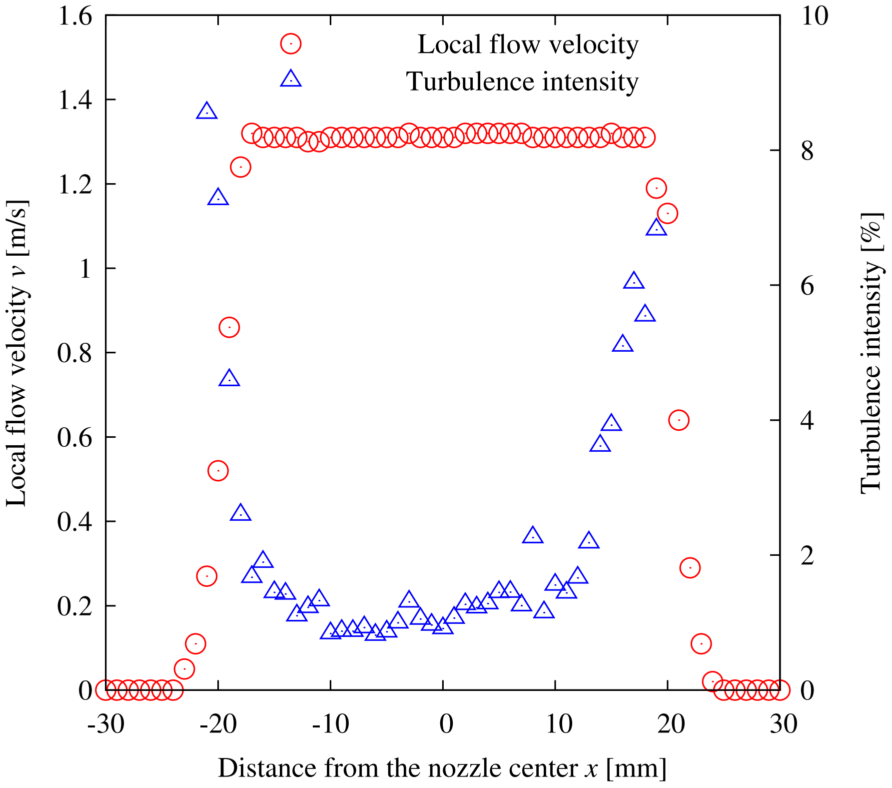

Figure 2-3-3 Distribution of local flow speed and turbulence intensity (y =50 mm)

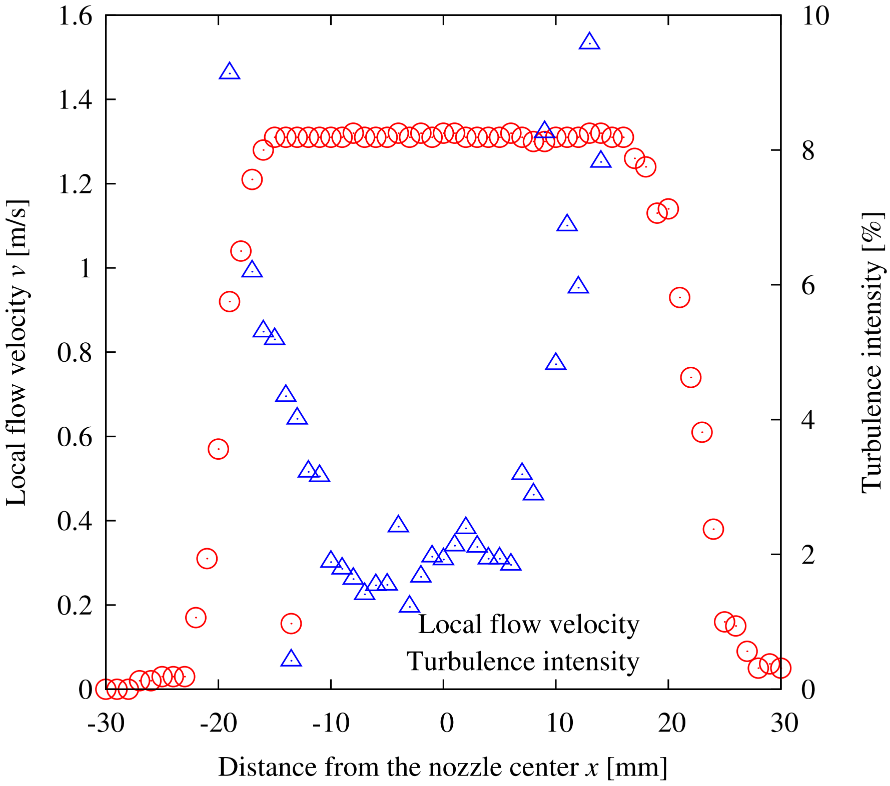

Figure 2-3-4 Distribution of local flow speed and turbulence intensity (*y* =75 mm)

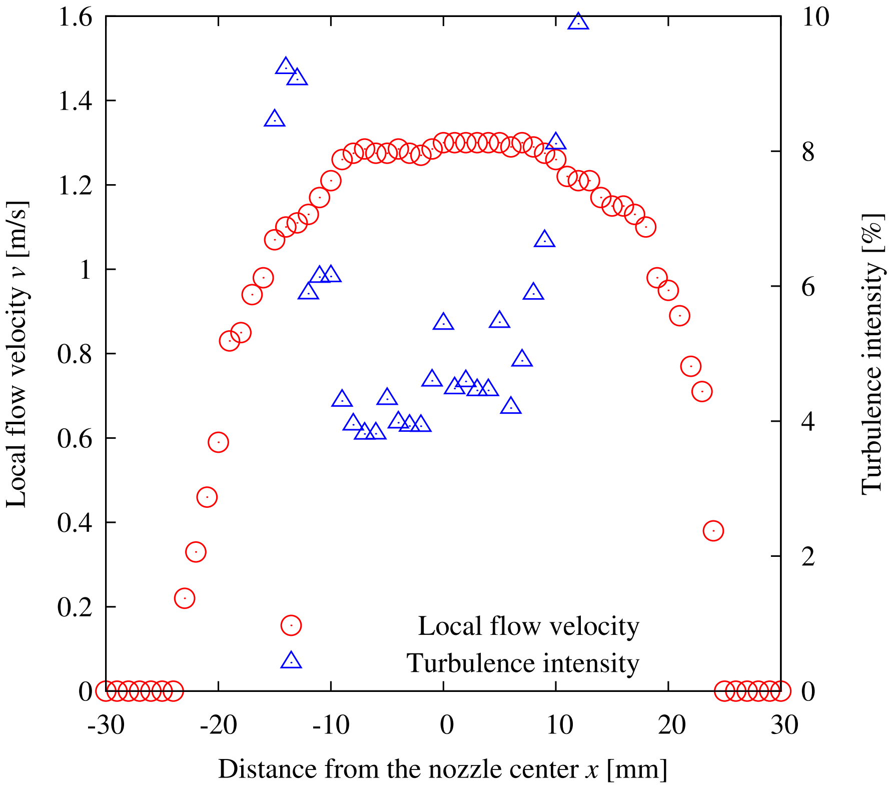

Figure 2-3-5 Distribution of local flow speed and turbulence intensity (*y* =100 mm)

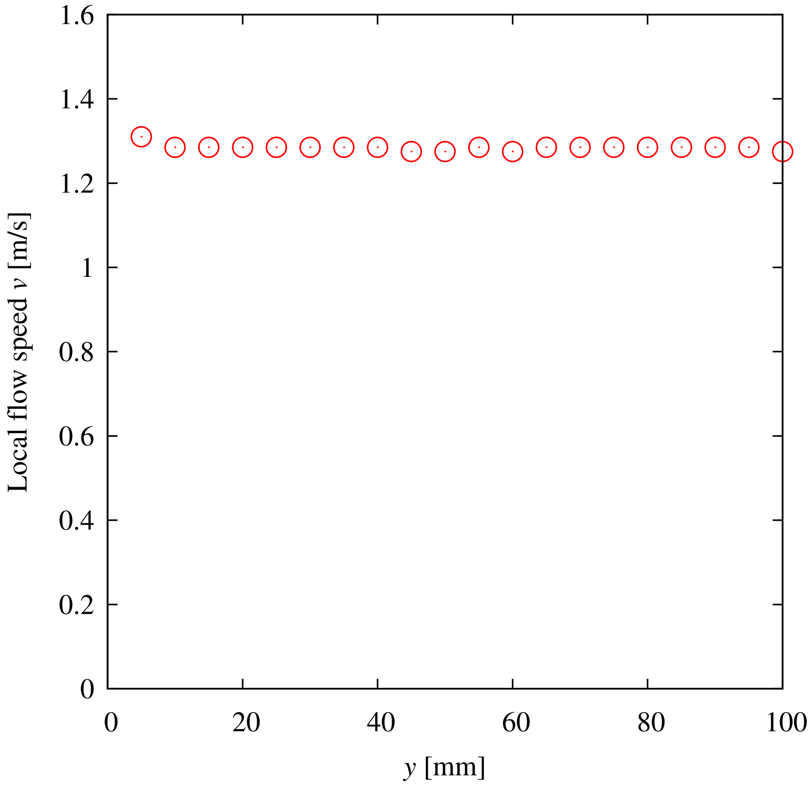

Figure 2-3-6 Distribution of local flow speed along streamwise (x =0 mm)

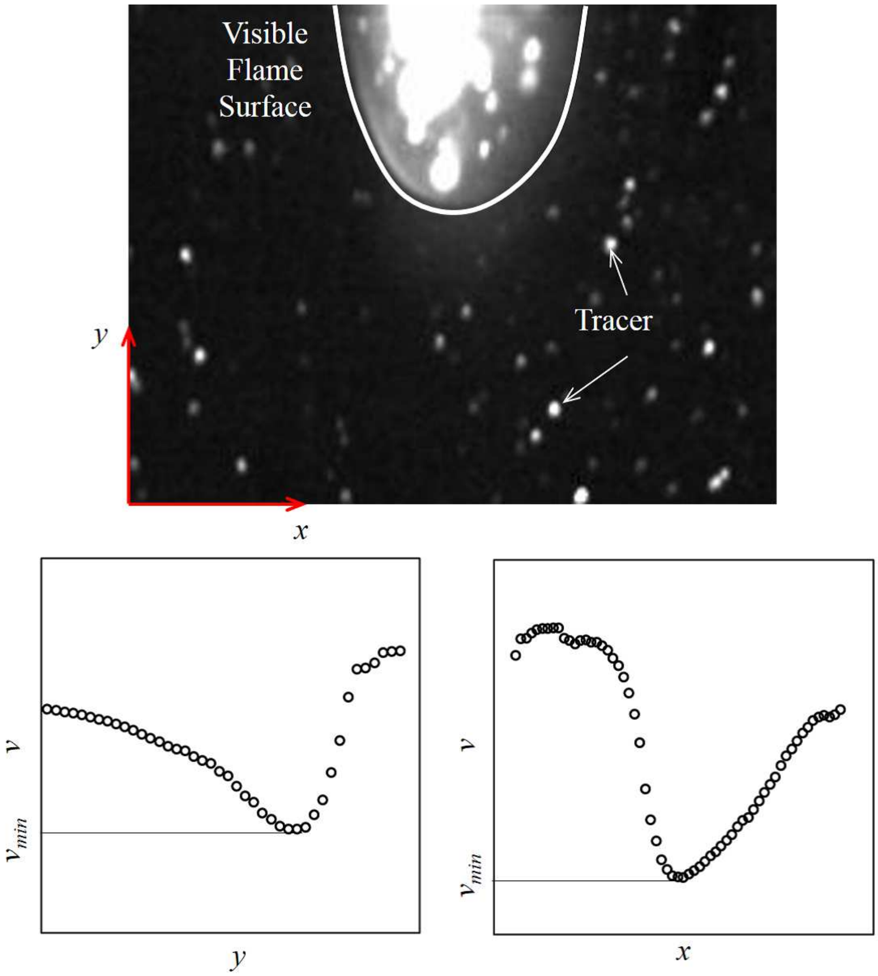

Figure 2-4-1 Raw image of PIV and schematic of flow speed distribution in the vicinity of the leading edge of triple flame

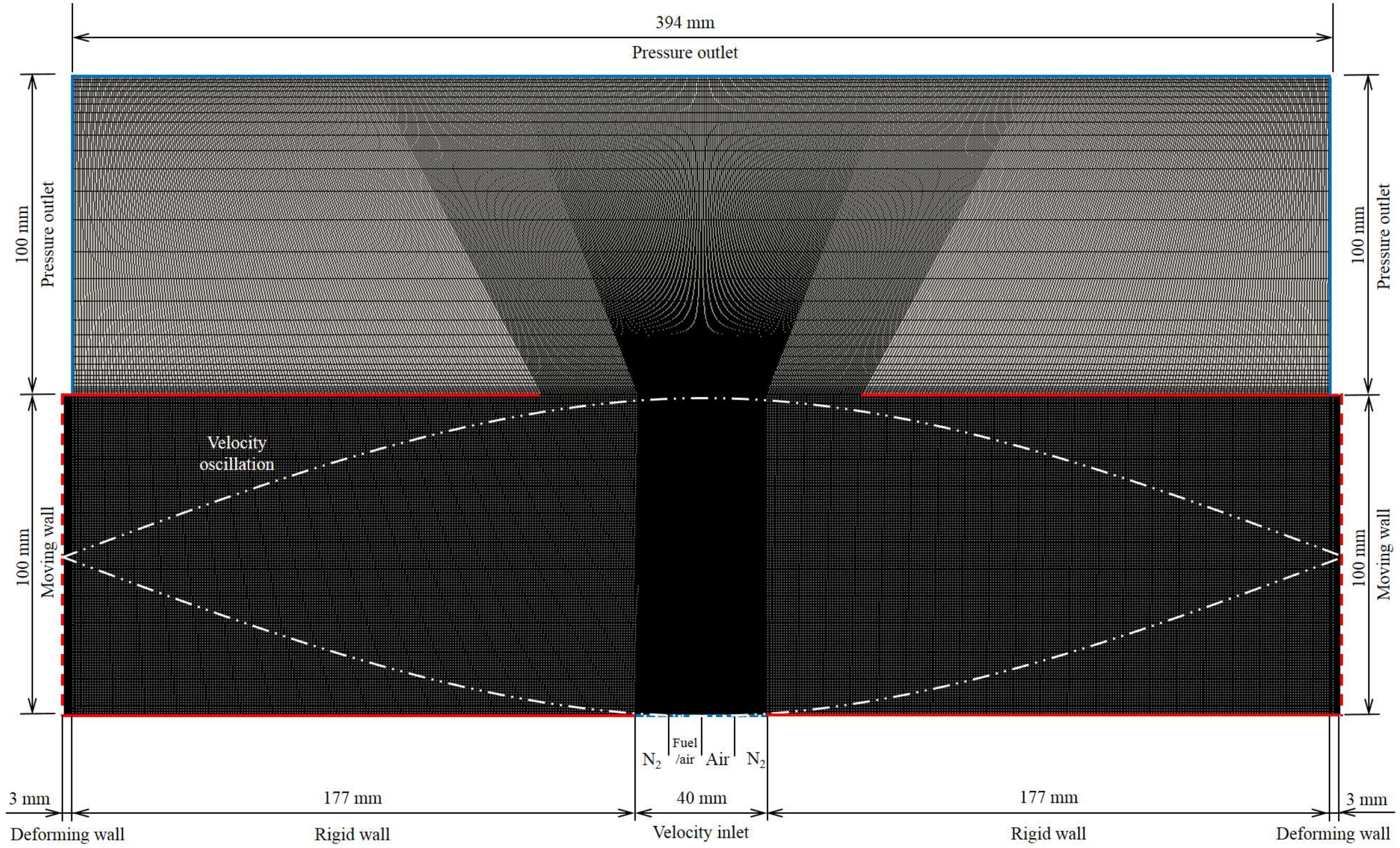

Figure 3-1-1 Computational domain (case1)

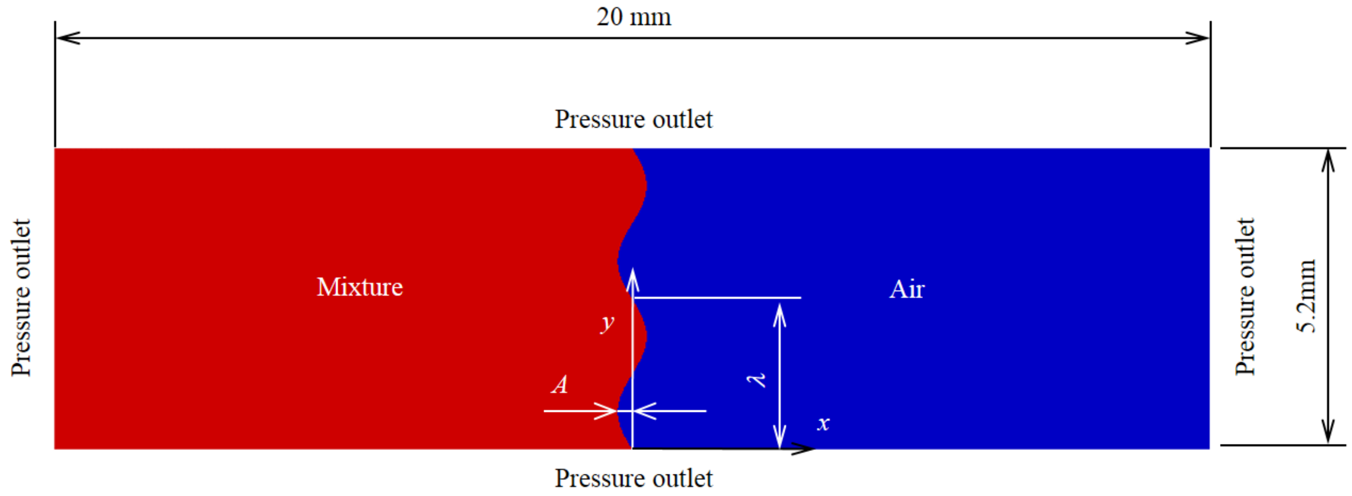

Figure 3-1-2 Computational domain (case2)

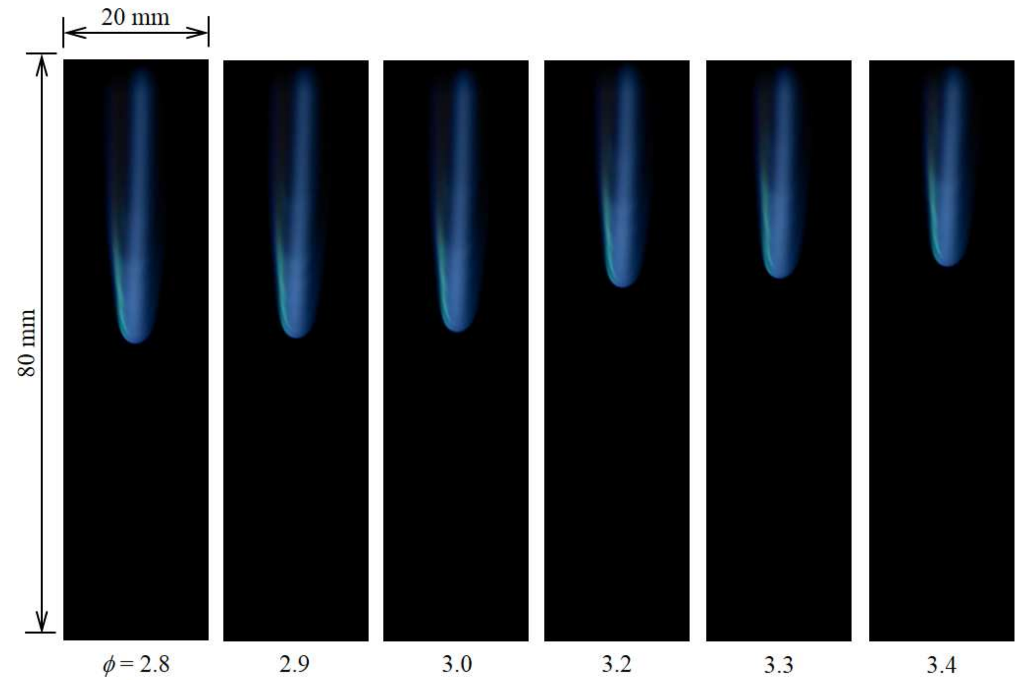

Figure 4-1-1 Direct images of the triple flame with various equivalence ratios without sound (CH_4)

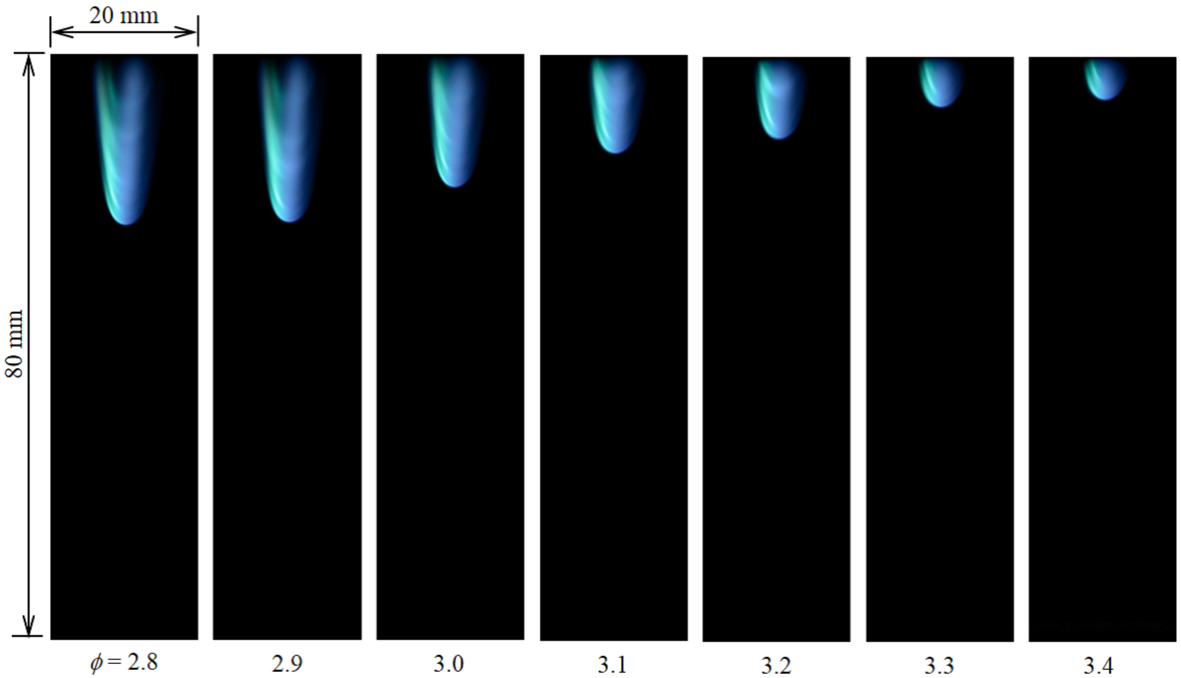

Figure 4-1-2 Direct images of the triple flame with various equivalence ratios without sound (C_3H_8)

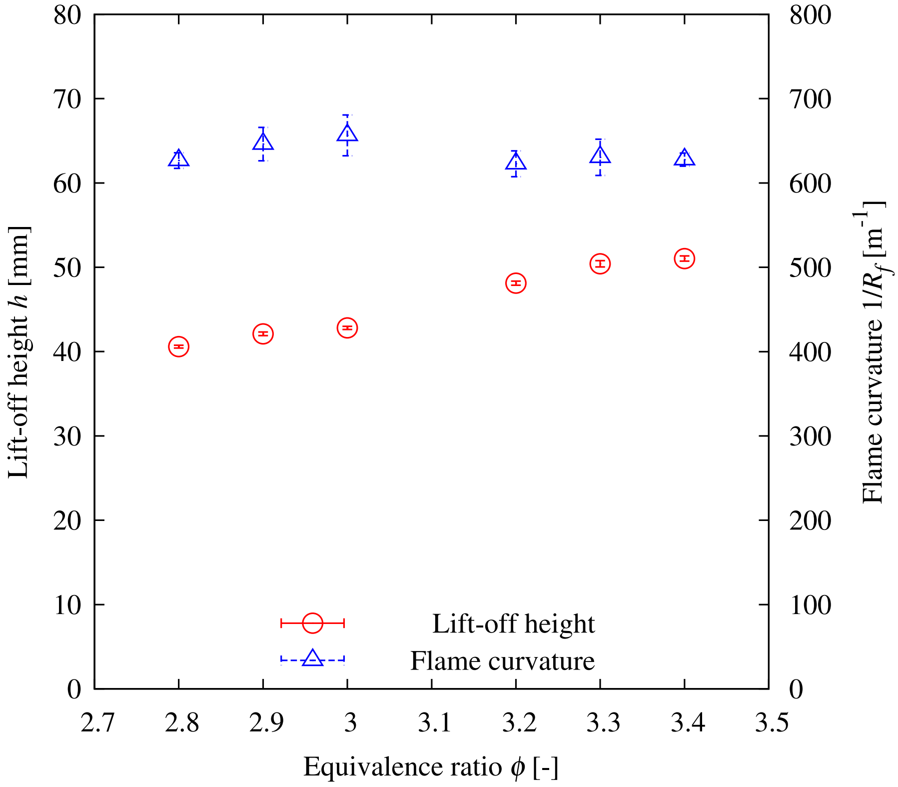

Figure 4-1-3 Flame curvature and lift-off height with various equivalence ratios without sound (CH_4, error bar: average ± S. D.)

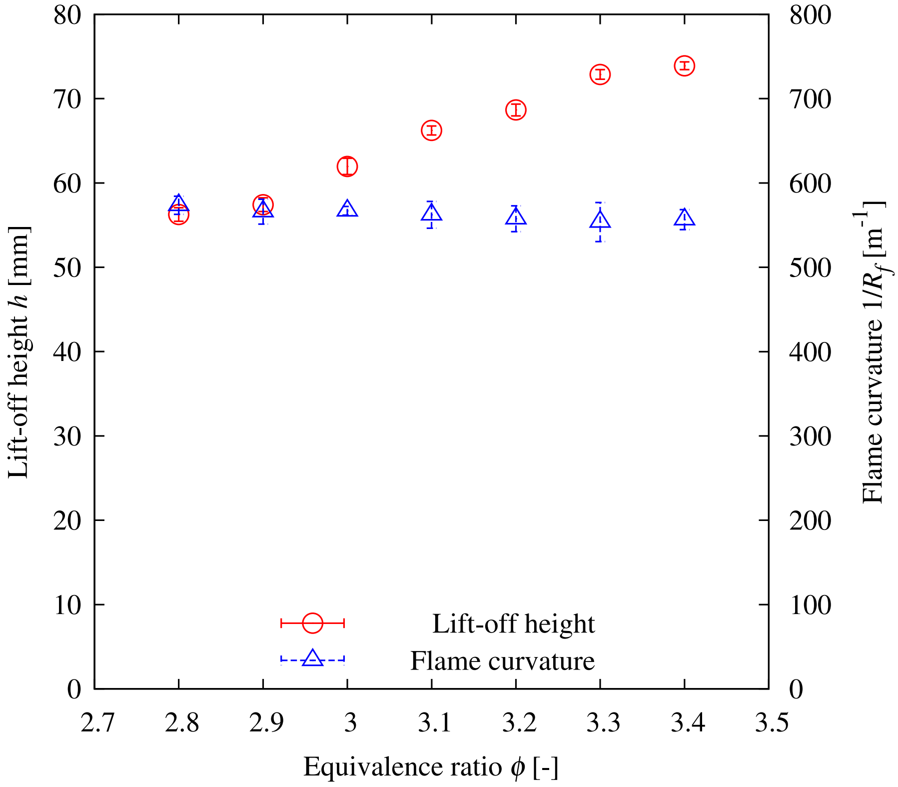

Figure 4-1-4 Flame curvature and lift-off height with various equivalence ratios without sound (C_3H_8, error bar: average ± S. D.)

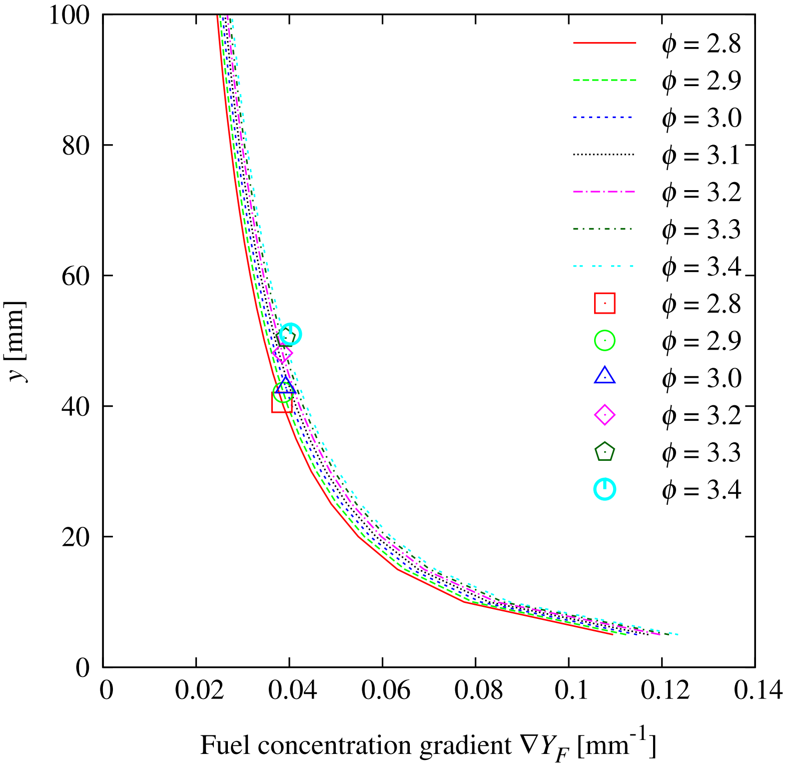

Figure 4-2-1 Calculated distribution of fuel concentration gradient with experimental results of the lift-off height (CH_4)

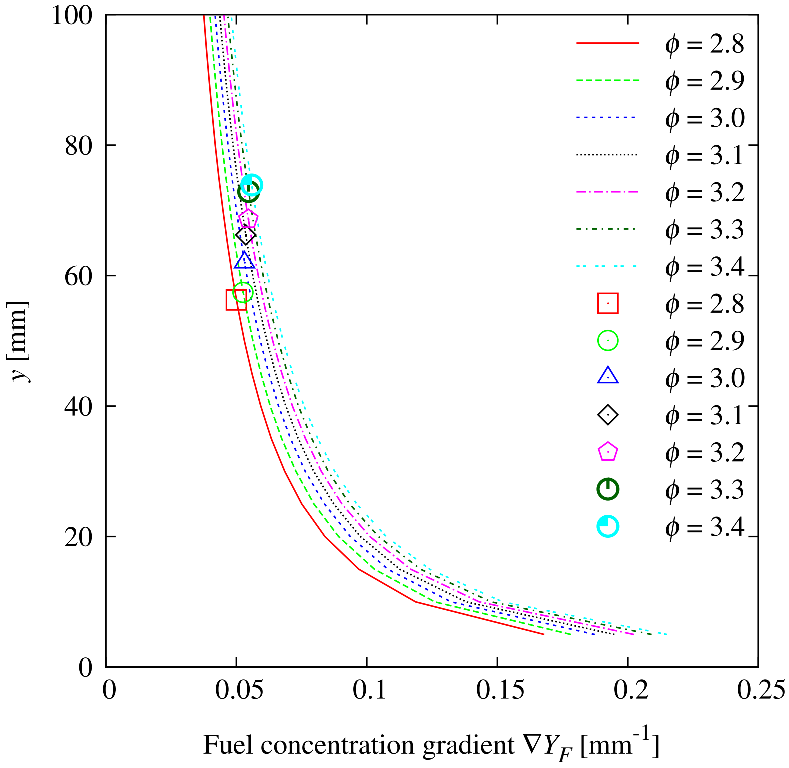

Figure 4-2-2 Calculated distribution of fuel concentration gradient with experimental results of the lift-off height (C_3H_8)

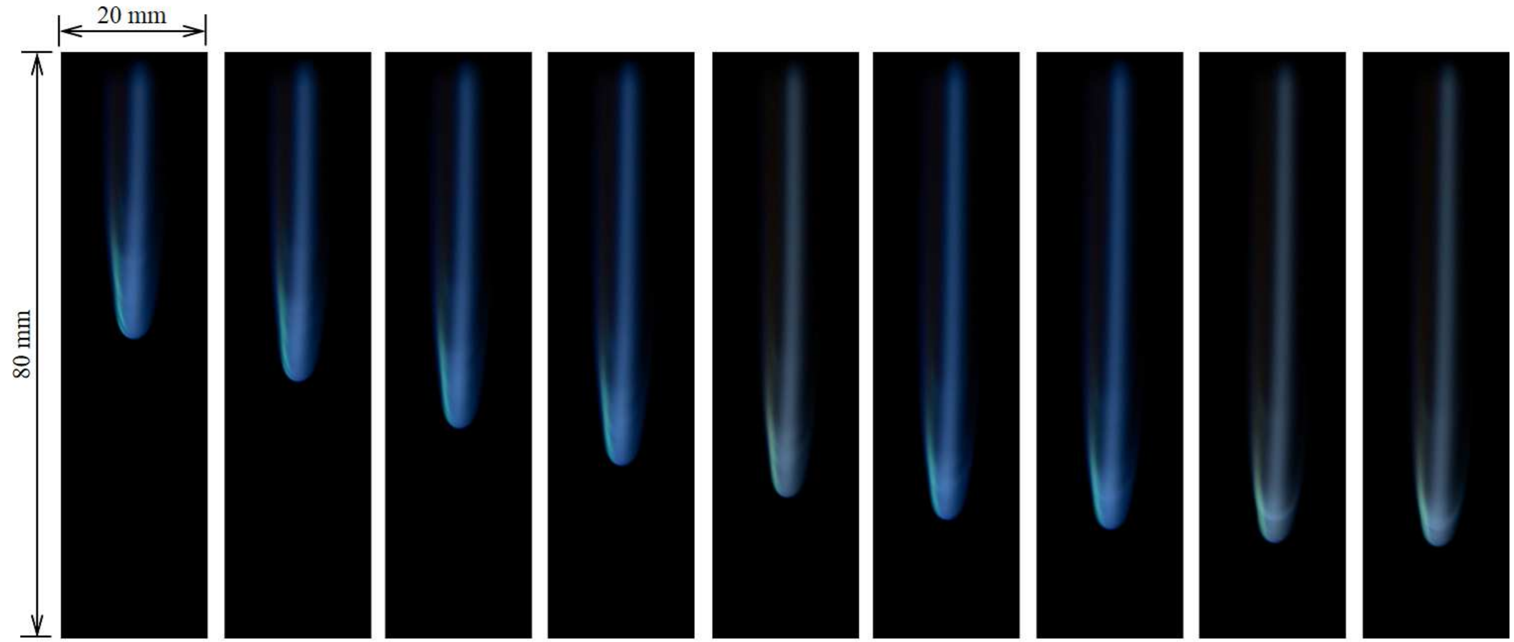

$P_S = 0$ 0.04 kPa 0.06 kPa 0.07 kPa 0.08 kPa 0.09 kPa 0.10 kPa 0.11 kPa 0.12 kPa

Figure 5-1-1 Direct images of the triple flame with various sound pressures (CH_4, ϕ =2.8)

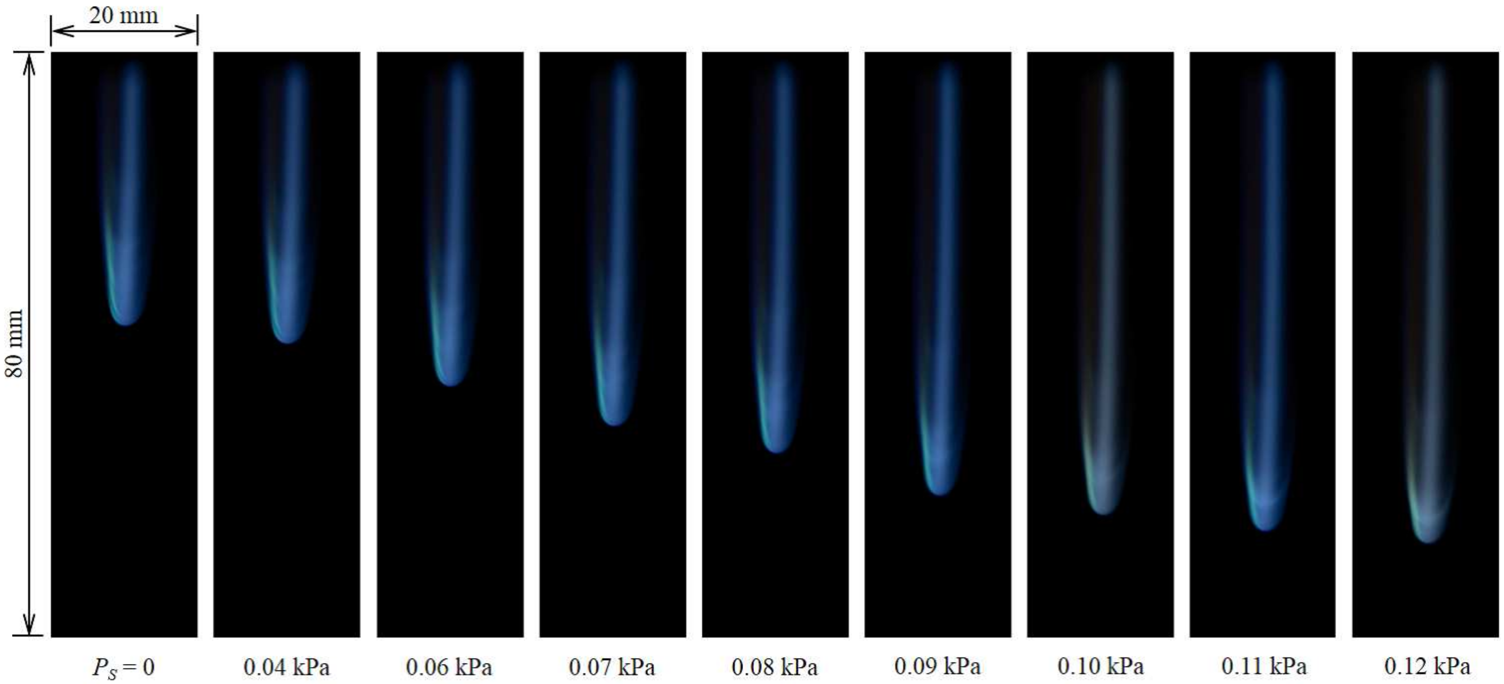

Figure 5-1-2 Direct images of the triple flame with various sound pressures (CH_4, ϕ =3.0)

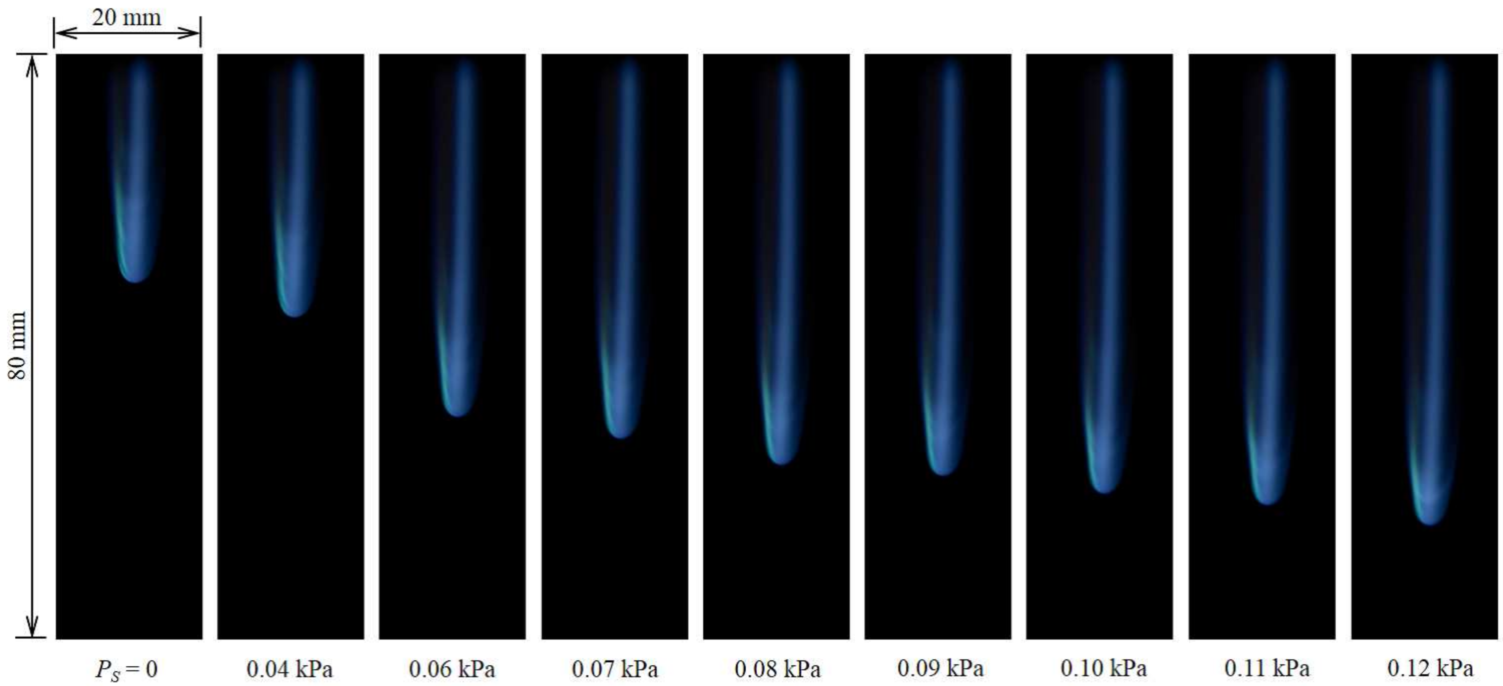

Figure 5-1-3 Direct images of the triple flame with various sound pressures (CH_4, ϕ =3.2)

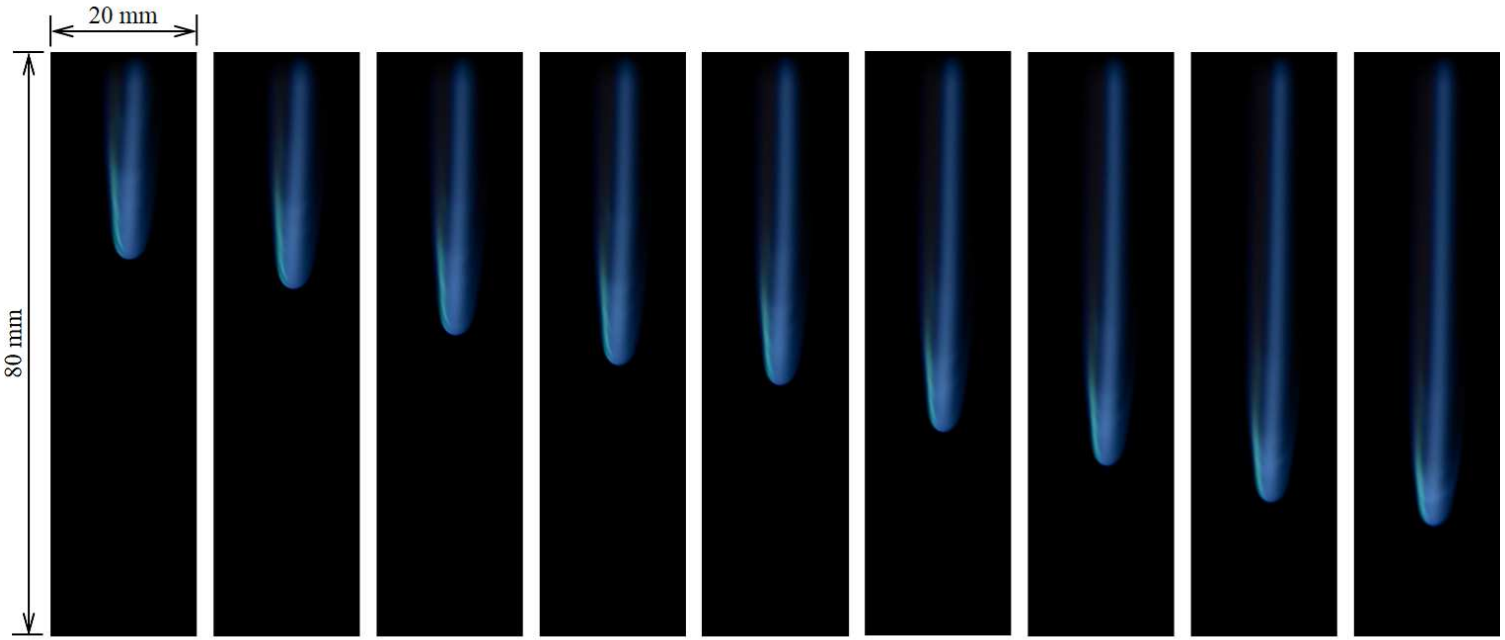

$P_S = 0$ 0.04 kPa 0.06 kPa 0.07 kPa 0.08 kPa 0.09 kPa 0.10 kPa 0.11 kPa 0.12 kPa

Figure 5-1-4 Direct images of the triple flame with various sound pressures (CH_4, ϕ =3.4)

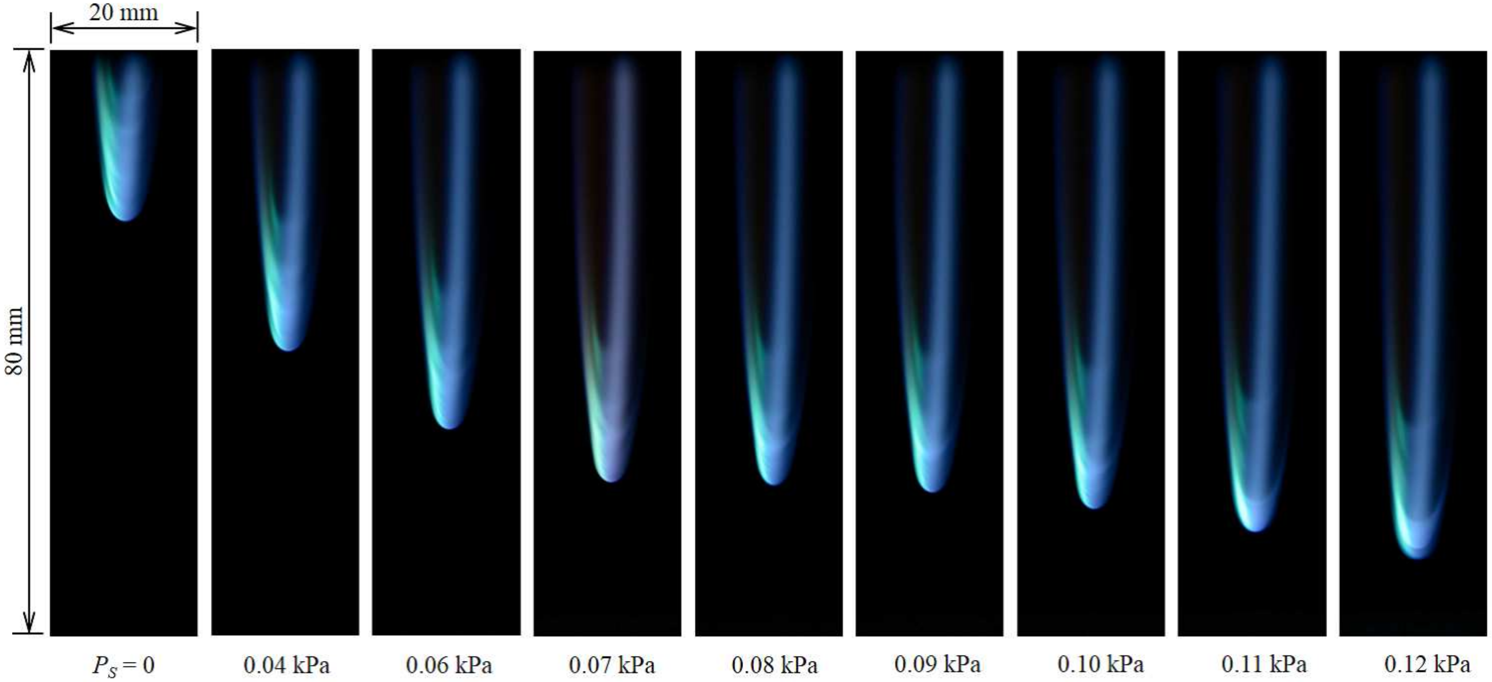

Figure 5-1-5 Direct images of the triple flame with various sound pressures (C_3H_8, ϕ =2.8)

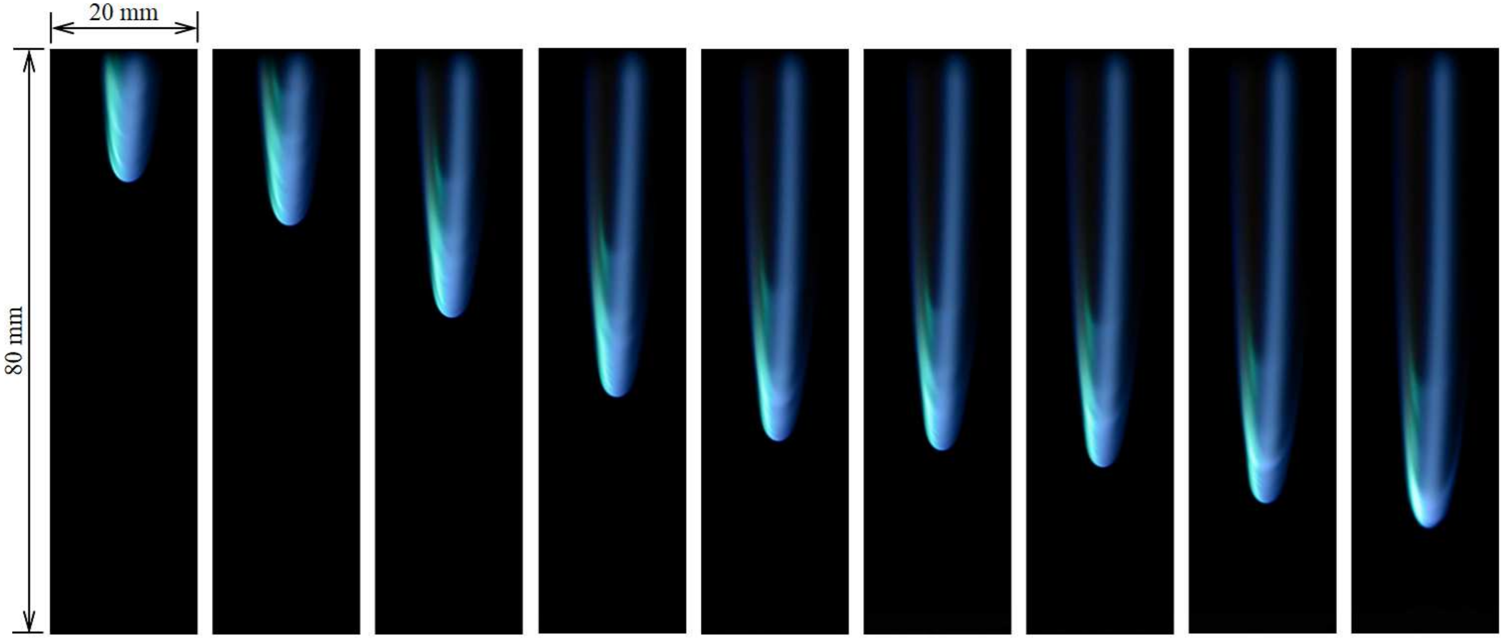

$P_S = 0$ 0.04 kPa 0.06 kPa 0.07 kPa 0.08 kPa 0.09 kPa 0.10 kPa 0.11 kPa 0.12 kPa

Figure 5-1-6 Direct images of the triple flame with various sound pressures (C_3H_8, ϕ =3.0)

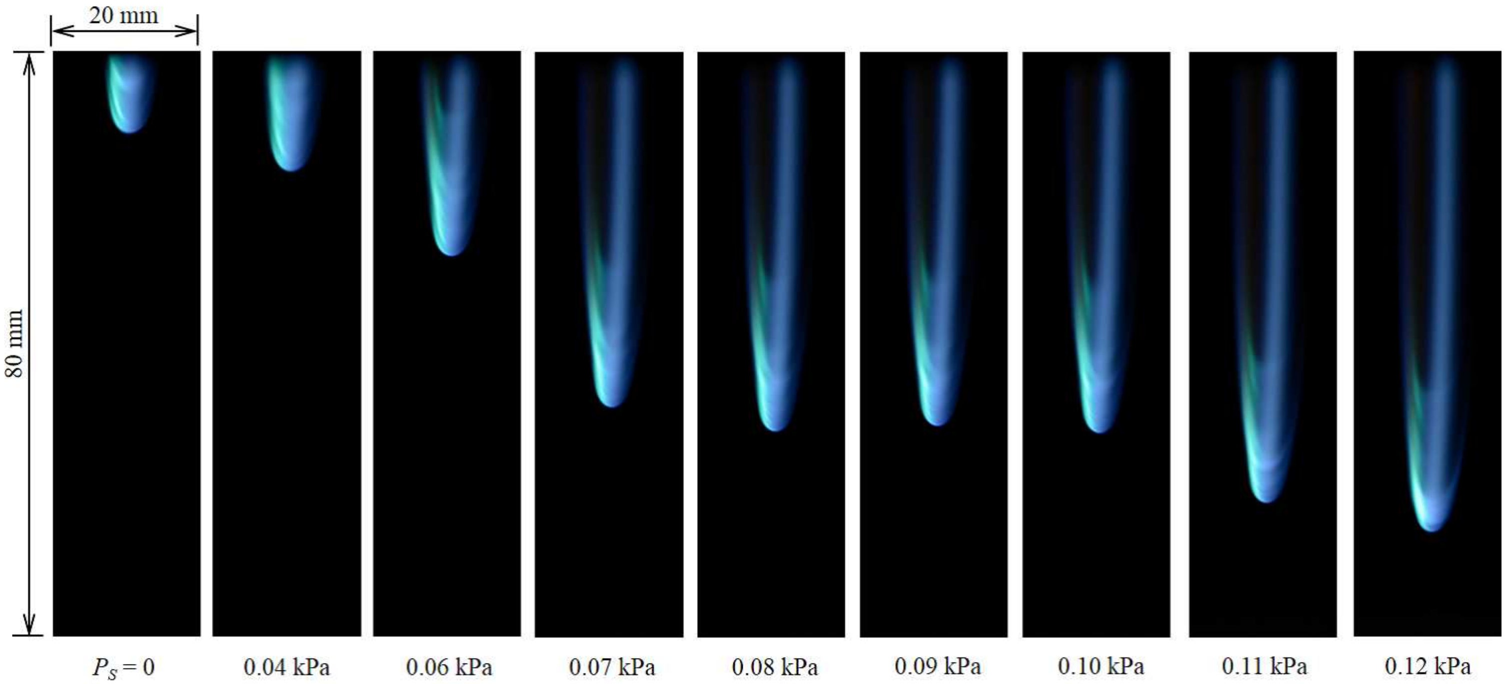

Figure 5-1-7 Direct images of the triple flame with various sound pressures (C_3H_8, ϕ =3.2)

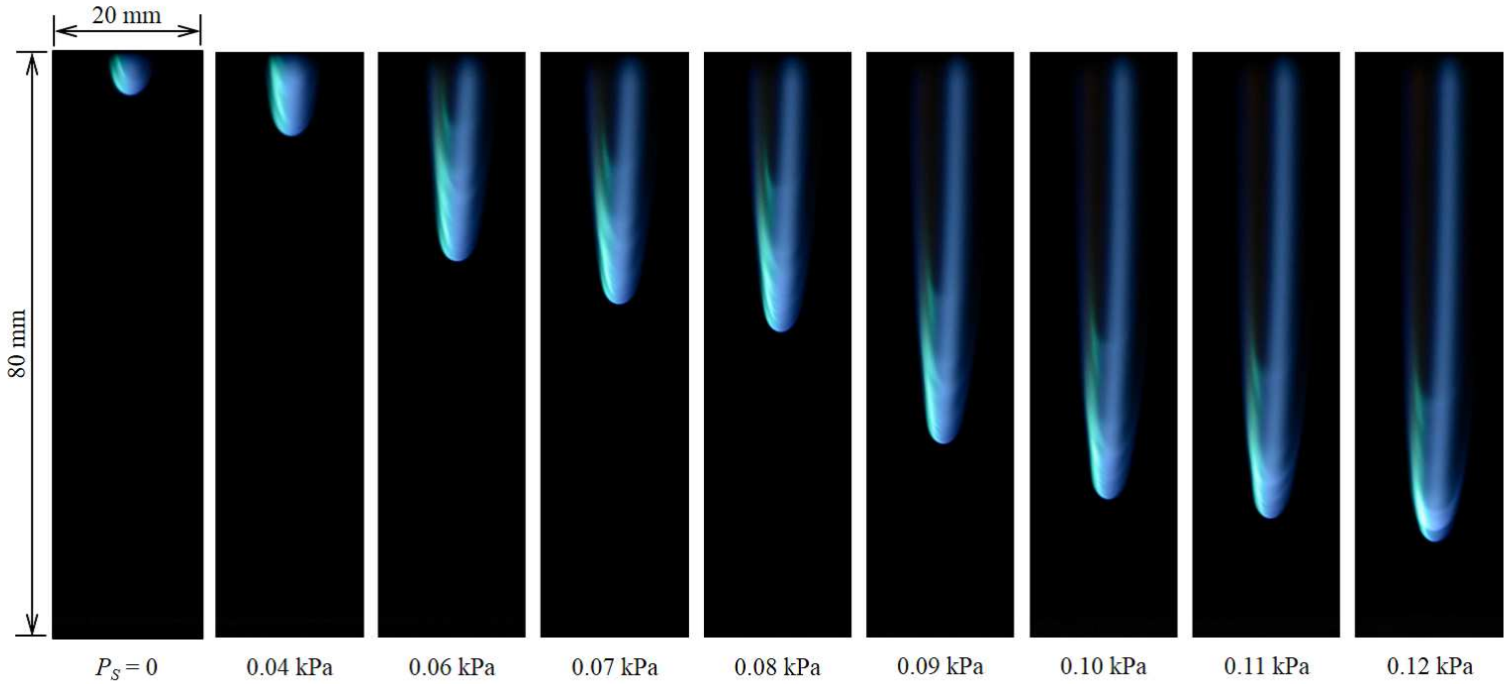

Figure 5-1-8 Direct images of the triple flame with various sound pressures (C_3H_8, ϕ =3.4)

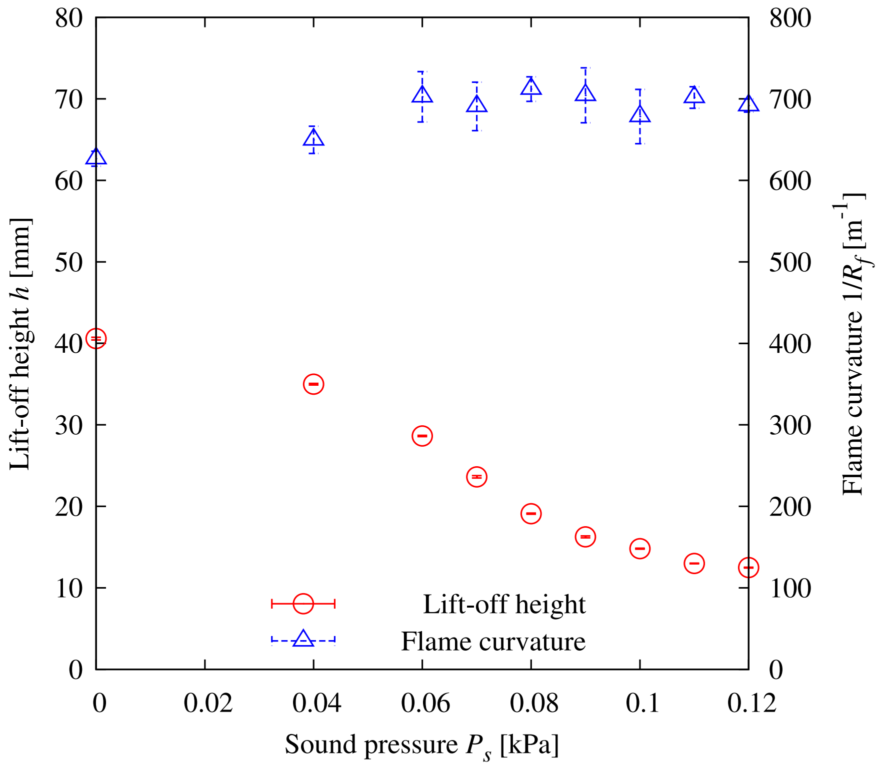

Figure 5-1-9 Flame curvature and lift-off height with various sound pressures (CH_4, ϕ =2.8, error bar: average ± S. D.)

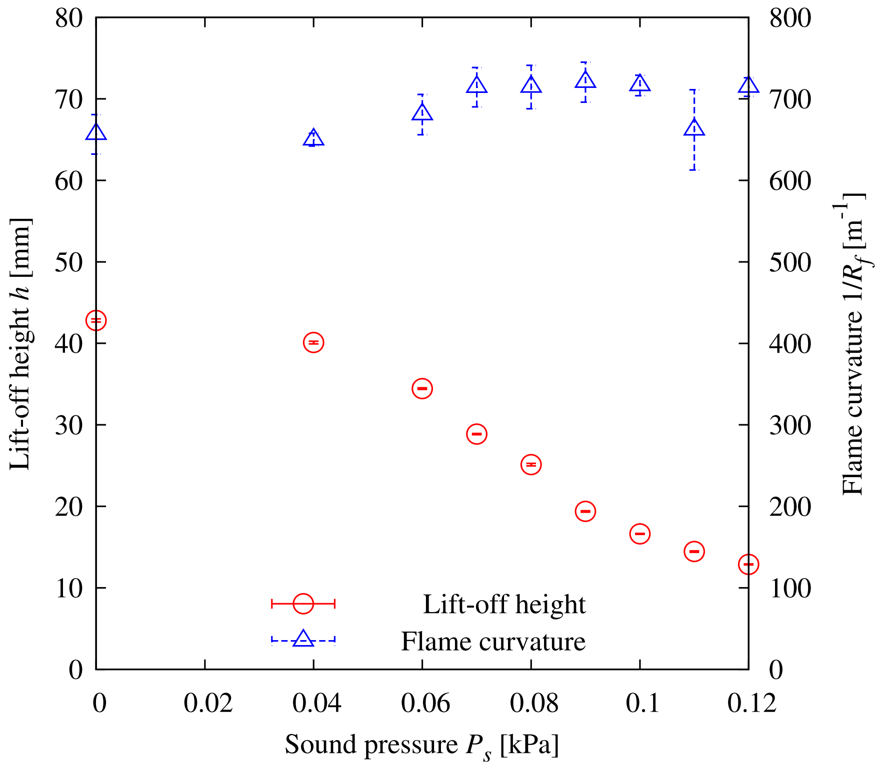

Figure 5-1-10 Flame curvature and lift-off height with various sound pressures (CH_4, ϕ =3.0, error bar: average ± S. D.)

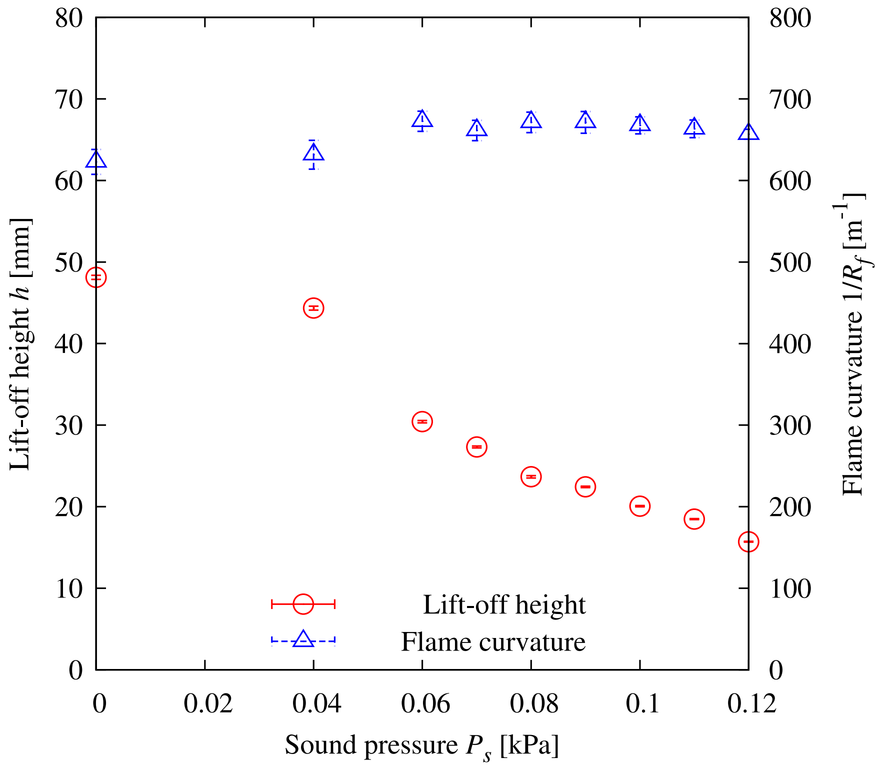

Figure 5-1-11 Flame curvature and lift-off height with various sound pressures (CH_4, ϕ =3.2, error bar: average ± S. D.)

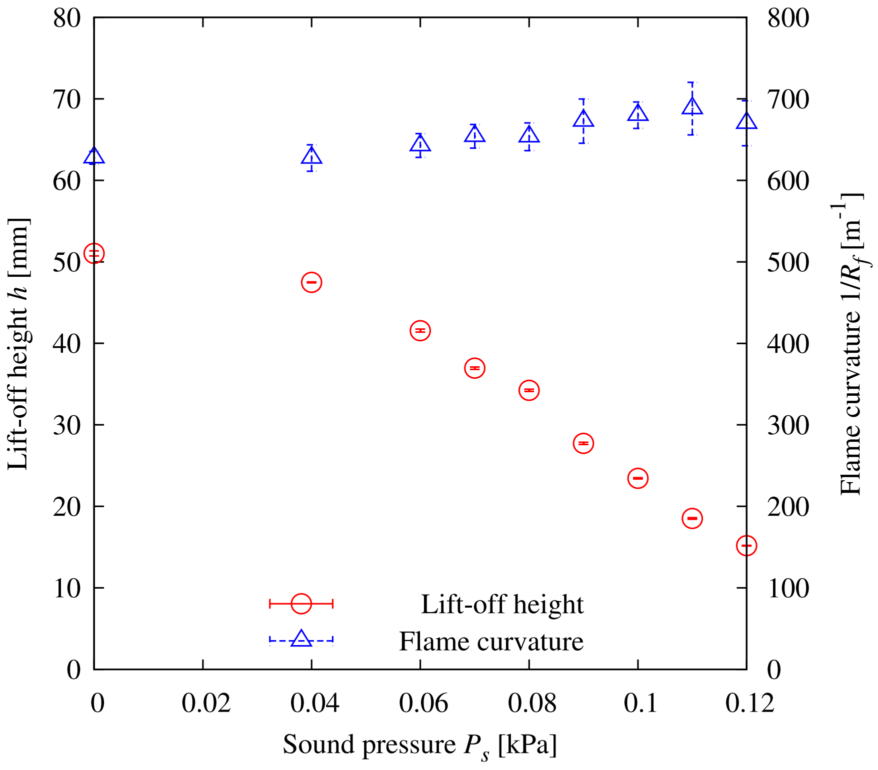

Figure 5-1-12 Flame curvature and lift-off height with various sound pressures (CH_4, ϕ =3.4, error bar: average ± S. D.)

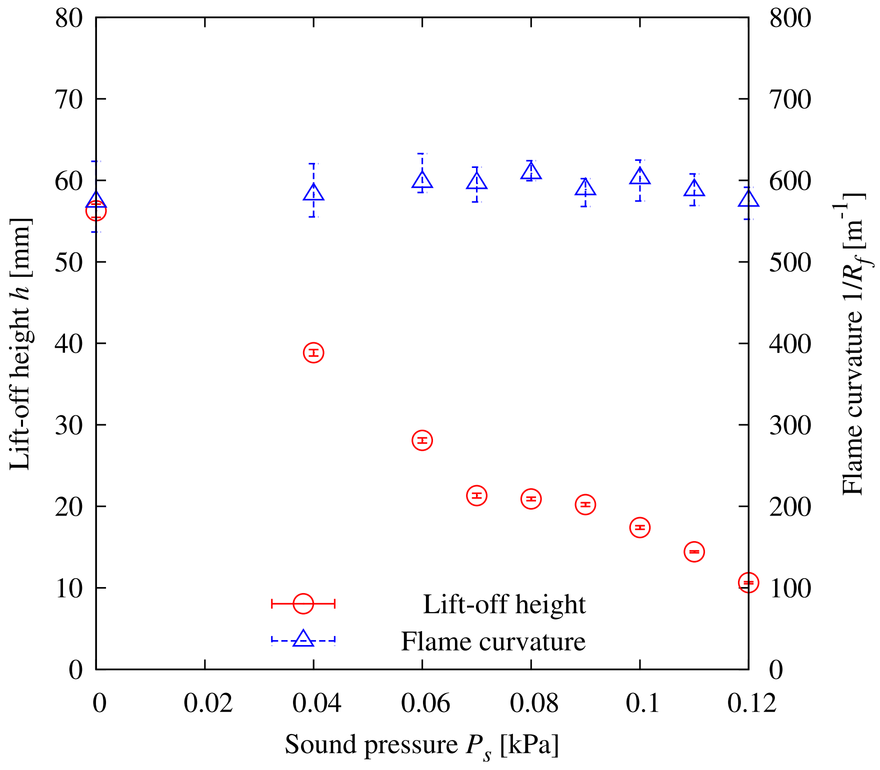

Figure 5-1-13 Flame curvature and lift-off height with various sound pressures (C_3H_8, ϕ =2.8, error bar: average ± S. D.)

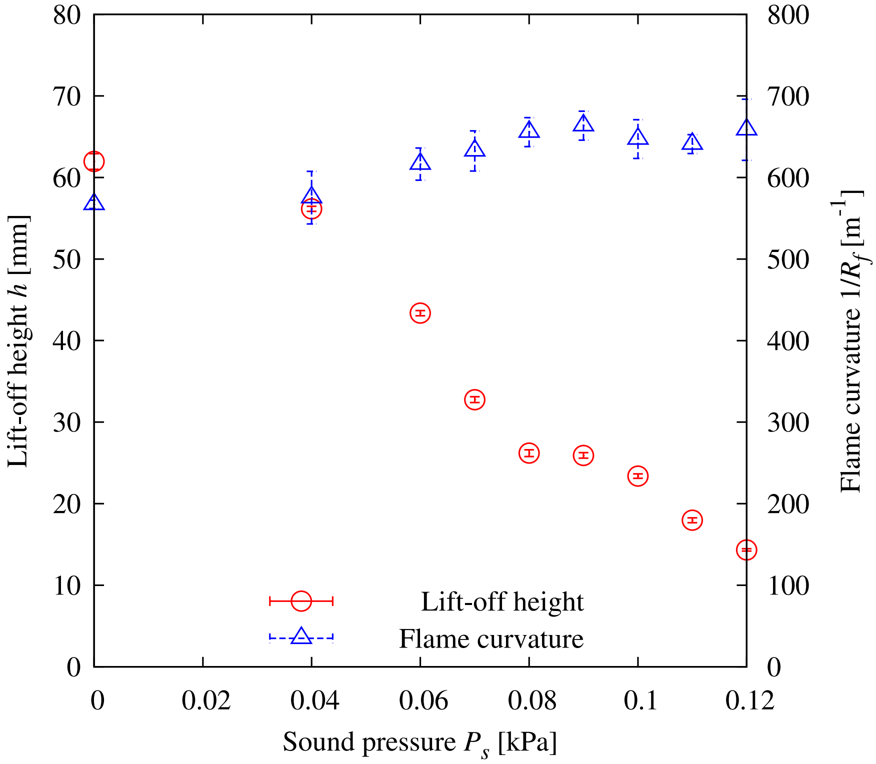

Figure 5-1-14 Flame curvature and lift-off height with various sound pressures (C_3H_8, ϕ =3.0, error bar: average ± S. D.)

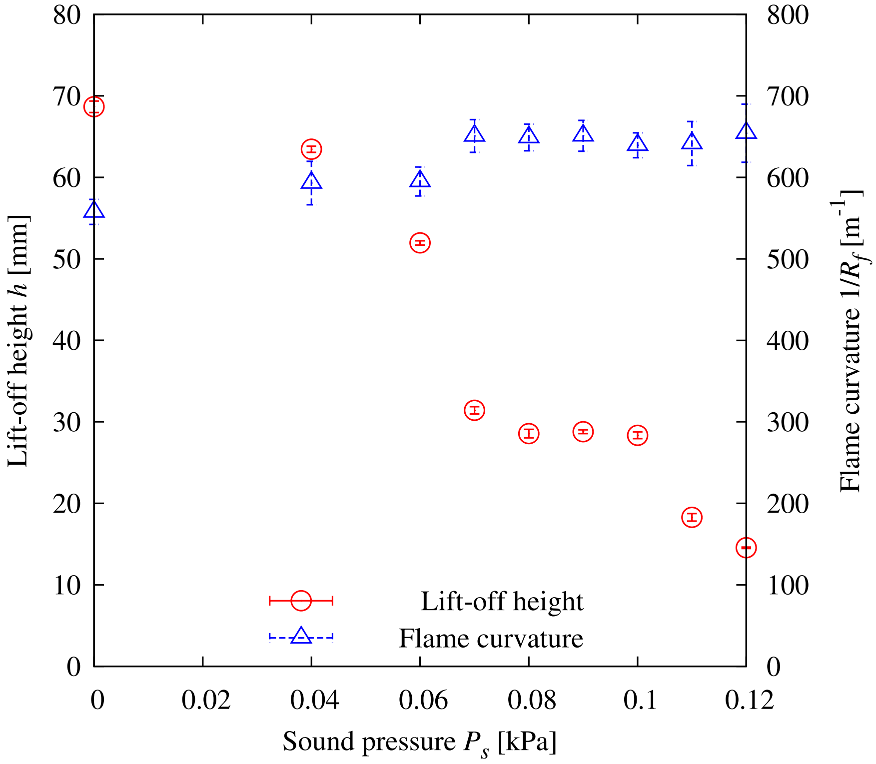

Figure 5-1-15 Flame curvature and lift-off height with various sound pressures (C_3H_8, ϕ =3.2, error bar: average ± S. D.)

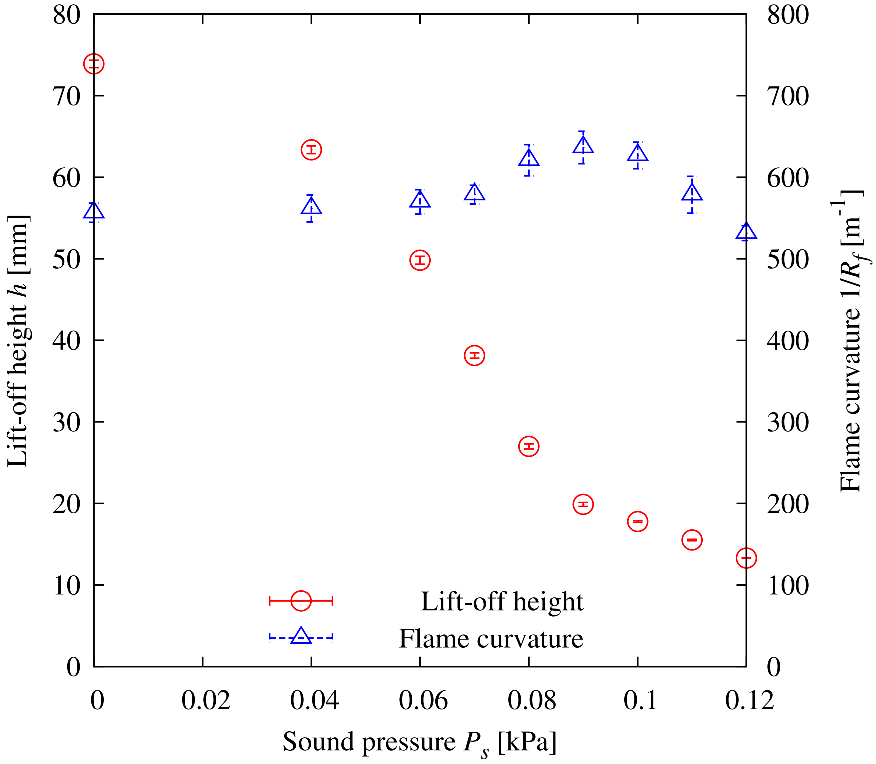

Figure 5-1-16 Flame curvature and lift-off height with various sound pressures (C_3H_8, ϕ =3.4, error bar: average ± S. D.)

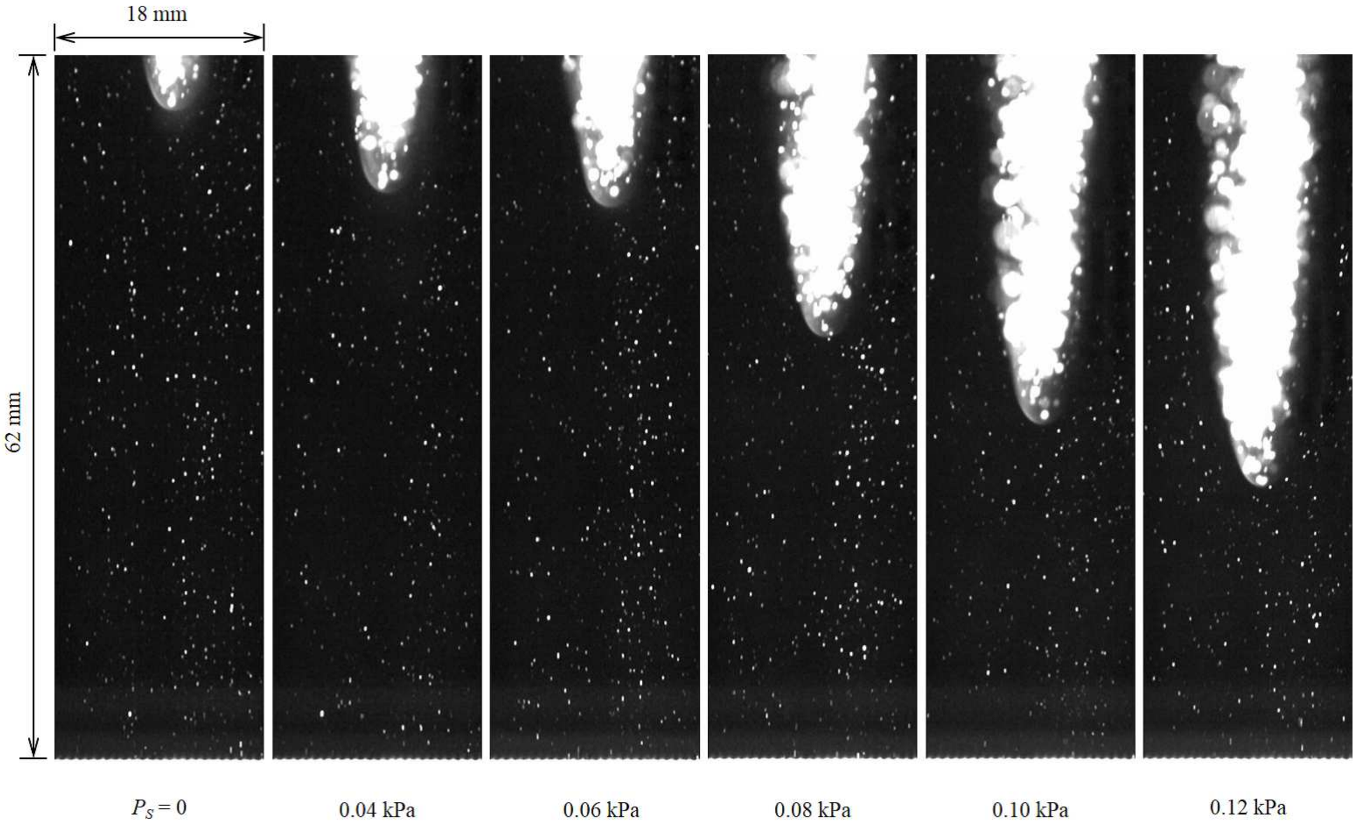

Figure 5-2-1 Raw images of PIV with various sound pressures

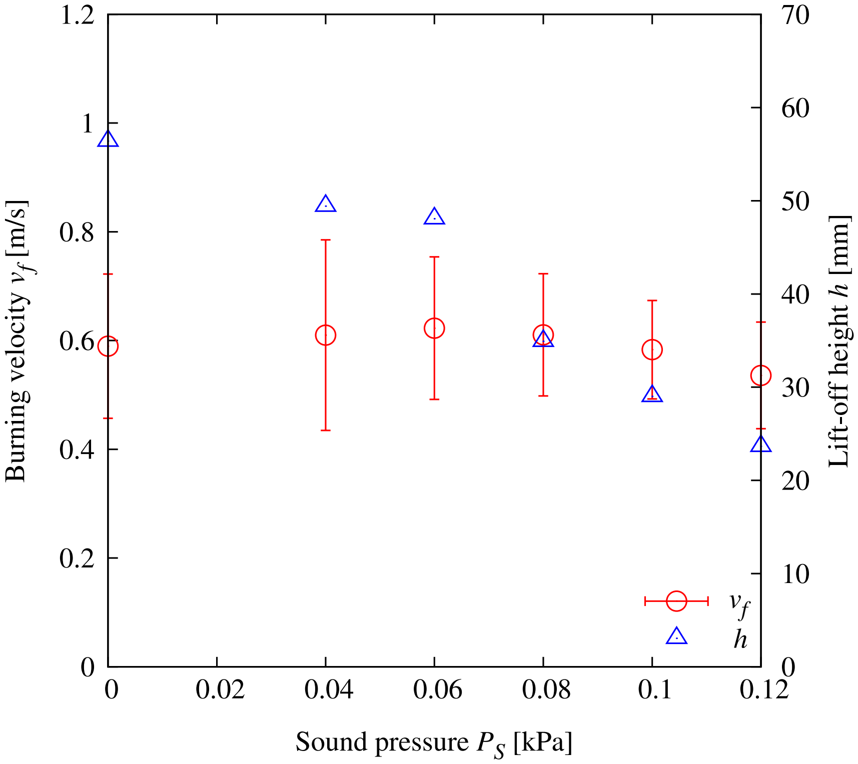

Figure 5-2-2 Burning velocity and lift-off height with various sound pressures (C_3H_8, ϕ =3.0, error bar: average ± S. D.)

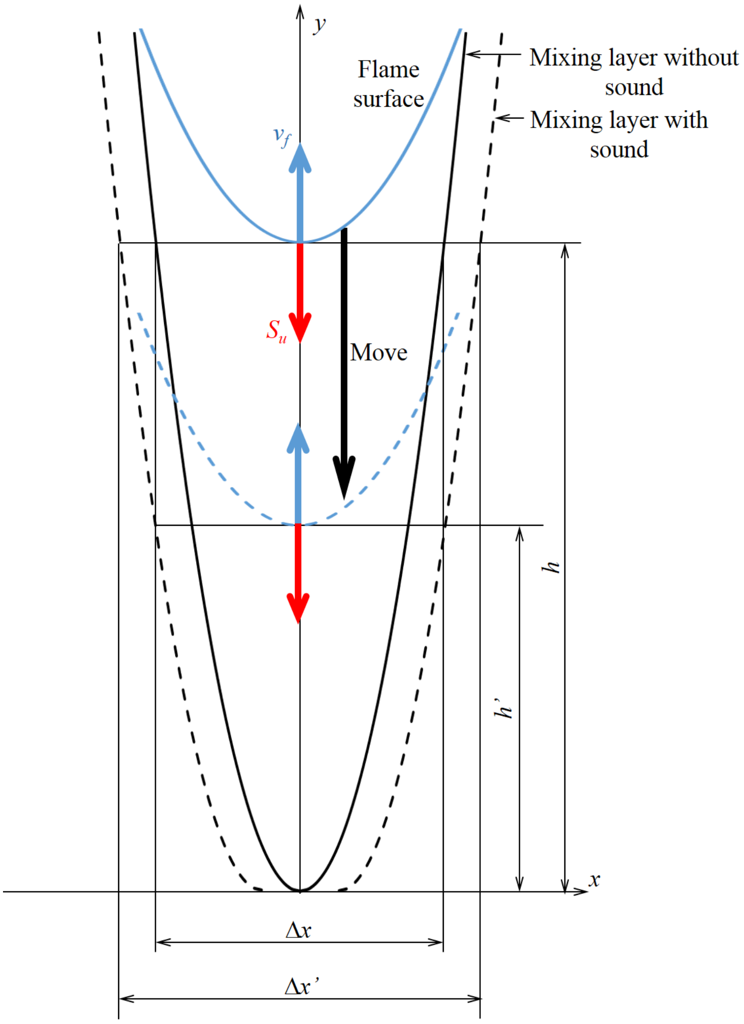

Figure 5-3-1 Lift-off height reduction mechanism

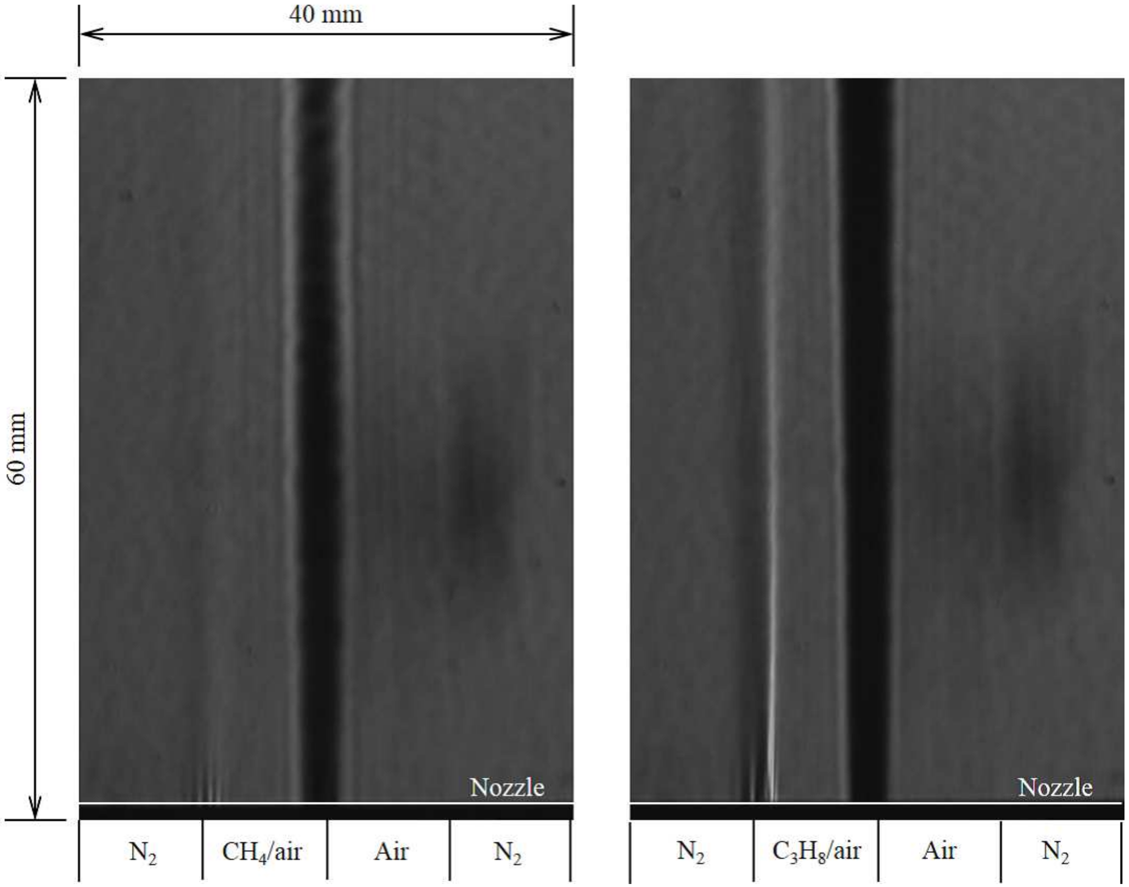

Figure 6-1-1 Schlieren images of the mixing layer without sound

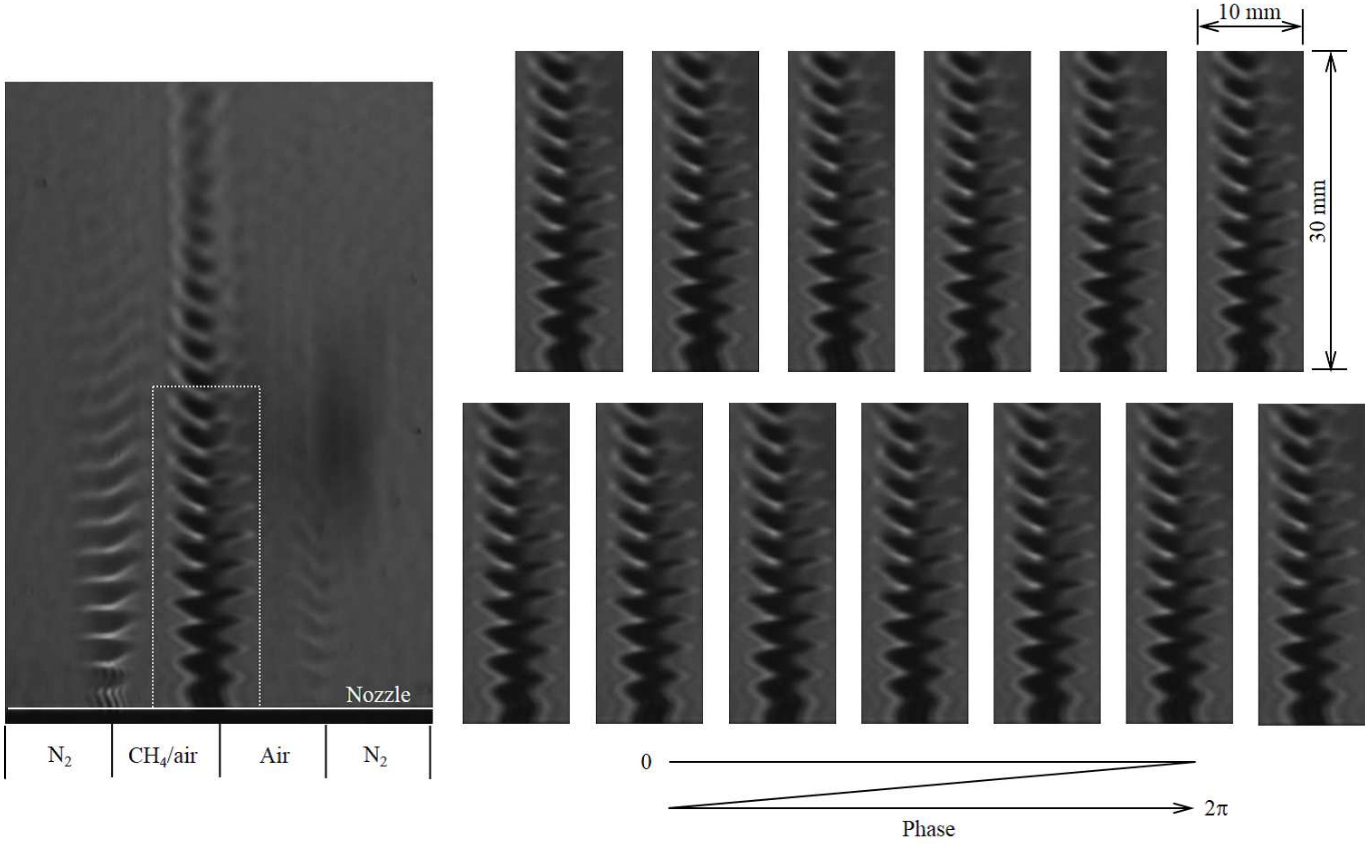

Figure 6-1-2 Schlieren images of the mixing layer with sound (CH_4, ϕ =3.0, P_S=0.08 kPa, Frame rate: 6,000 fps)

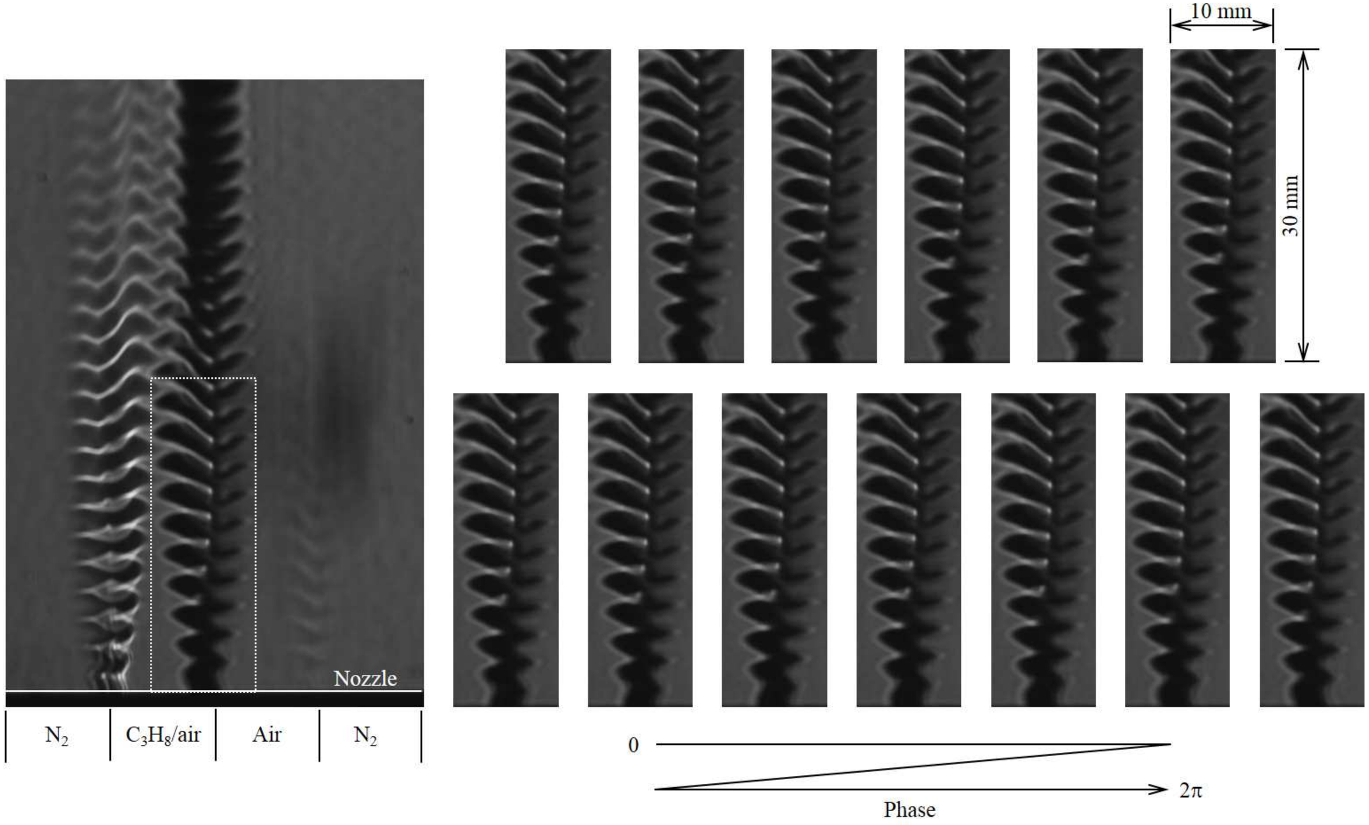

Figure 6-1-3 Schlieren images of the mixing layer with sound (C_3H_8, ϕ =3.0, P_S=0.08 kPa, Frame rate: 6,000 fps)

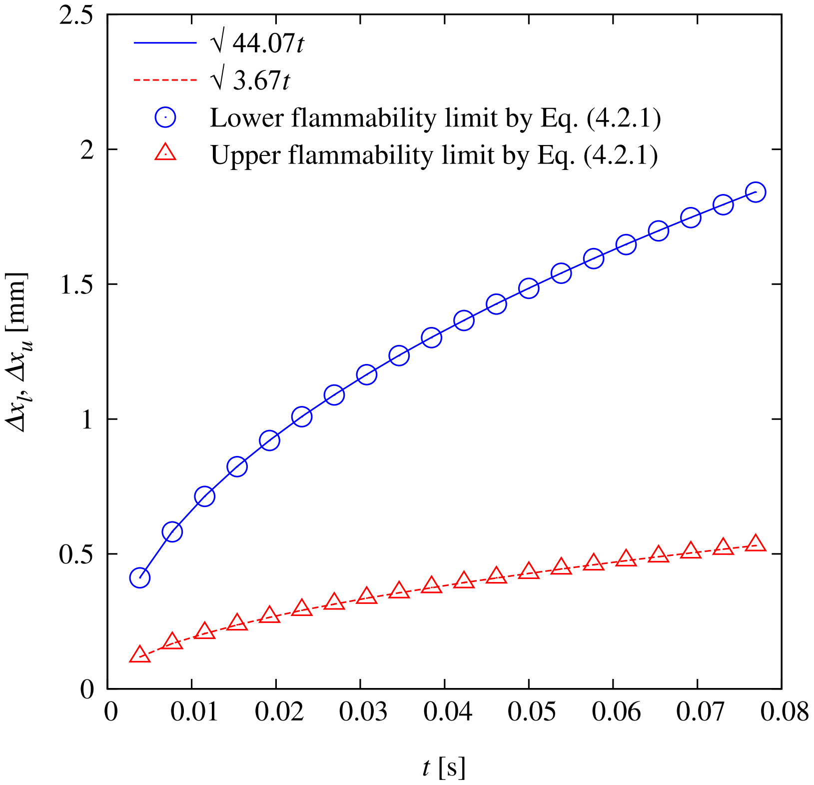

Figure 6-3-1 Calculated distribution of the mixing layer's width and its fitting curve (CH_4, ϕ =3.0)

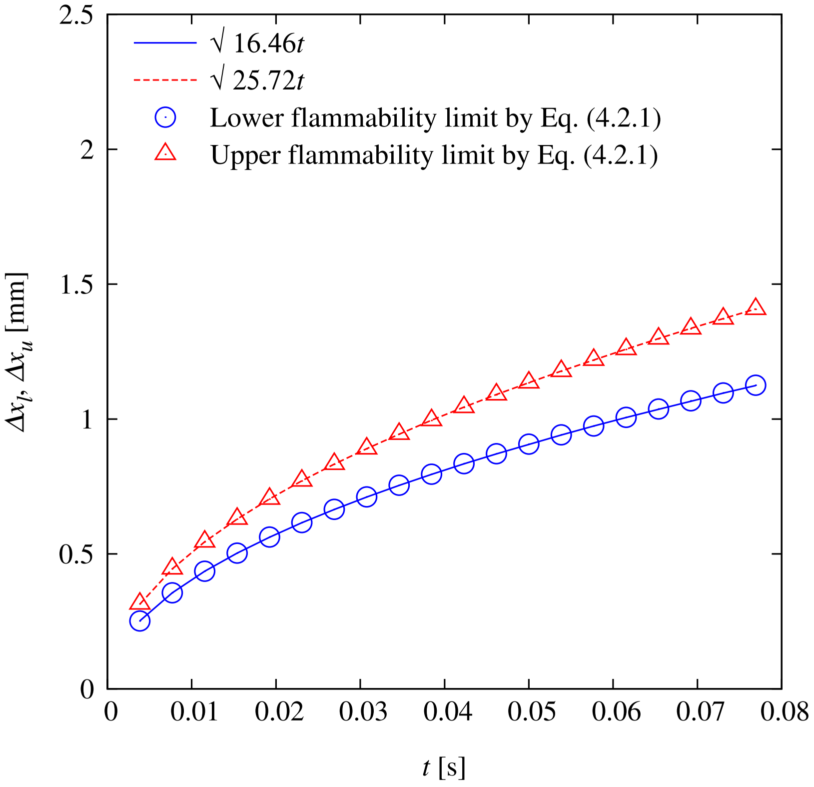

Figure 6-3-2 Calculated distribution of the mixing layer's width and its fitting curve (C_3H_8, ϕ =3.0)

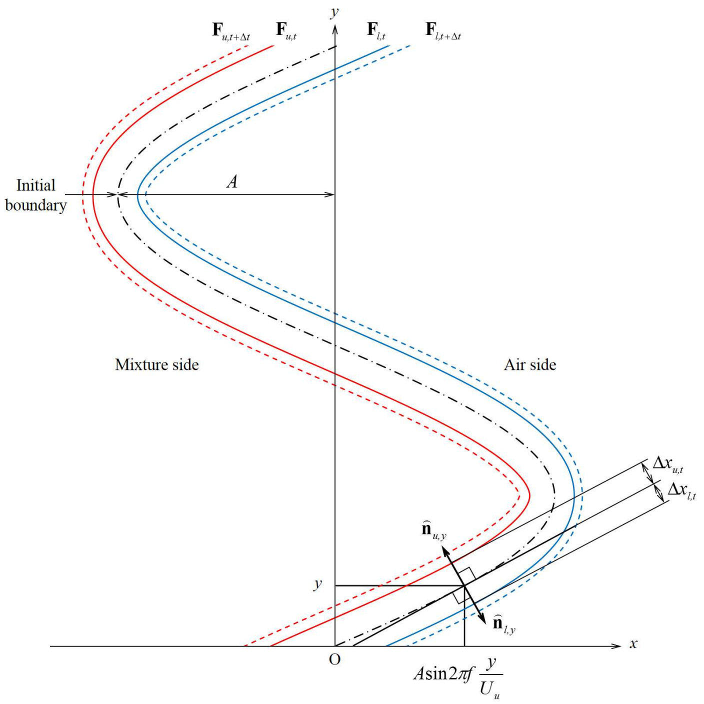

Figure 6-3-3 Schematic of meandering boundary shape and the diffusion model

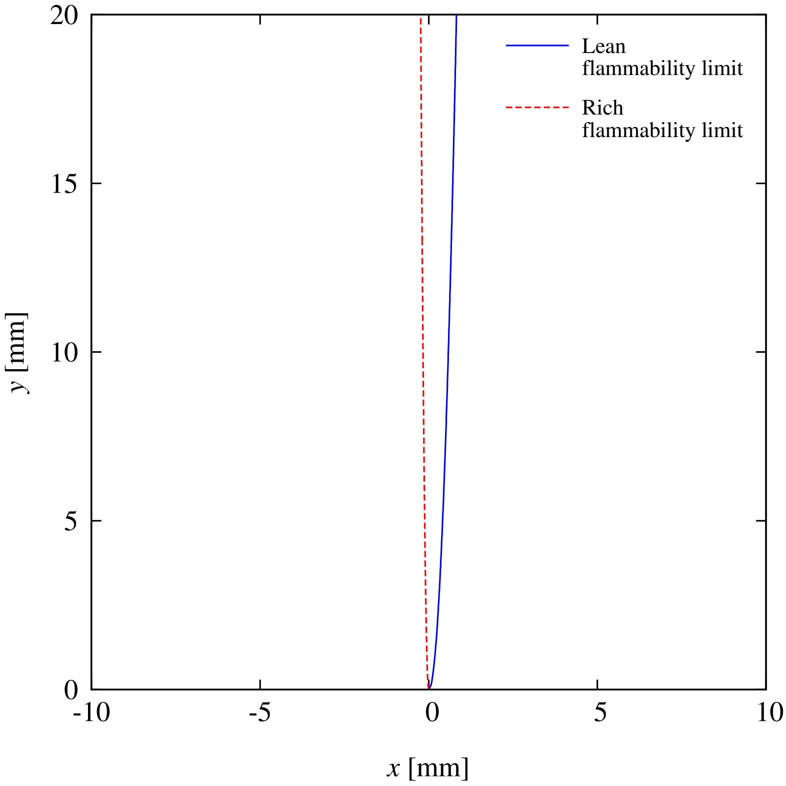

Figure 6-3-4 Calculated mixing layer's shape (CH_4, ϕ =3.0, A =0 mm)

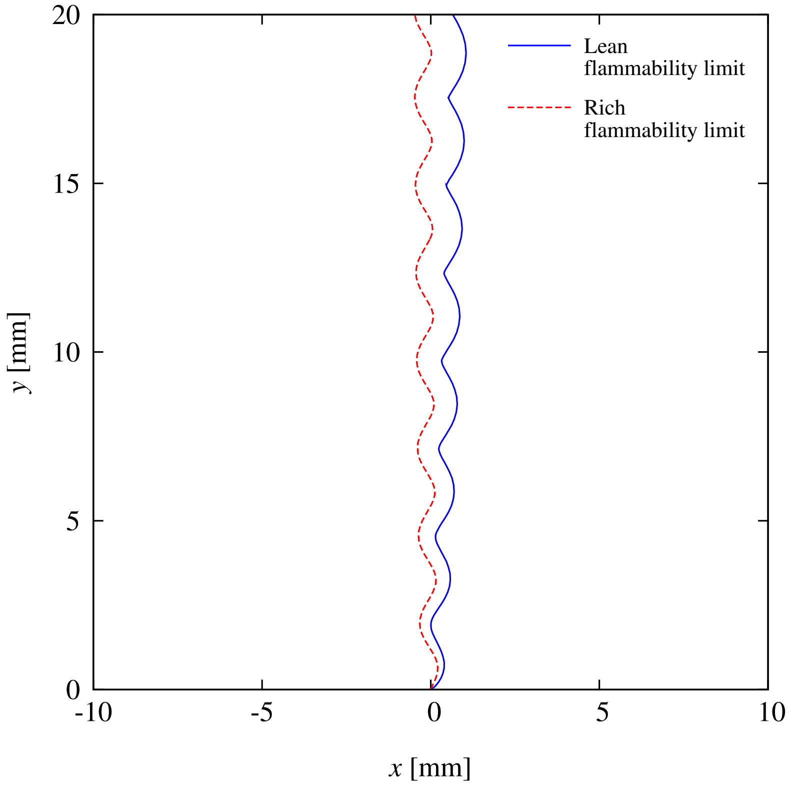

Figure 6-3-5 Calculated mixing layer’s shape (CH_4, ϕ =3.0, A =0.25 mm)

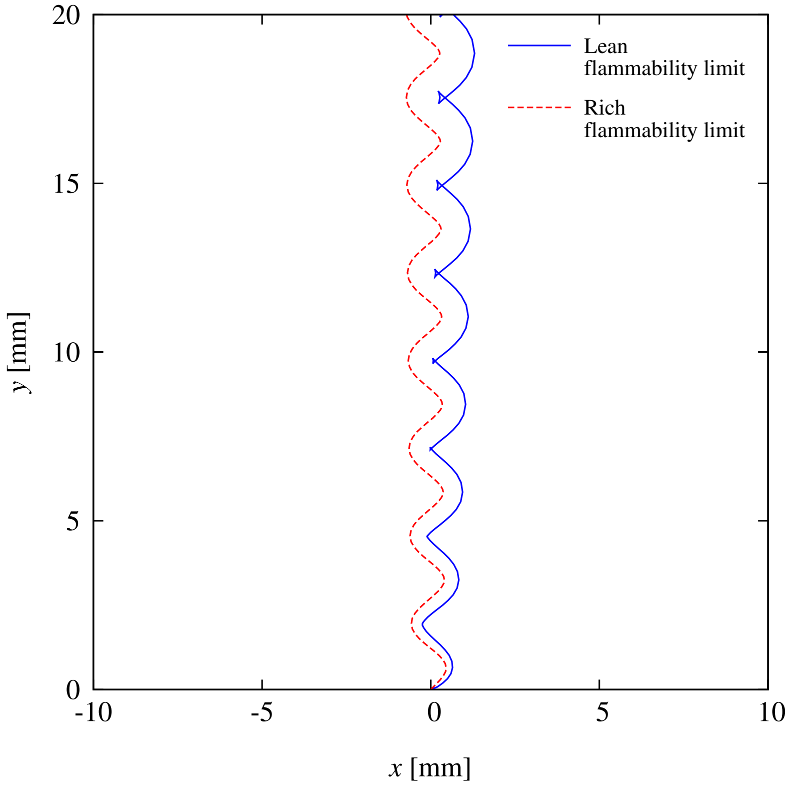

Figure 6-3-6 Calculated mixing layer's shape (CH_4, ϕ =3.0, A =0.50 mm)

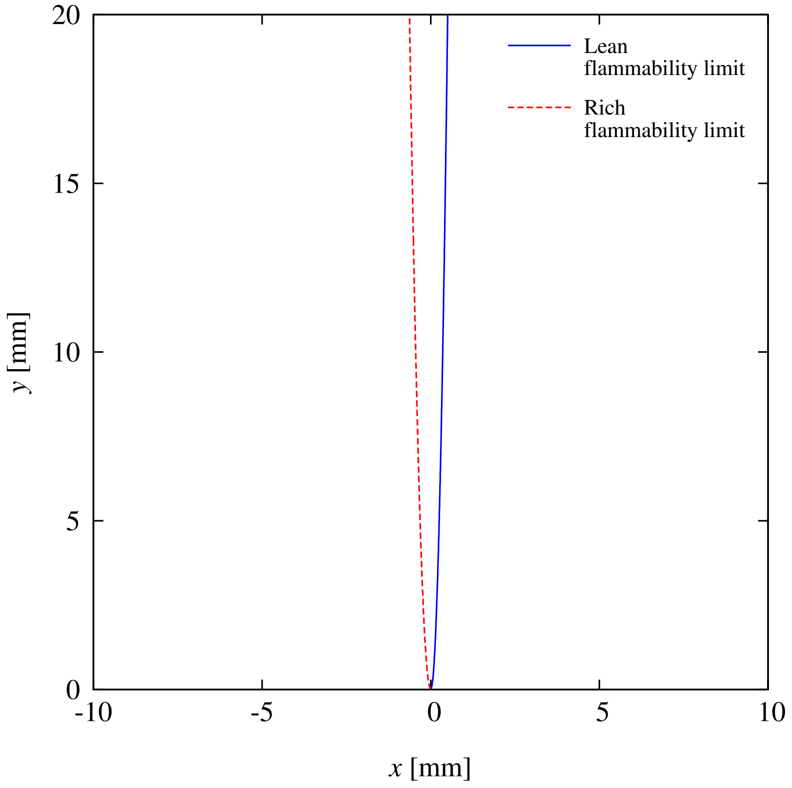

Figure 6-3-7 Calculated mixing layer's shape (C_3H_8, ϕ =3.0, A =0 mm)

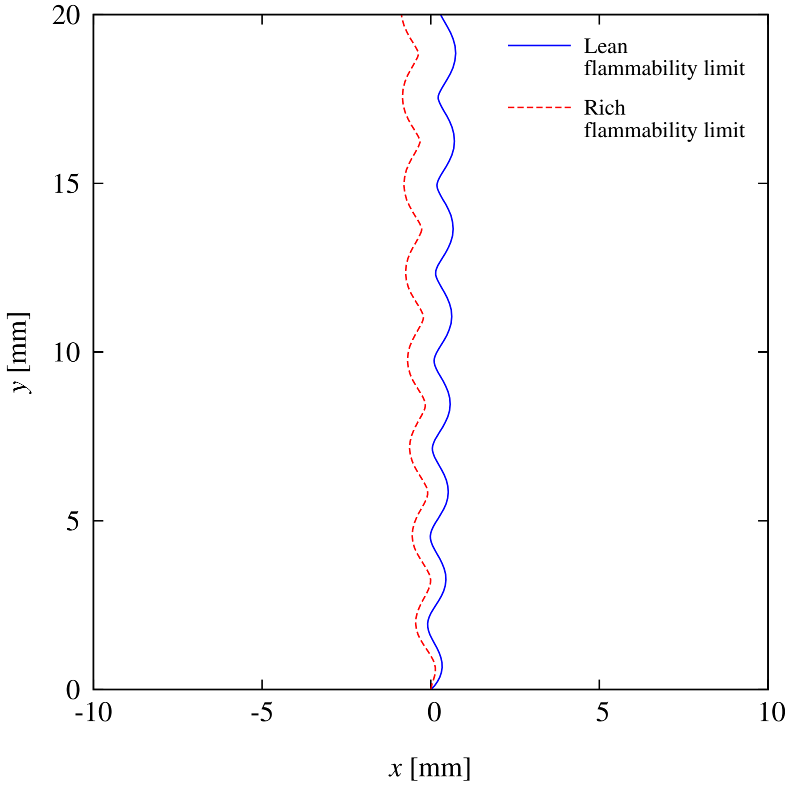

Figure 6-3-8 Calculated mixing layer's shape (C_3H_8, ϕ =3.0, A =0.25 mm)

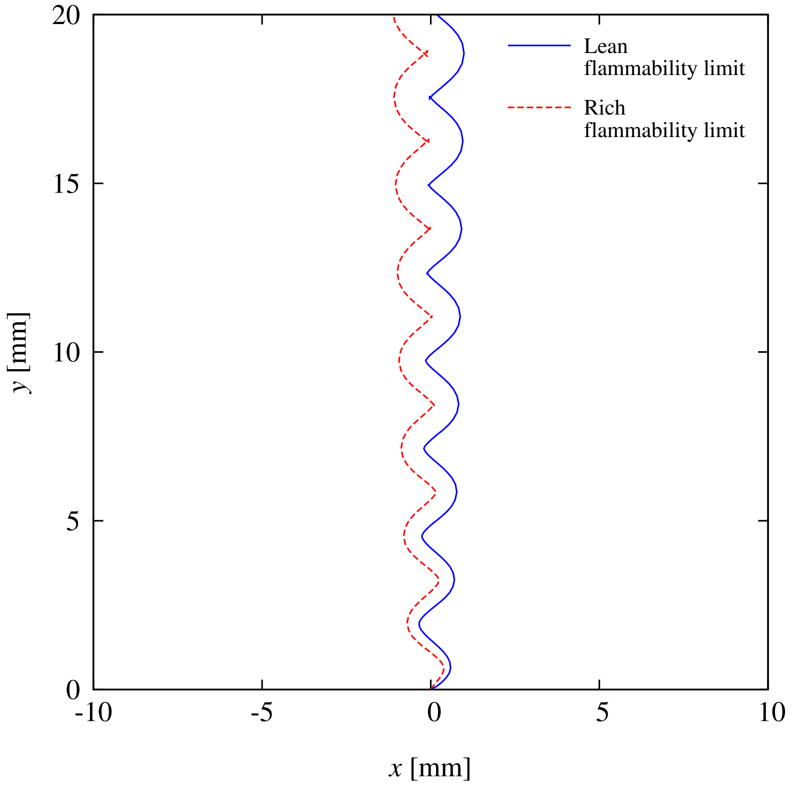

Figure 6-3-9 Calculated mixing layer's shape (C_3H_8, ϕ =3.0, A =0.50 mm)

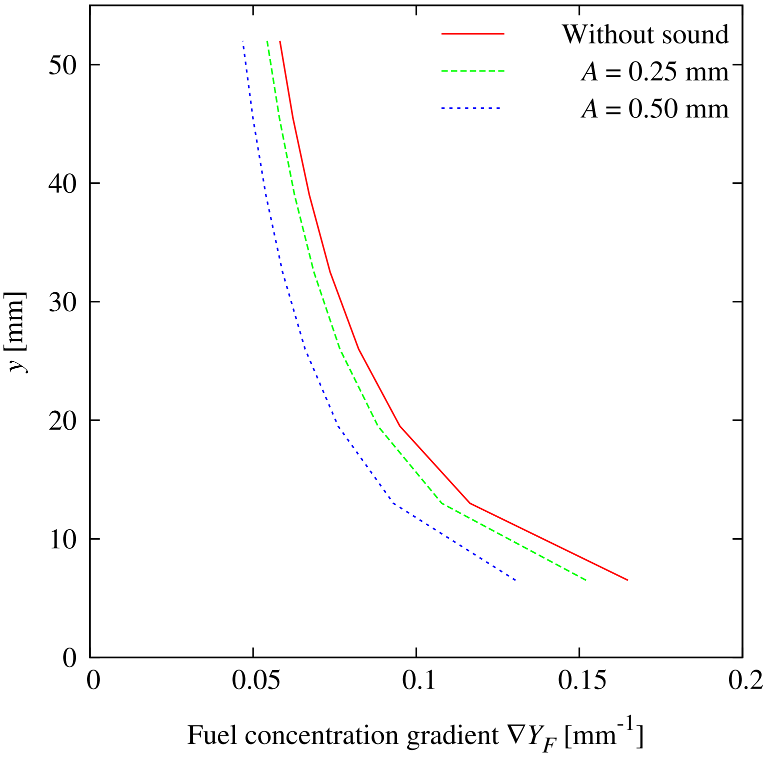

Figure 6-3-10 Calculated fuel concentration gradient by the model (C_3H_8, ϕ =3.0, λ=2.6 mm)

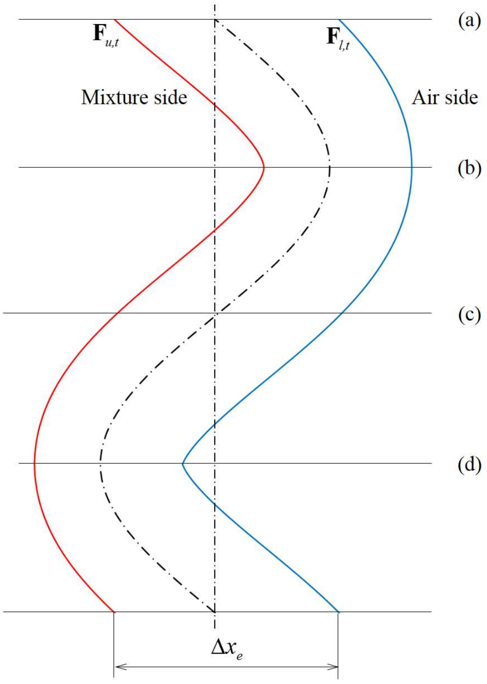

Figure 6-3-11 Definition of the effective width and data acquisition location

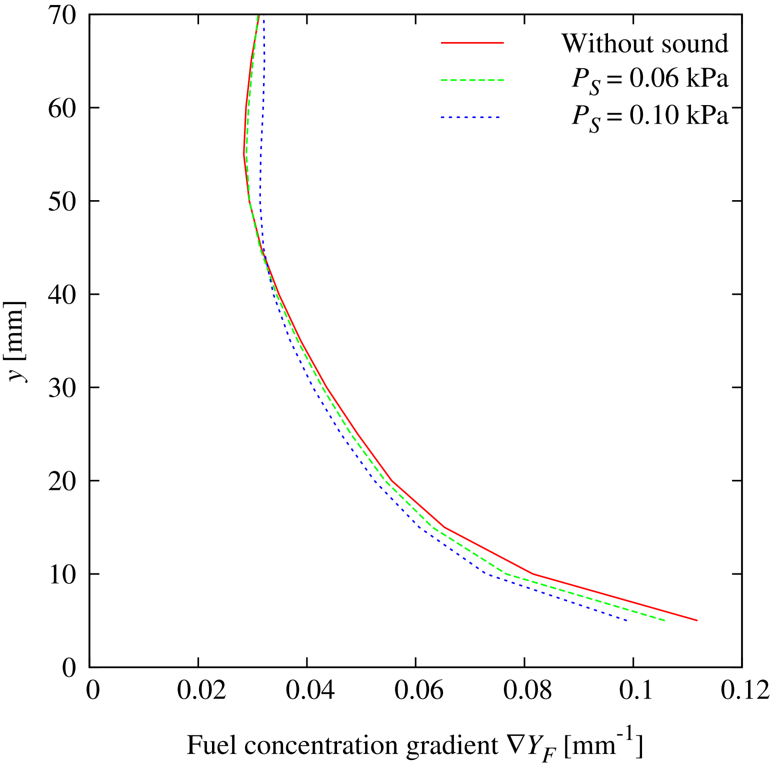

Figure 6-4-1 Calculated distribution of fuel concentration gradient with sound by the numerical simulation of case 1 (CH_4)

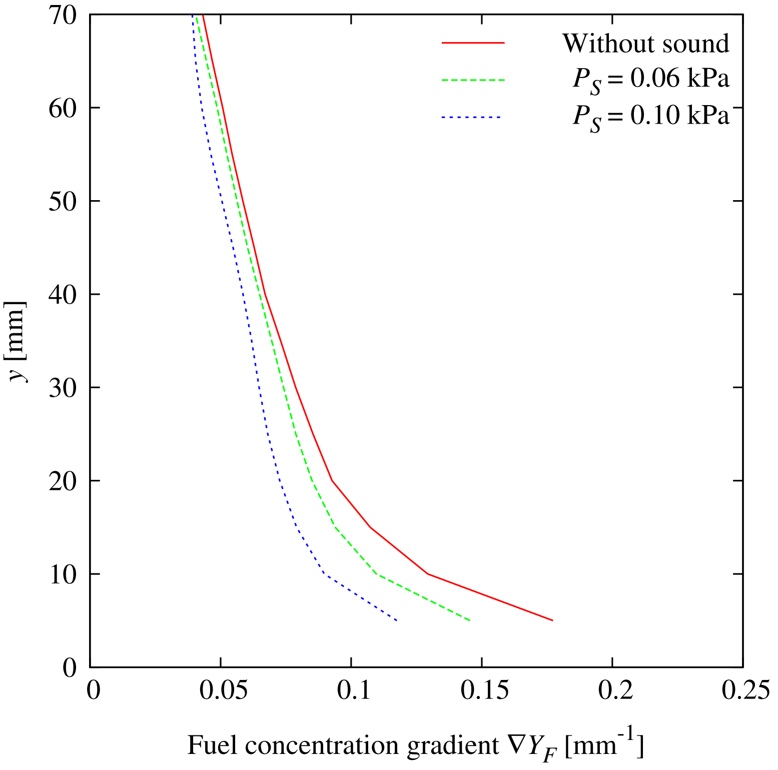

Figure 6-4-2 Calculated distribution of fuel concentration gradient with sound by the numerical simulation of case 1 (C_3H_8)

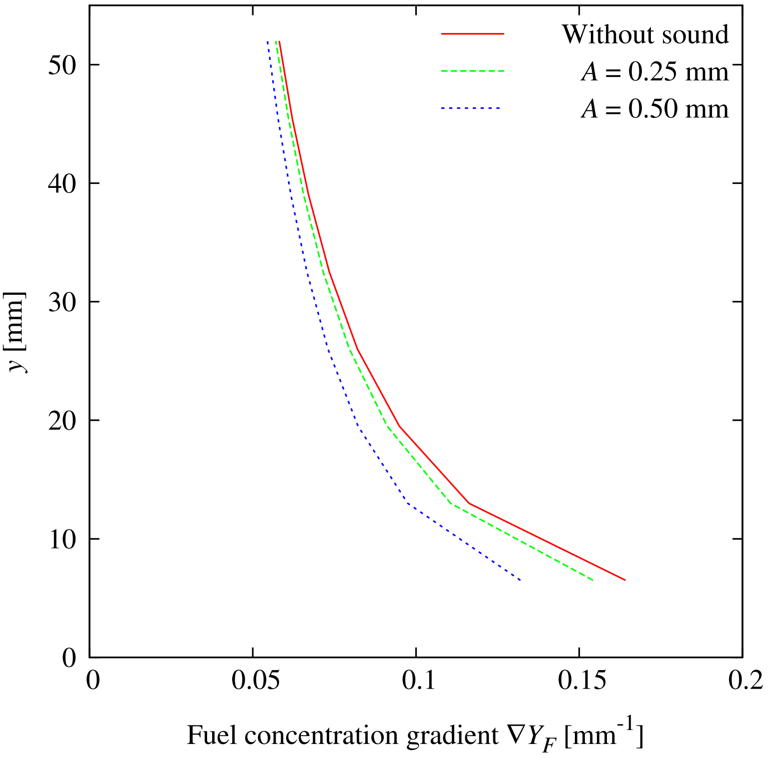

Figure 6-4-3 Calculated distribution of fuel concentration gradient by the numerical simulation of case 2 (C_3H_8, ϕ =3.0, λ=2.6 mm)

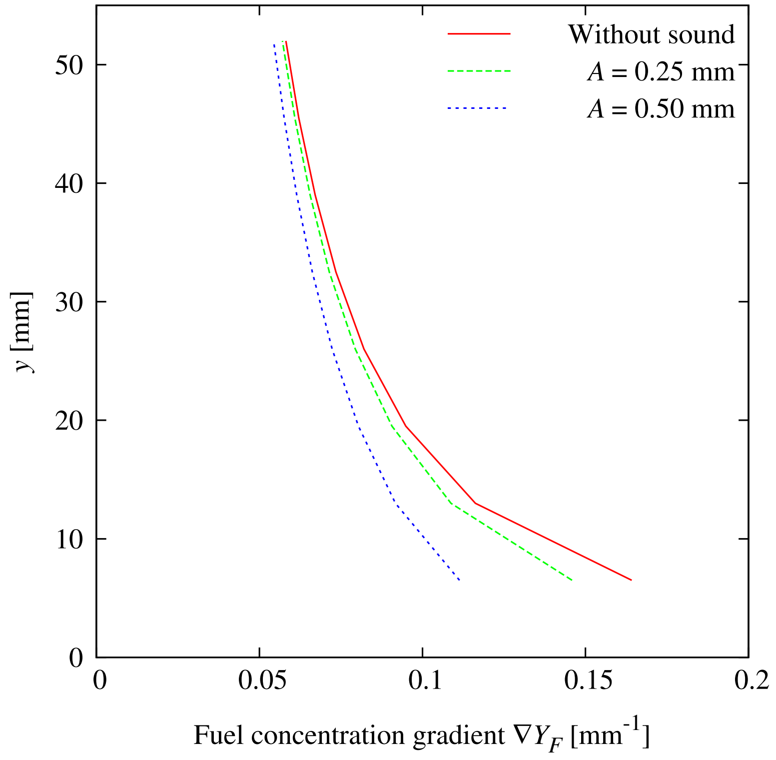

Figure 6-4-4 Calculated distribution of fuel concentration gradient by the numerical simulation of case 2 (C_3H_8, ϕ =3.0, λ=1.3 mm)

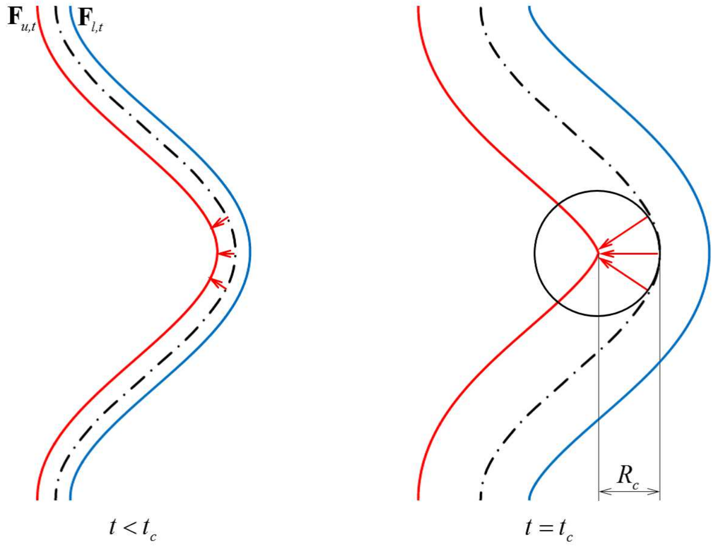

Figure 6-5-1 Diffusion until cusp formation

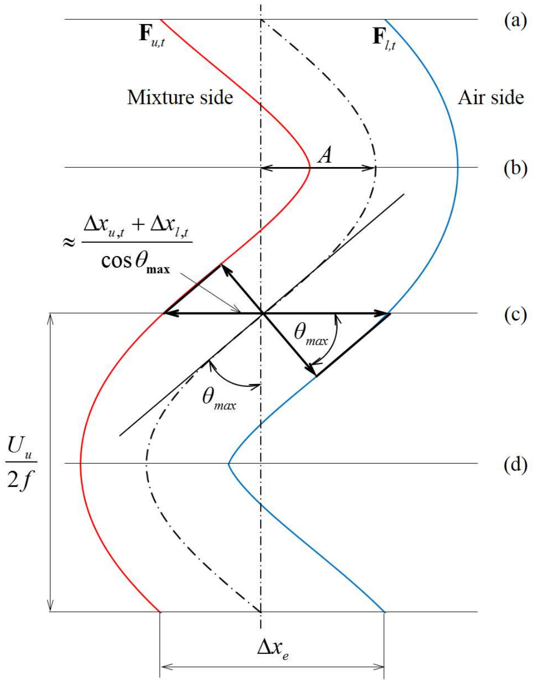

Figure 6-5-2 Schematic of boundary shape in the case of $K > 4\pi^2 St$

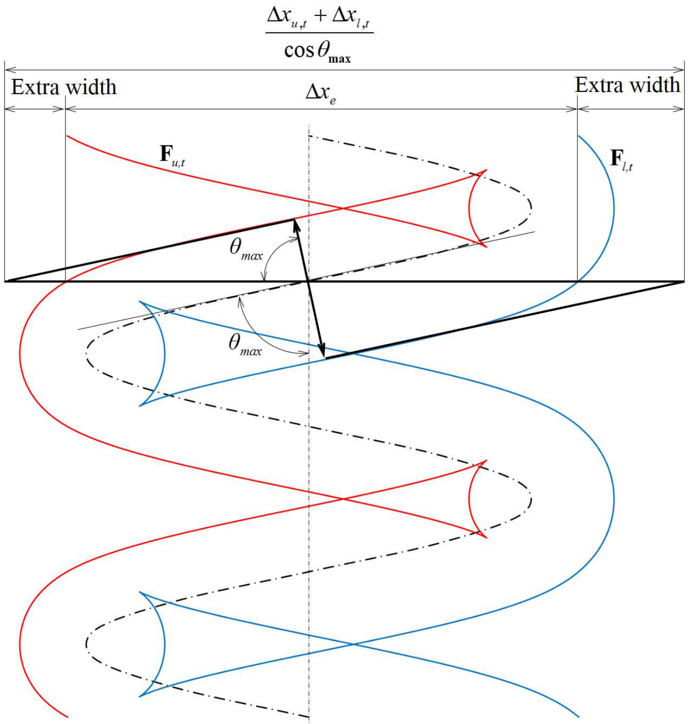

Figure 6-5-3 Schematic of boundary shape in the case of $K < 4\pi^2 St$

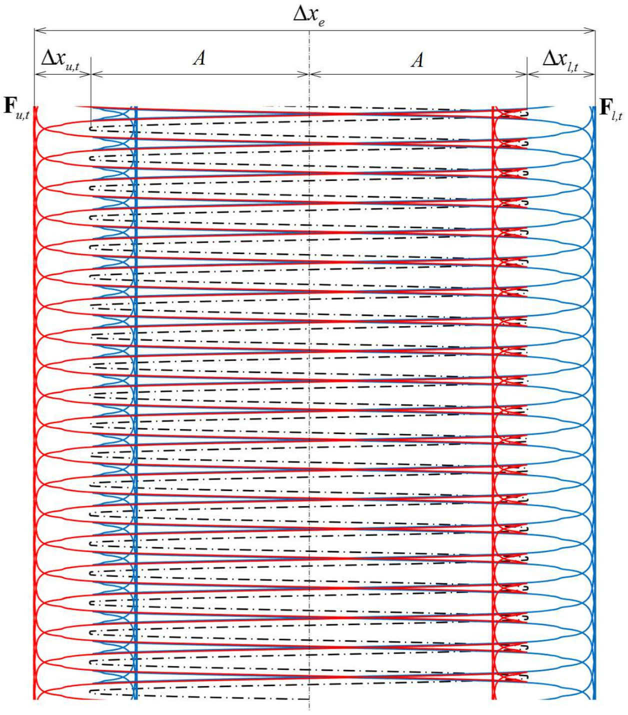

Figure 6-5-4 Schematic of boundary shape in the case of $K \ll 4\pi^2 St$

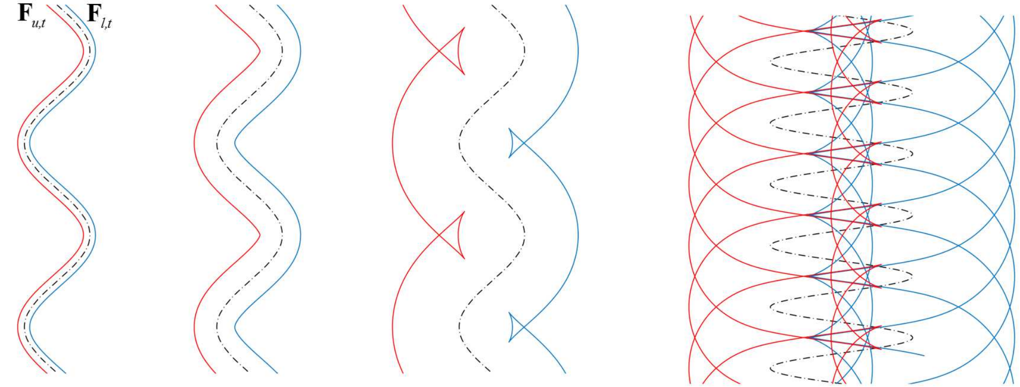

$K > 4\pi^2 St$ $K = 4\pi^2 St$ $K < 4\pi^2 St$ $K \ll 4\pi^2 St$

Figure 6-5-5 Schematic of boundary shapes with various relations between K and St

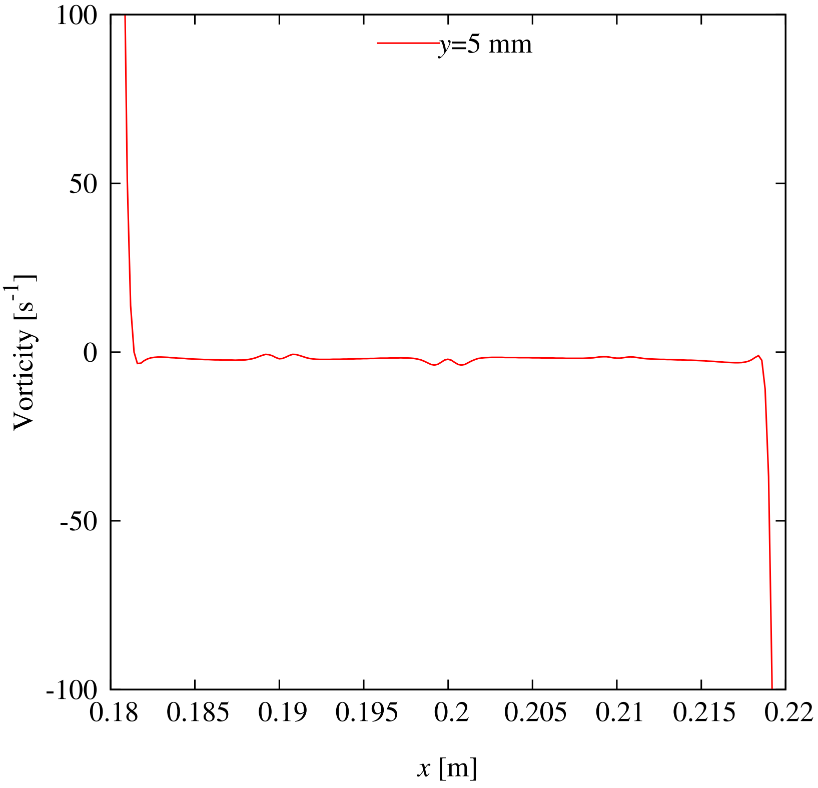

Figure 6-5-6 Vorticity around the mixing layer of methane (P_S=0.1 kPa,y =5 mm)

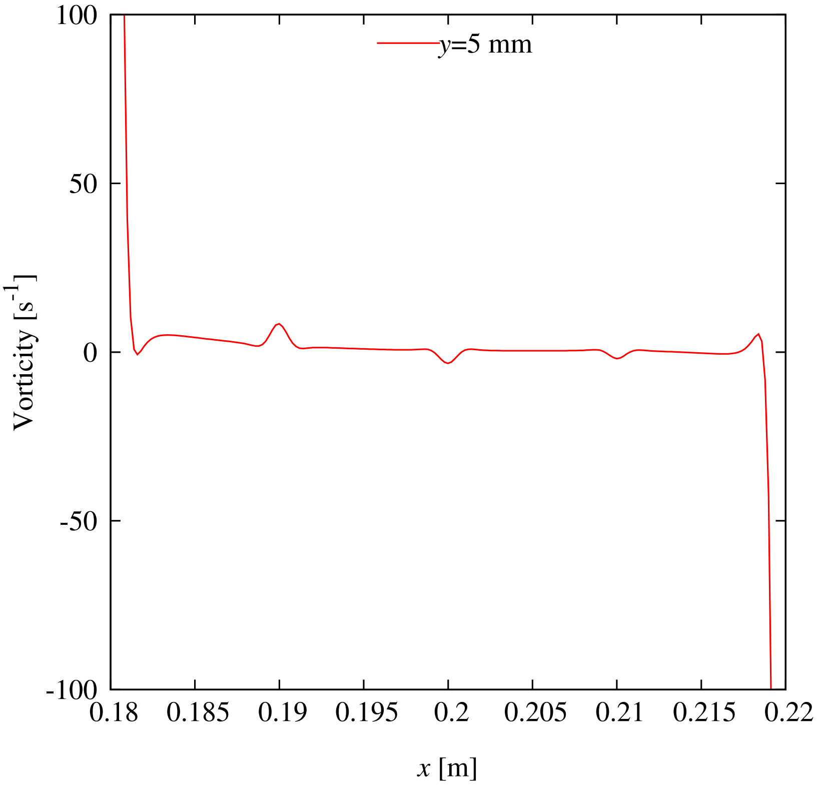

Figure 6-5-7 Vorticity around the mixing layer of propane (P_S=0.1 kPa,y =5 mm)

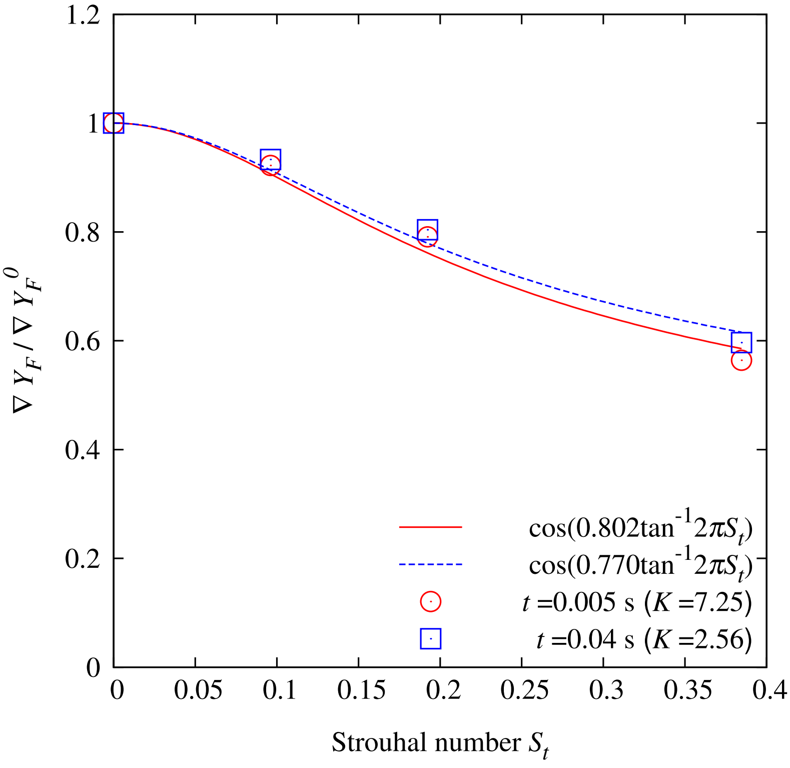

Figure 6-5-8 Normalized fuel concentration gradient obtained by the model (λ=2.6 mm, K=2.56, 7.25)

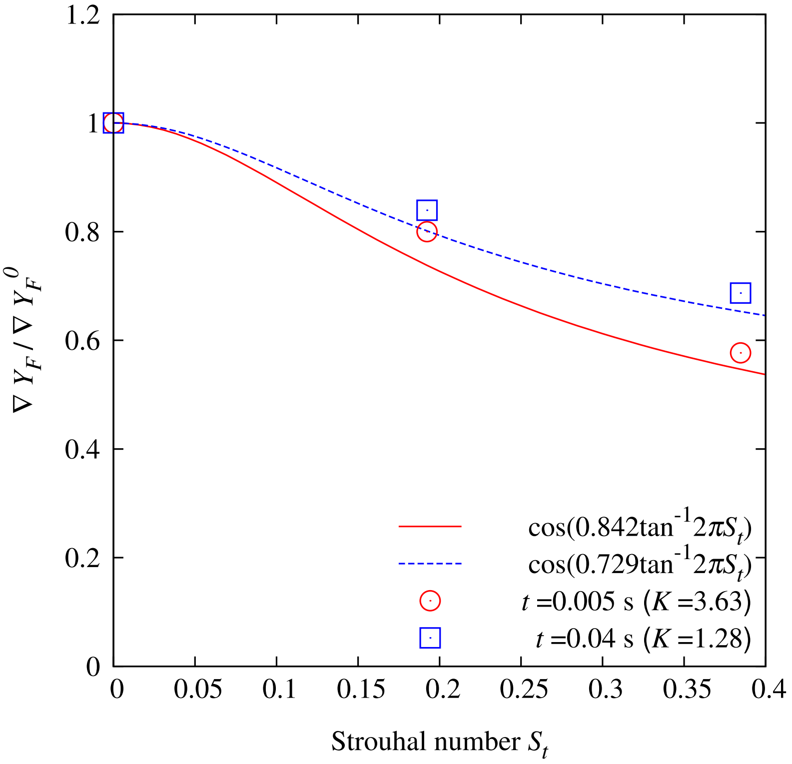

Figure 6-5-9 Normalized fuel concentration gradient obtained by the model (λ=1.3 mm, K=1.28, 3.63)

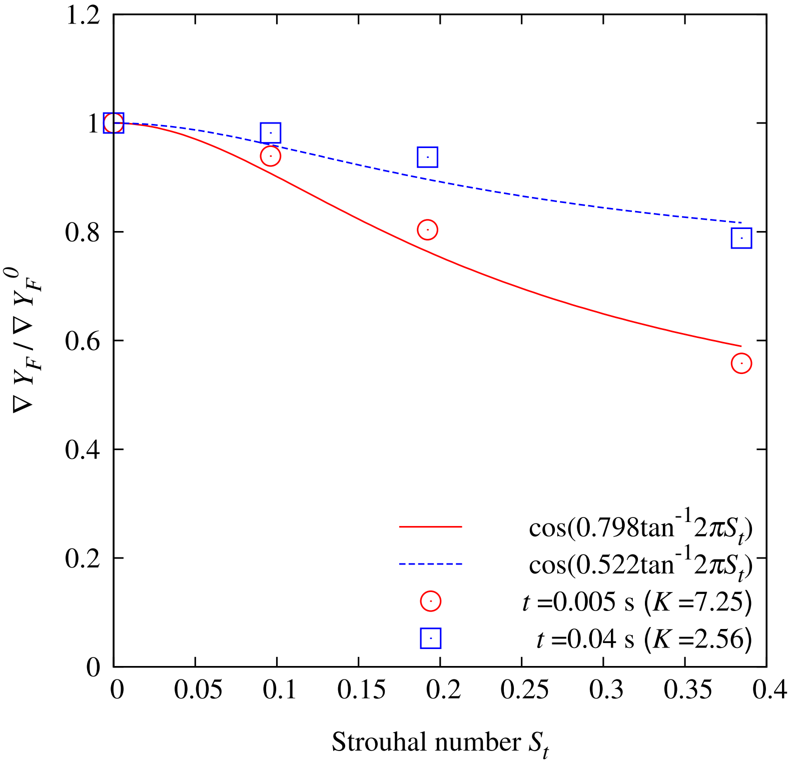

Figure 6-5-10 Normalized fuel concentration gradient obtained by numerical simulation (λ=2.6 mm, K=2.56, 7.25)

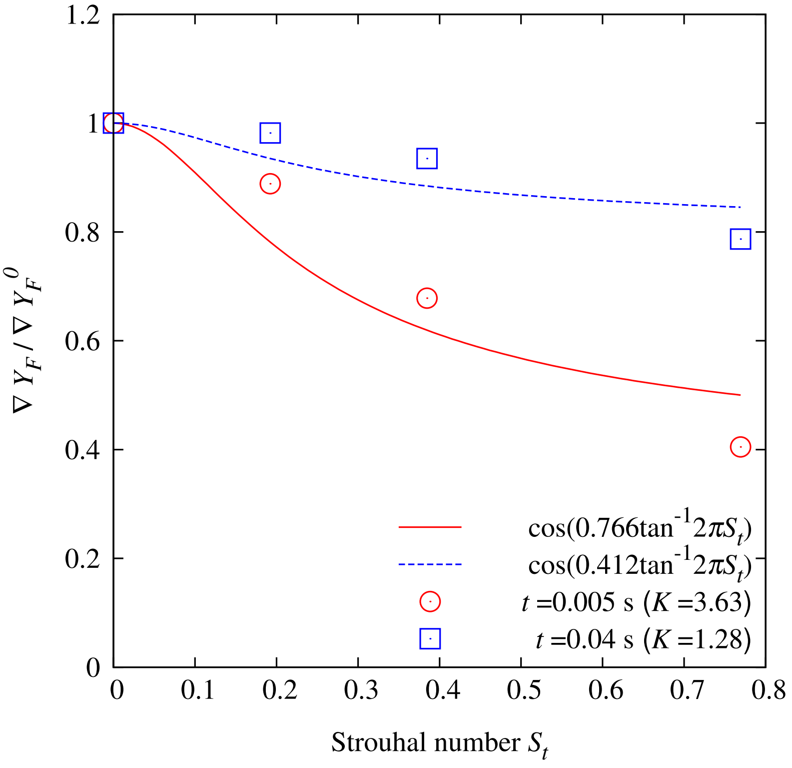

Figure 6-5-11 Normalized fuel concentration gradient obtained by numerical simulation (λ=1.3 mm, K=1.28, 3.63)

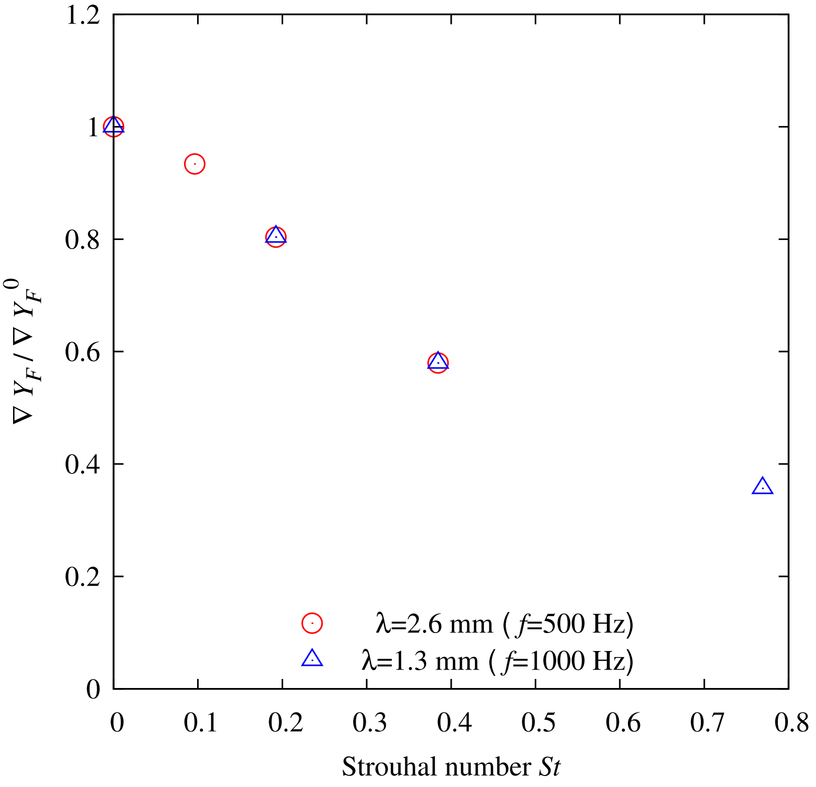

Figure 6-5-12 Normalized fuel concentration gradient obtained by the model (K=3.63)

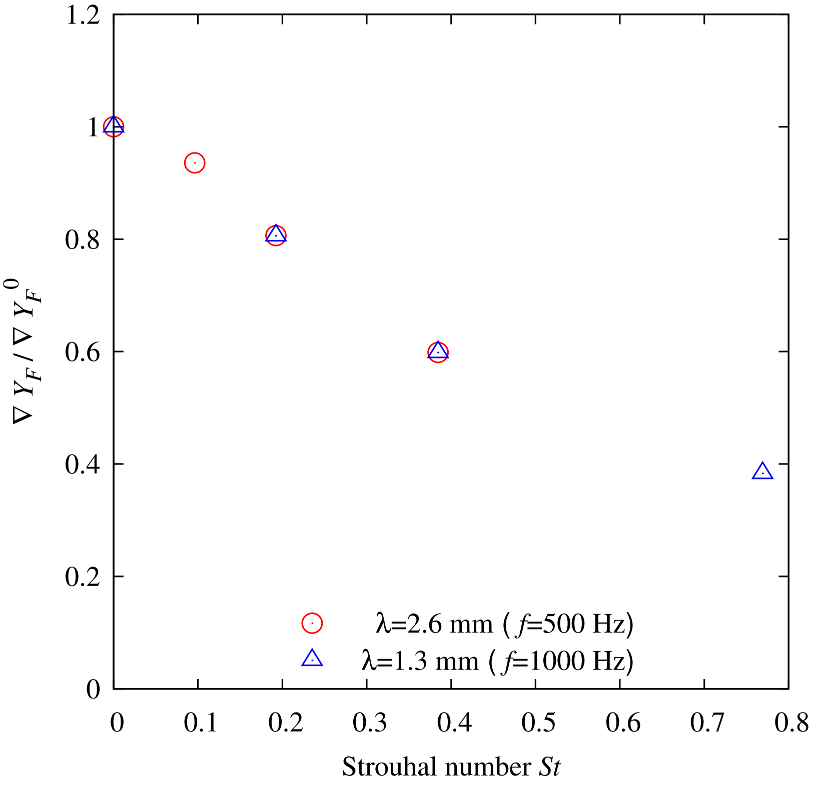

Figure 6-5-13 Normalized fuel concentration gradient obtained by the model (K=2.56)

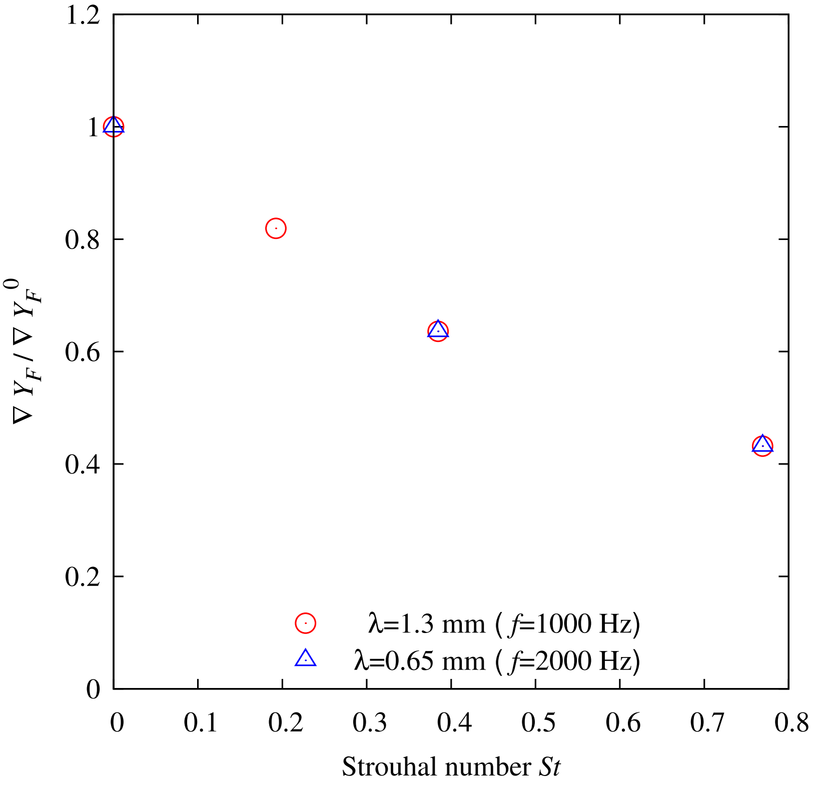

Figure 6-5-14 Normalized fuel concentration gradient obtained by the model (K=1.81)

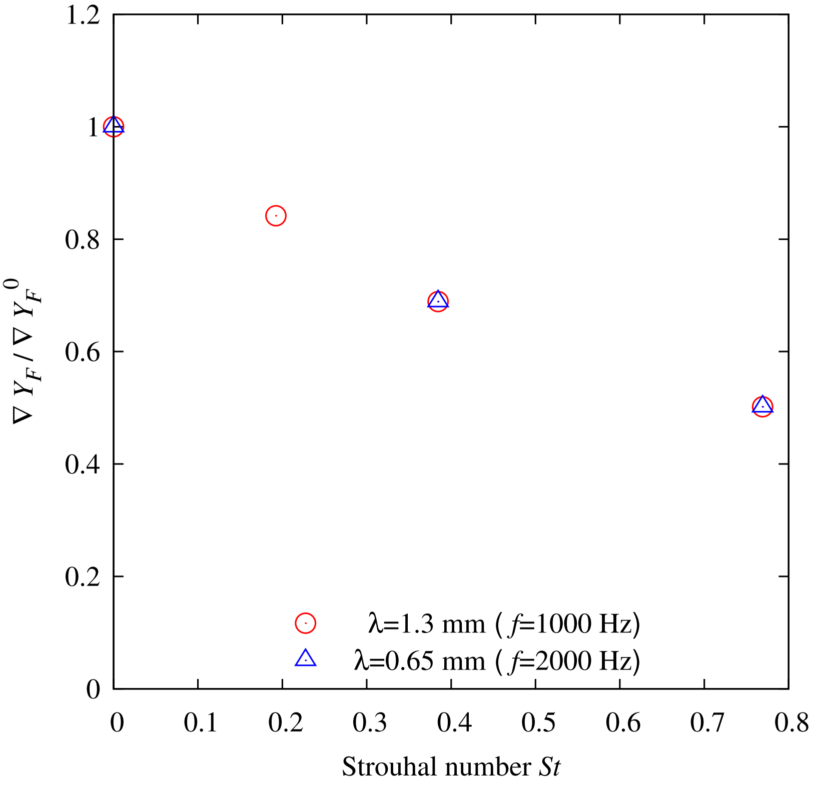

Figure 6-5-15 Normalized fuel concentration gradient obtained by the model (K=1.28)

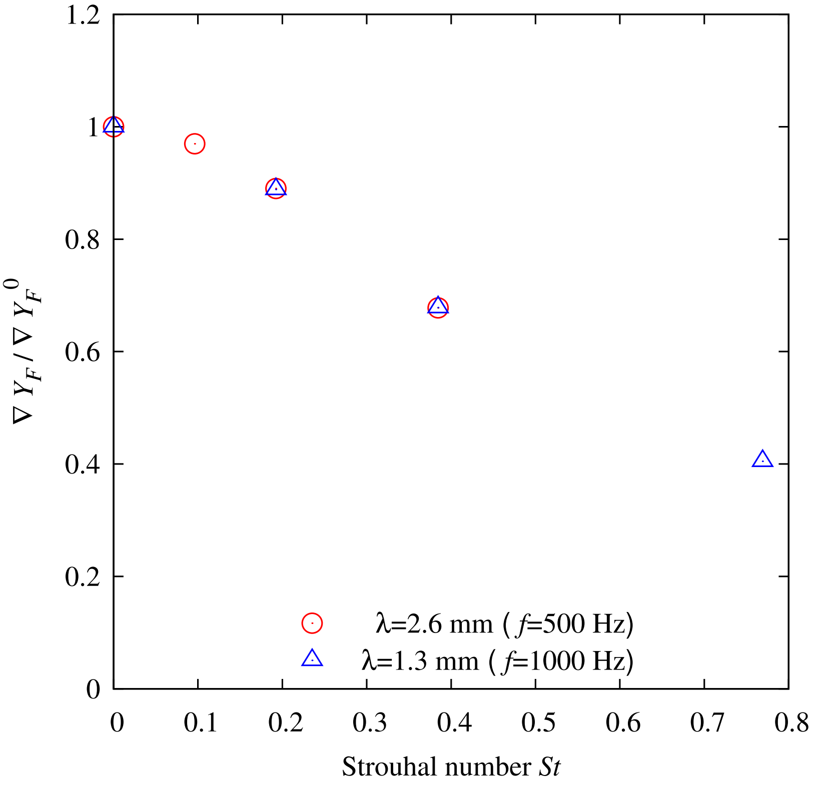

Figure 6-5-16 Normalized fuel concentration gradient obtained by numerical simulation (K=3.63)

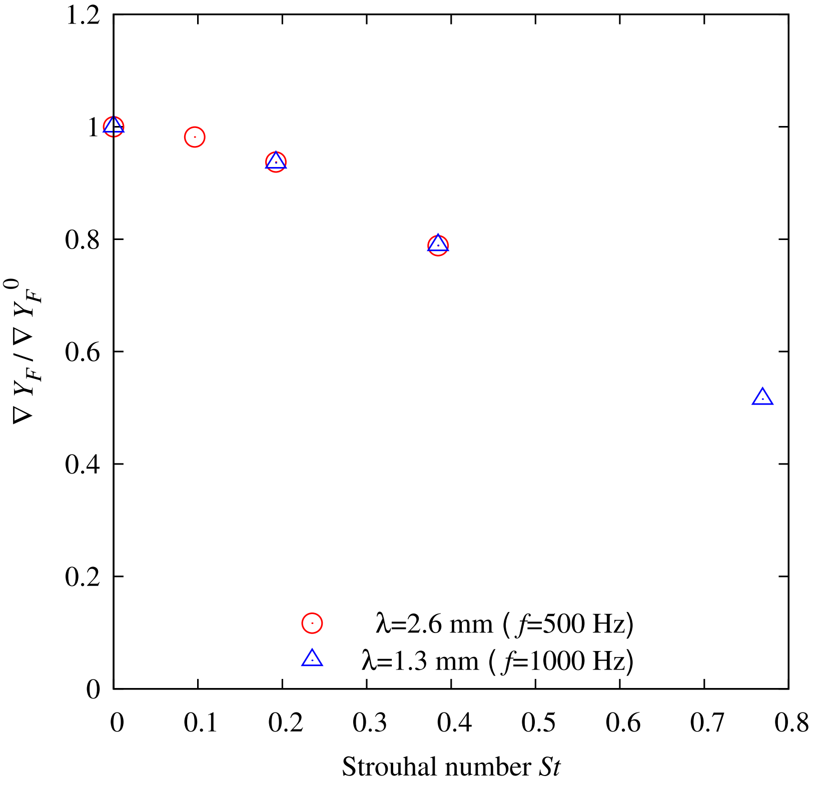

Figure 6-5-17 Normalized fuel concentration gradient obtained by numerical simulation (K=2.56)

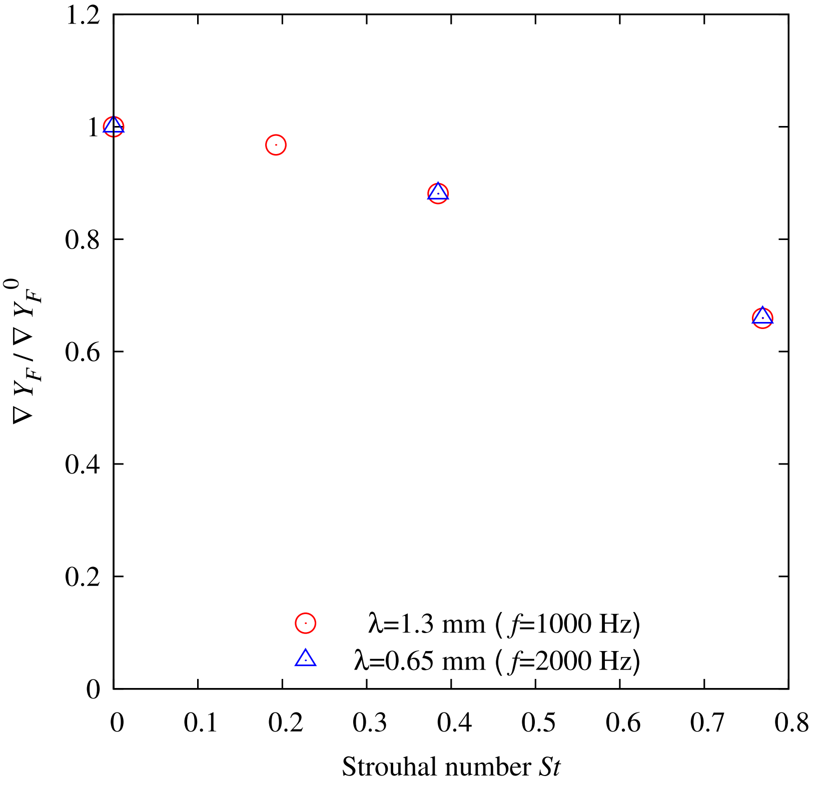

Figure 6-5-18 Normalized fuel concentration gradient obtained by numerical simulation (K=1.81)

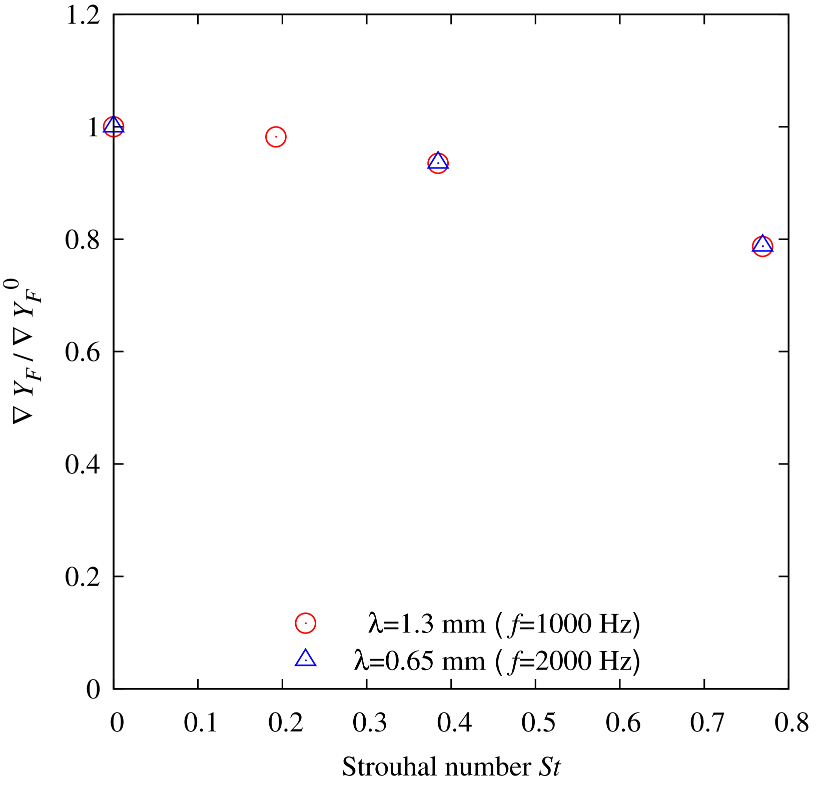

Figure 6-5-19 Normalized fuel concentration gradient obtained by numerical simulation (K=1.28)

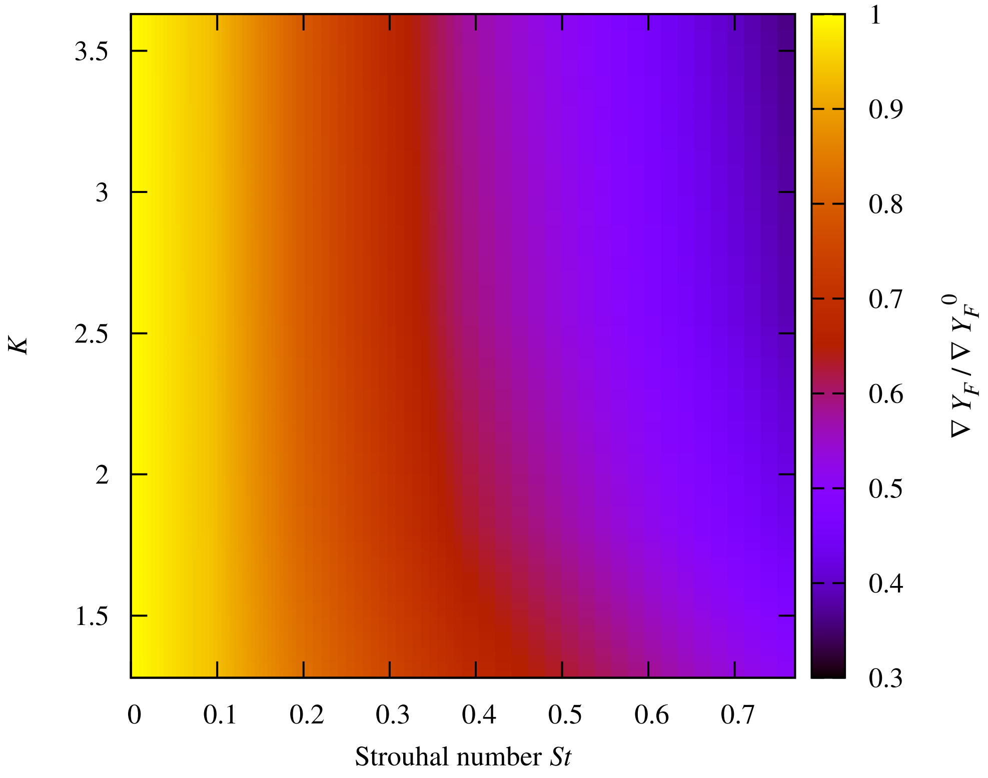

Figure 6-5-20 Contour of the normalized fuel concentration gradient obtained by the model

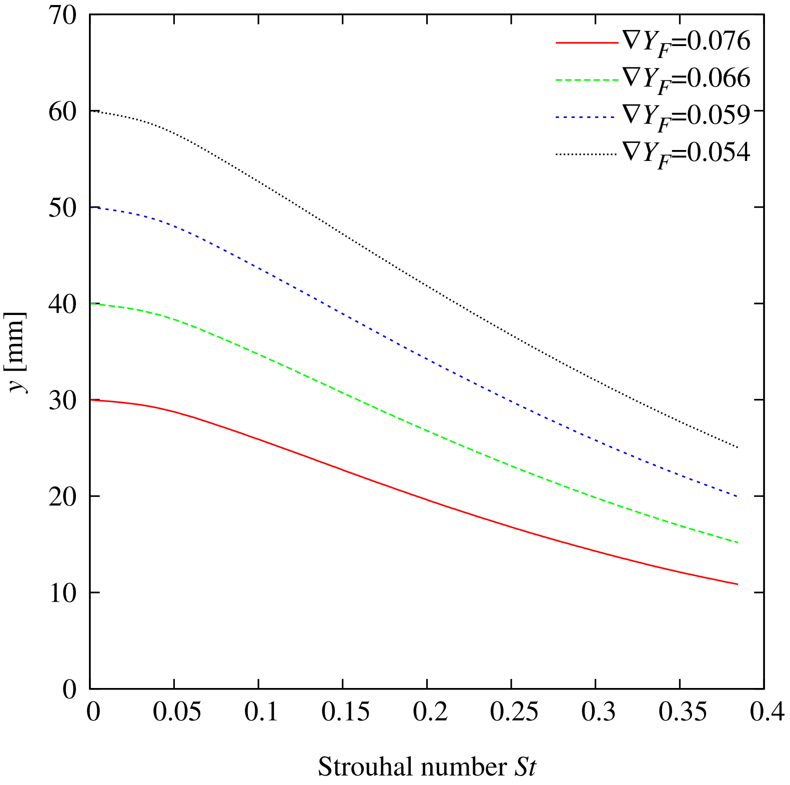

Figure 6-5-21 Locus of the iso-fuel concentration gradient with various St (Propane, ϕ=3.0)

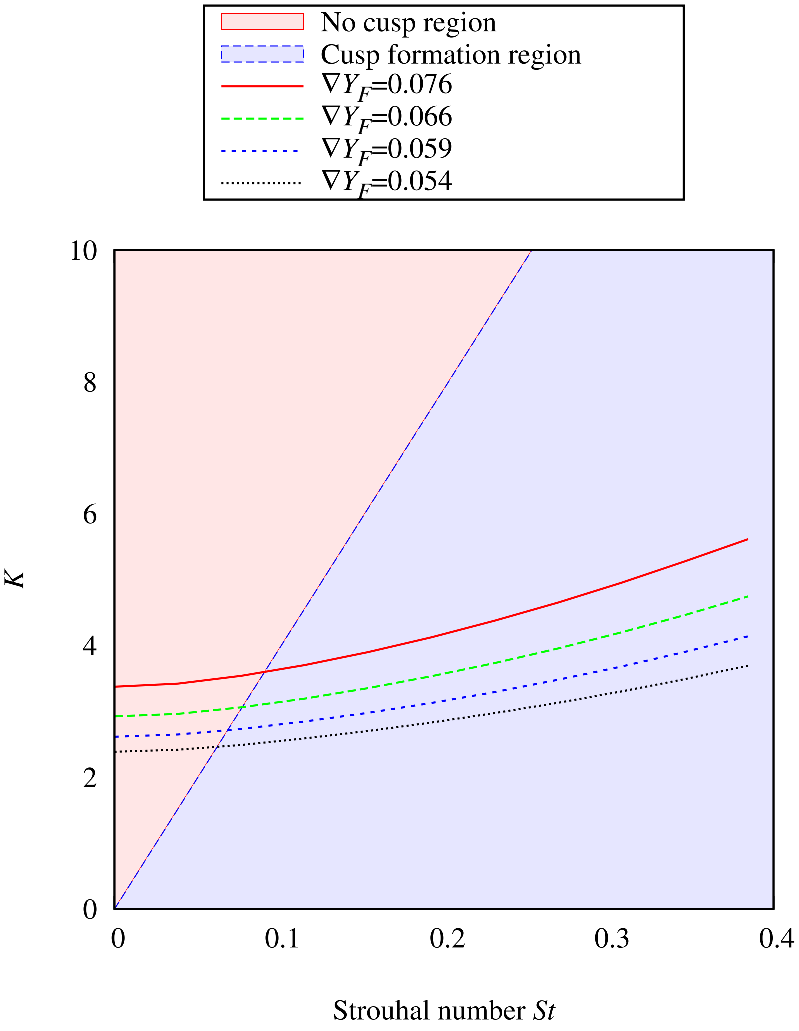

Figure 6-5-22 Locus of the iso-fuel concentration gradient with various St with $K - St$ diagram(Propane, ϕ=3.0)

Appendix A. Drawings of the test section

The drawings of the test section are shown in appendix A.

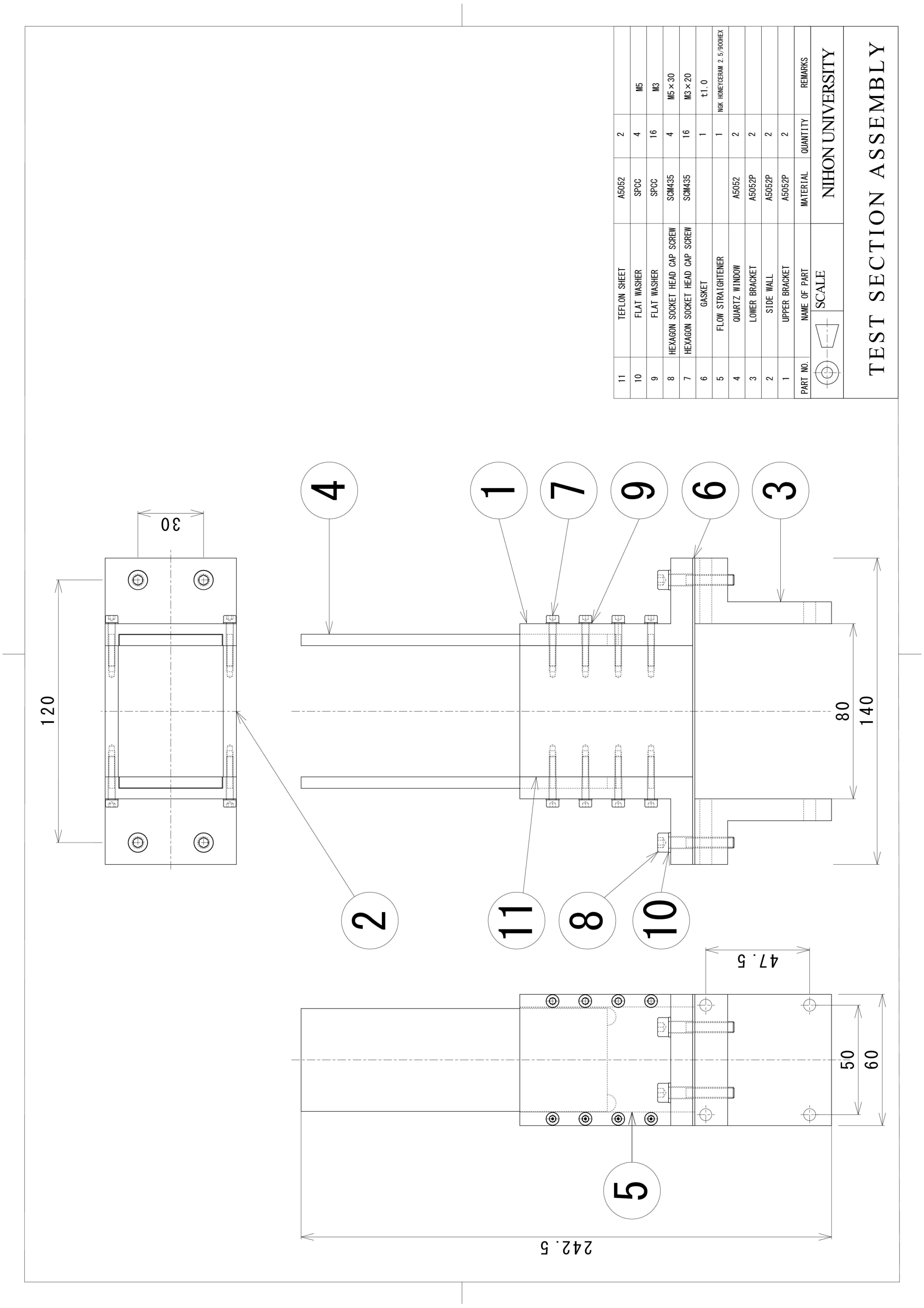

Figure A-1 Drawing of the assembly

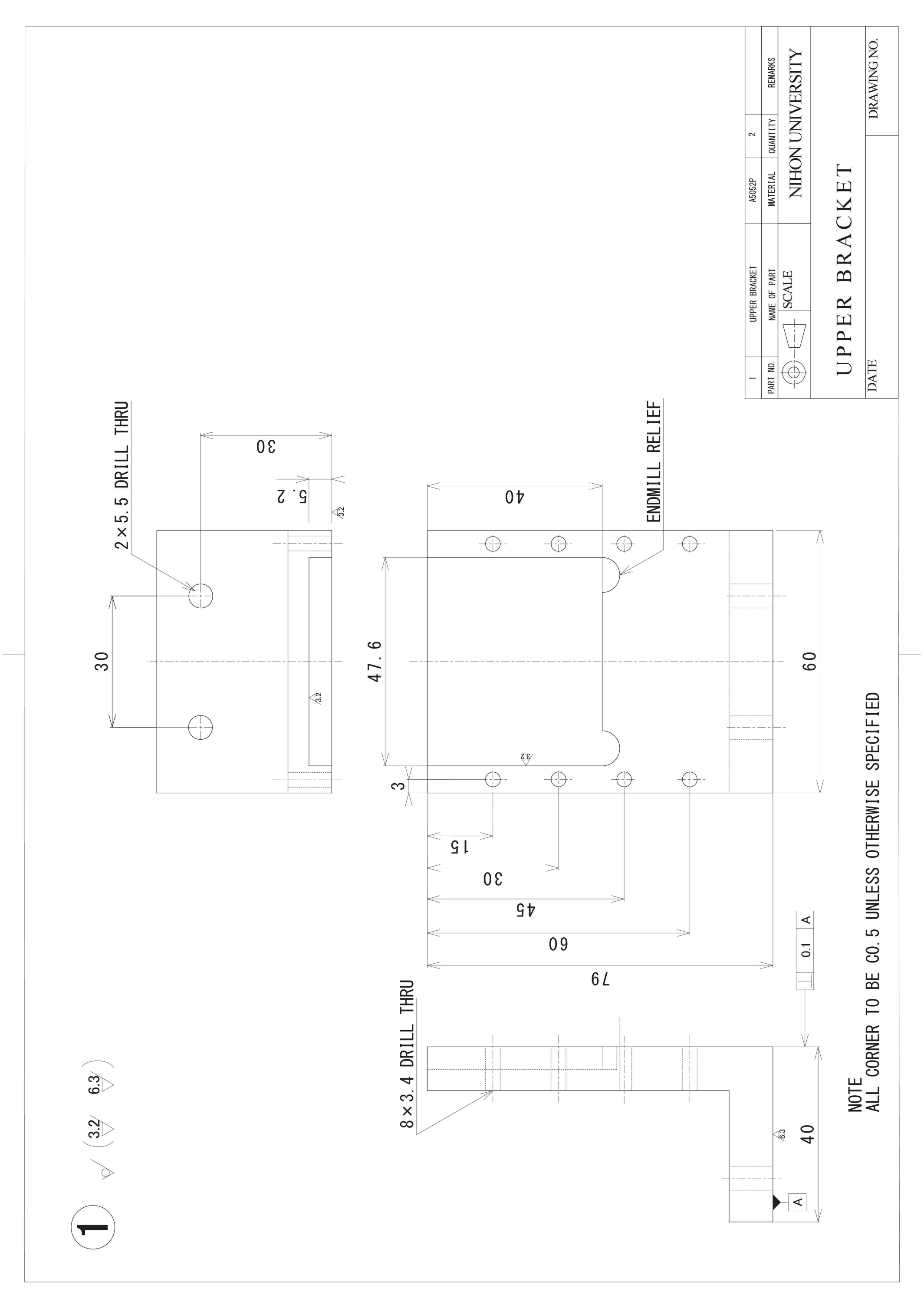

NOTE
ALL CORNER TO BE C0.5 UNLESS OTHERWISE SPECIFIED

Figure A-2 Drawing of the upper bracket

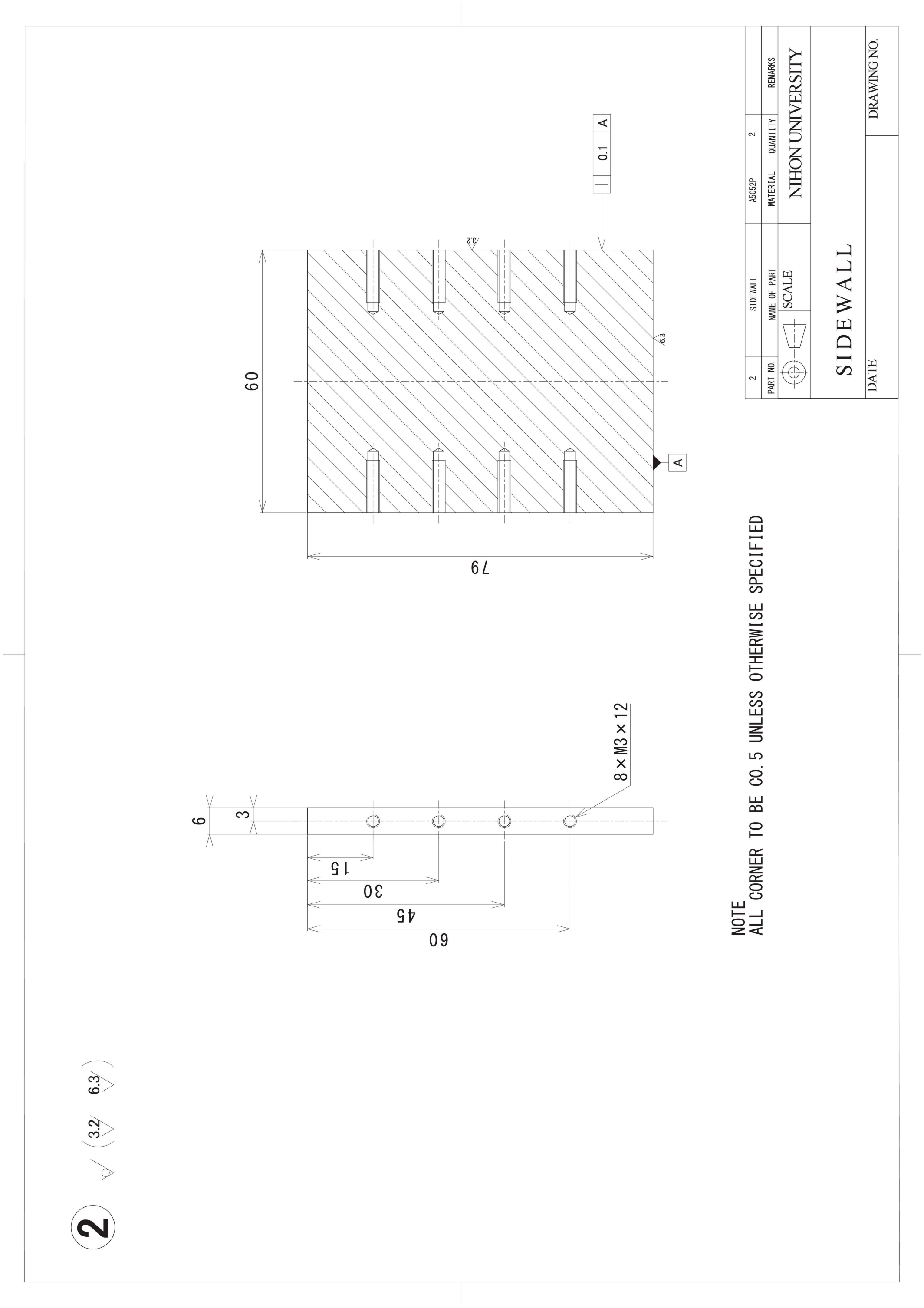

Figure A-3 Drawing of the sidewall

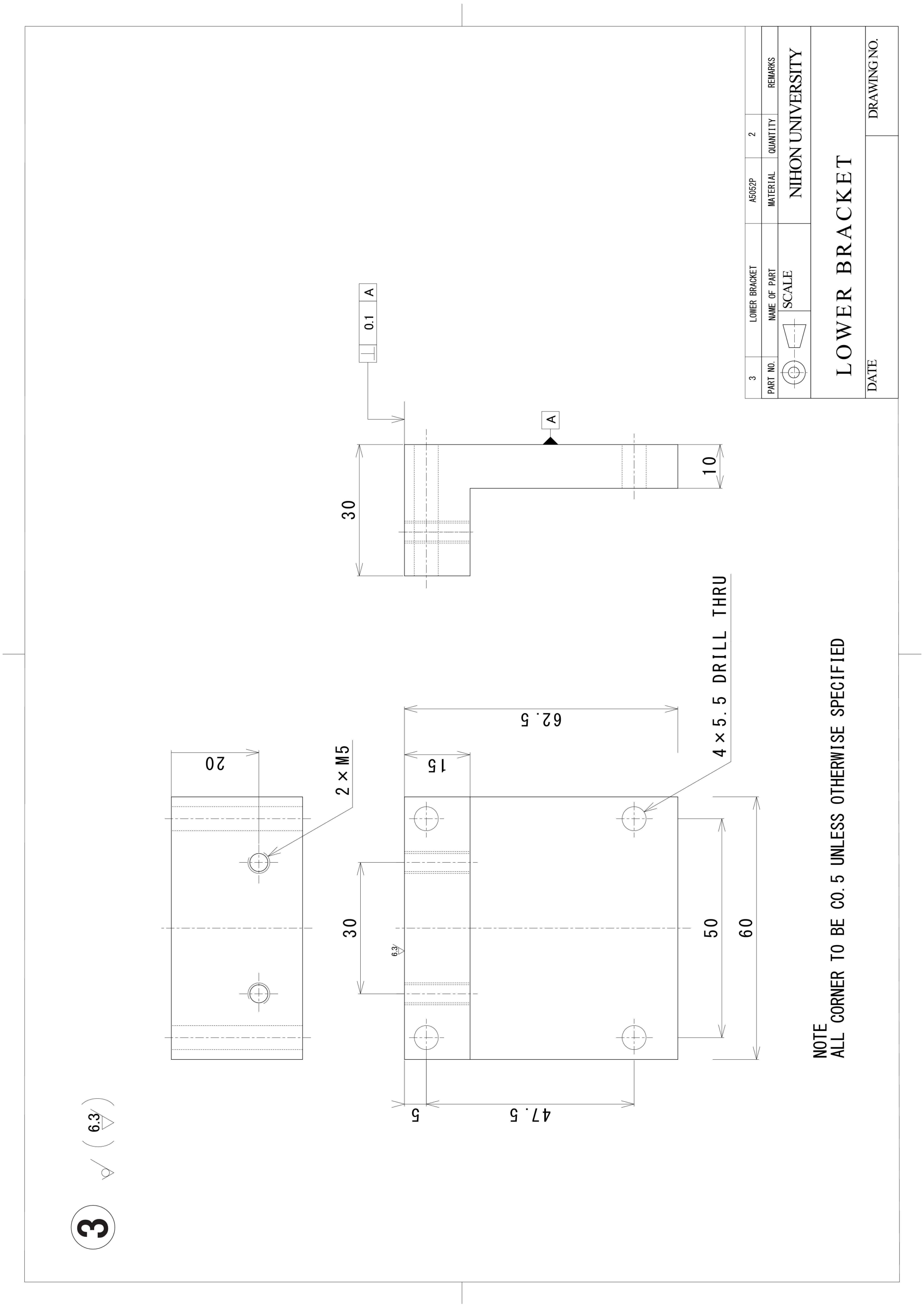

Figure A-4 Drawing of the lower bracket

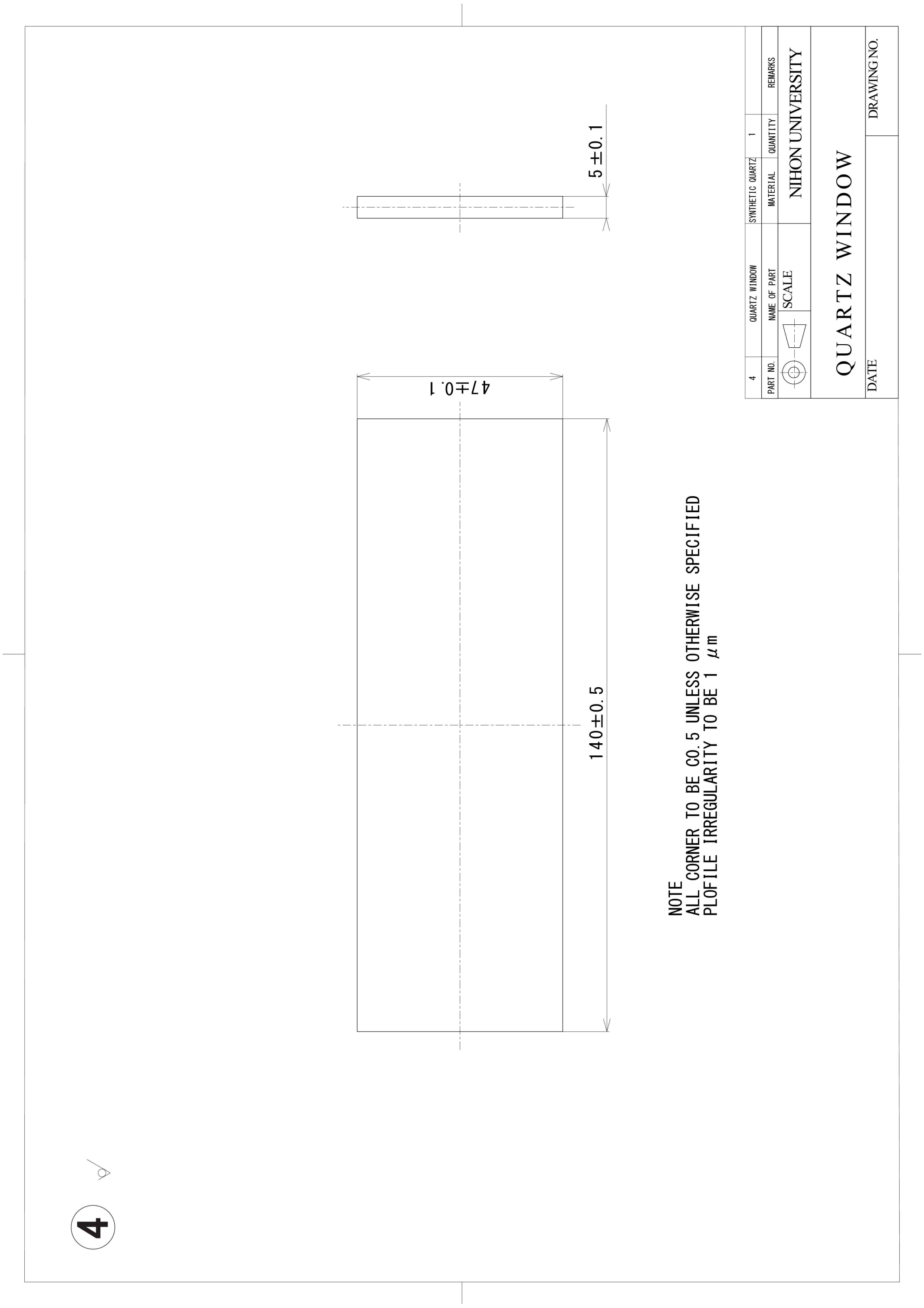

Figure A-5 Drawing of the quartz window

Appendix B. Drawings of the multi-slot burner

The drawings of the multi-slot burner are shown in appendix B.

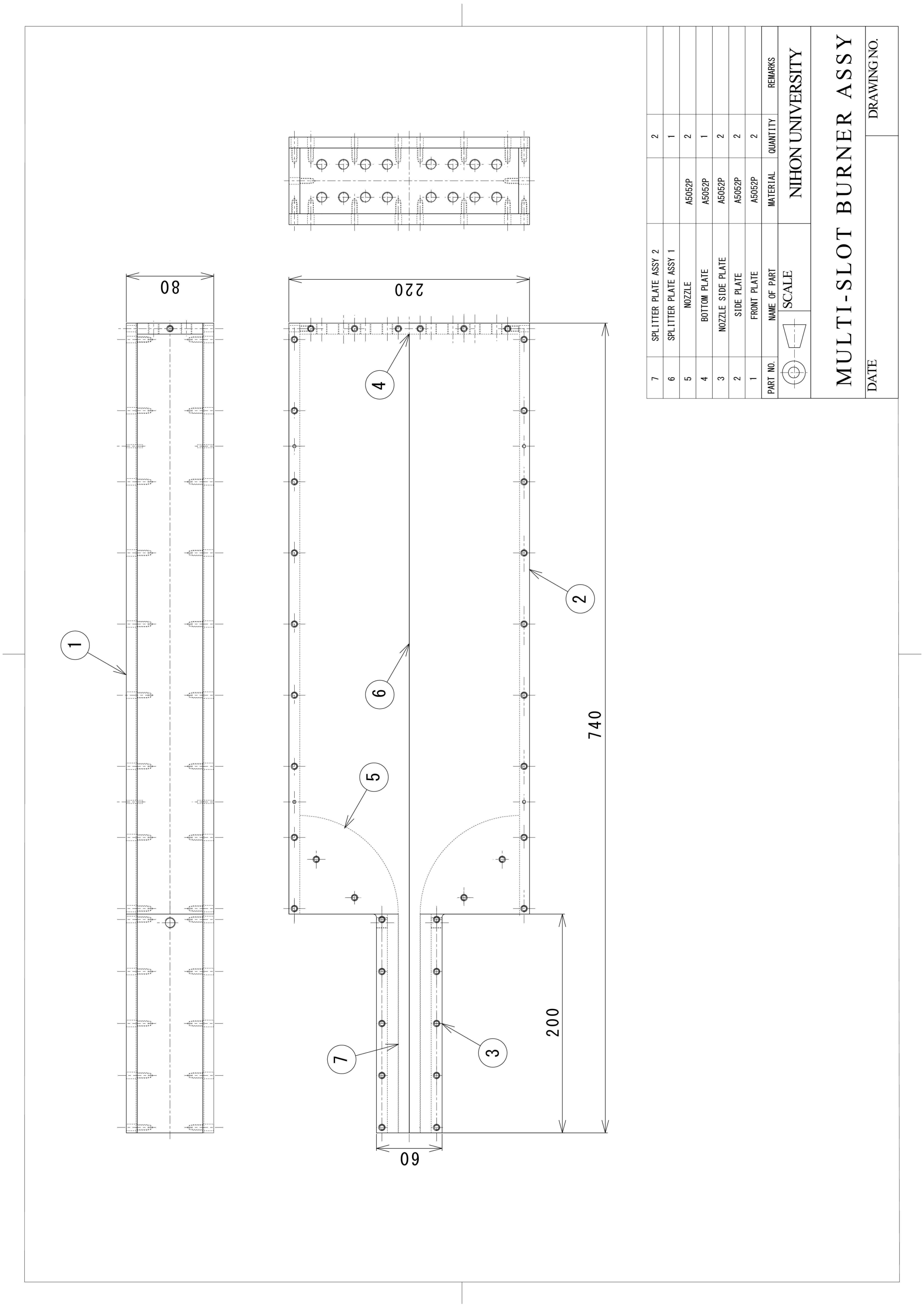

Figure B-1 Drawing of the multi-slot burner assembly

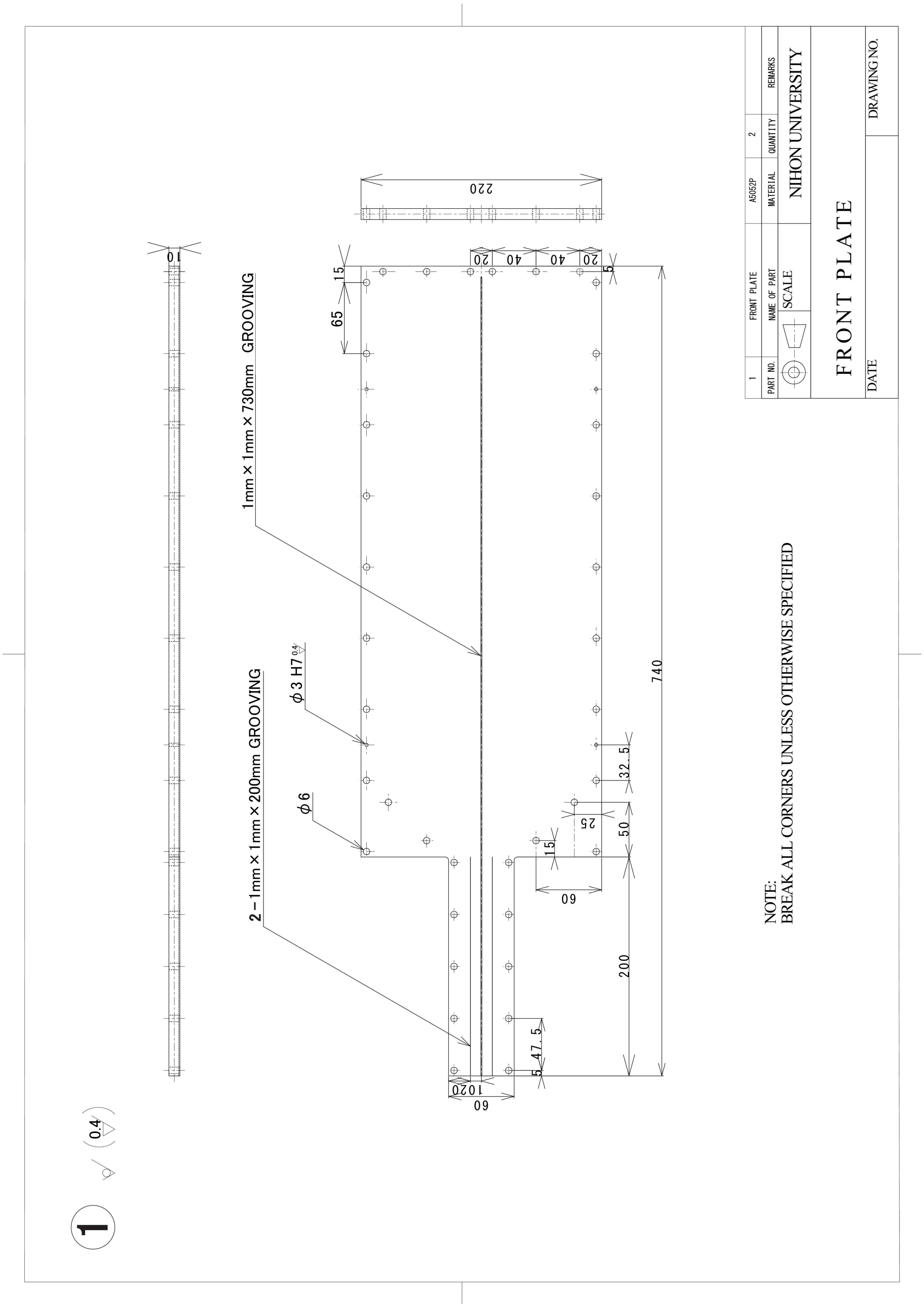

Figure B-2 Drawing of the front plate

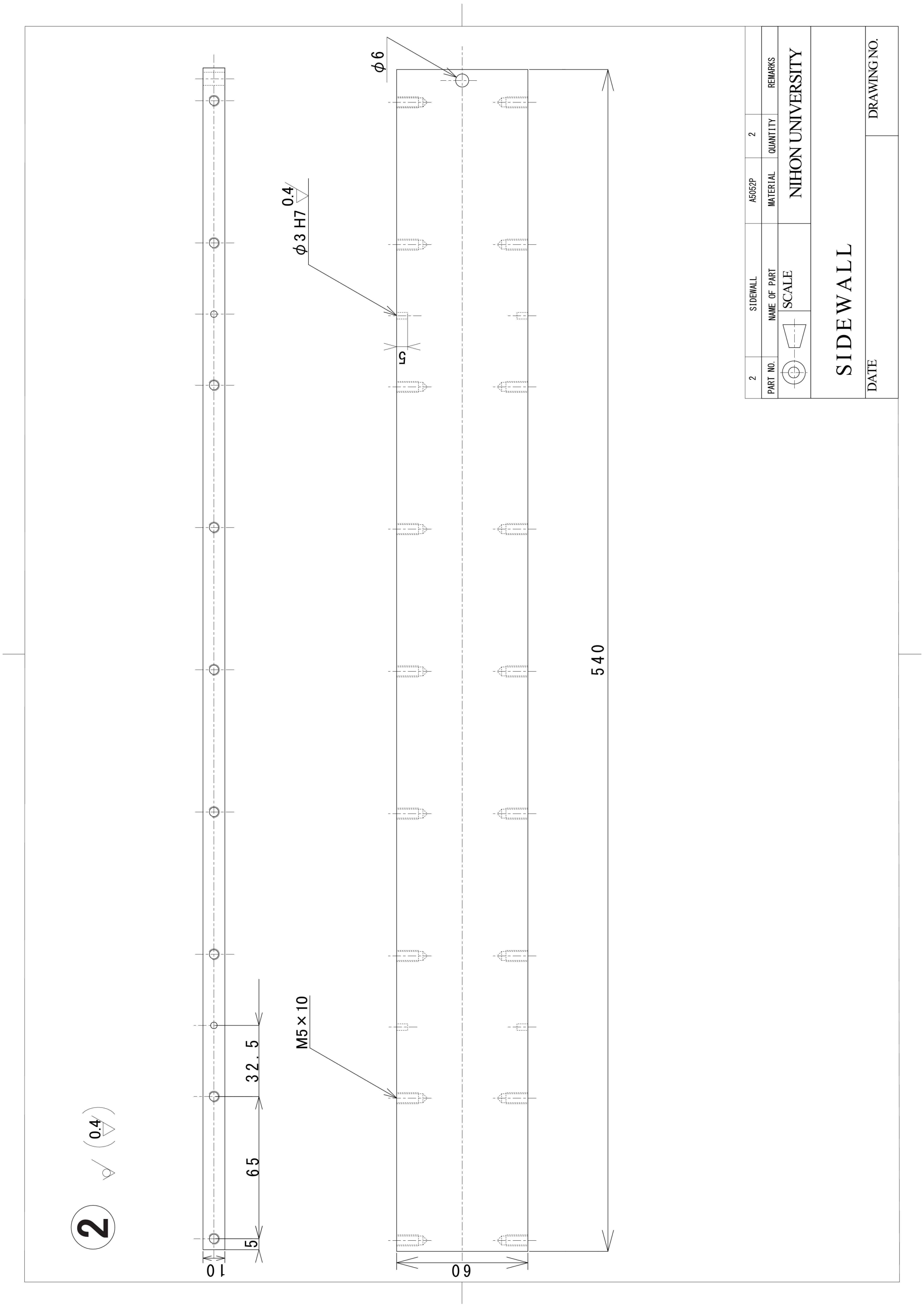

Figure B-3 Drawing of the sidewall

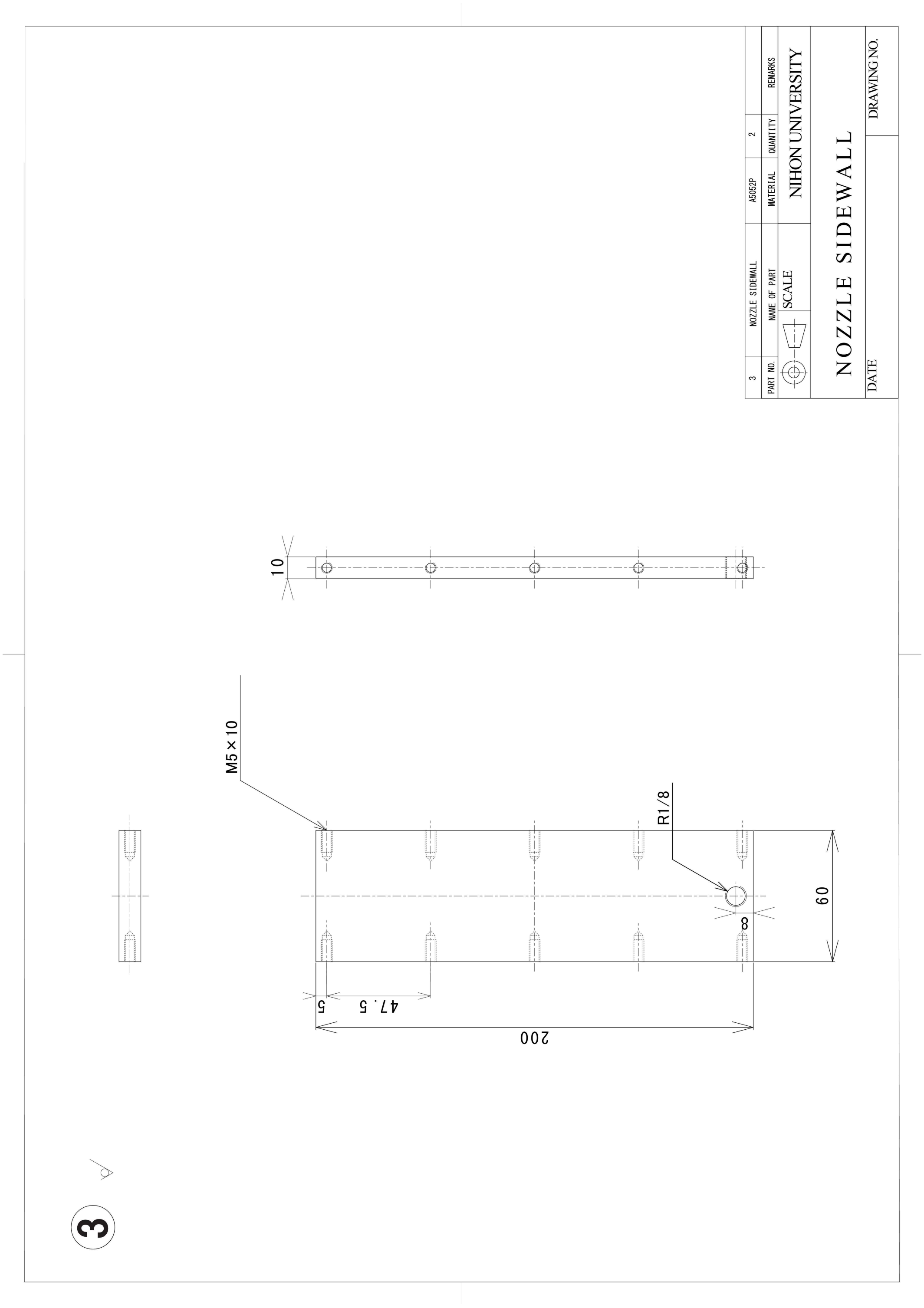

Figure B-4 Drawing of the nozzle sidewall

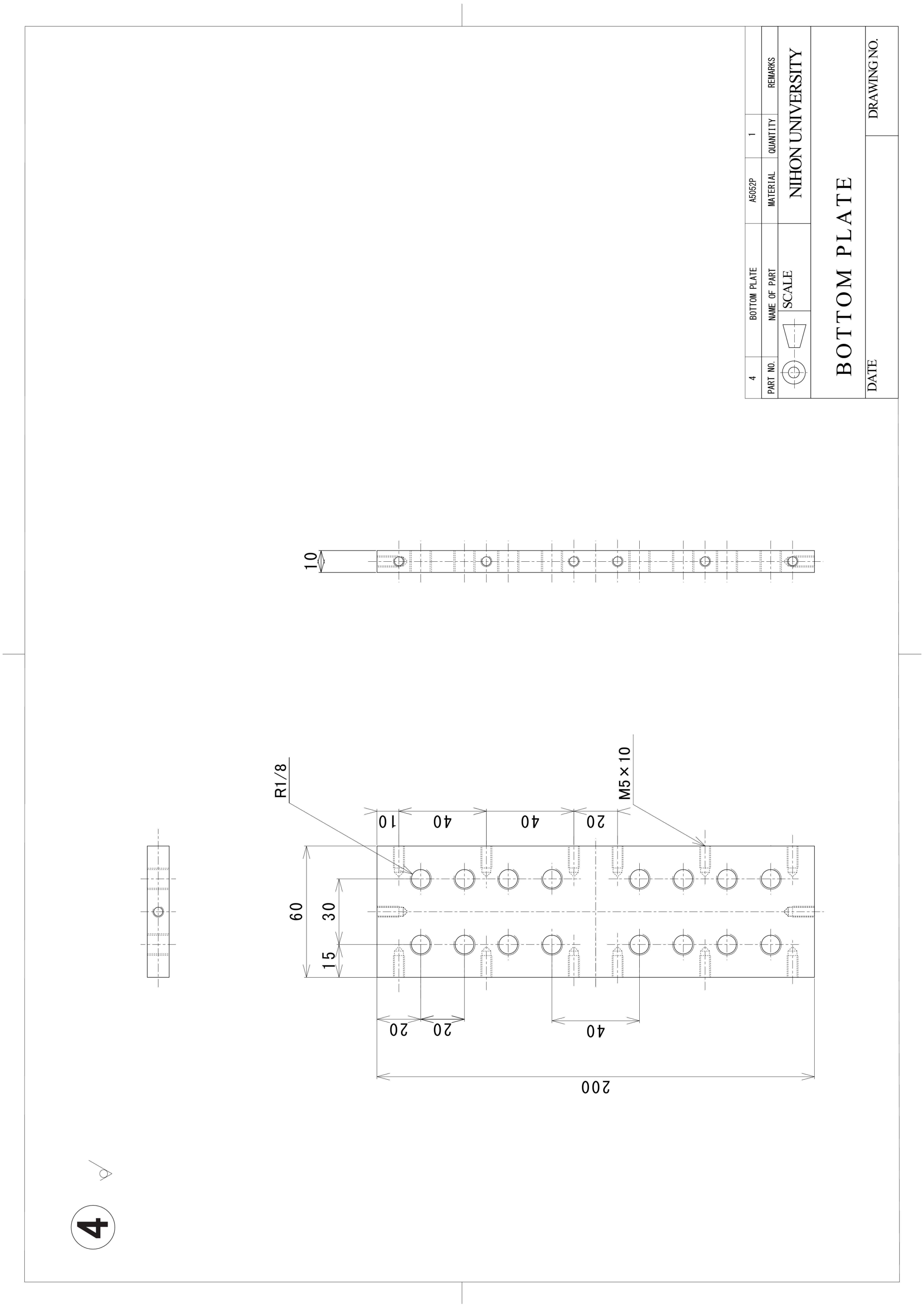

Figure B-5 Drawing of the bottom plate

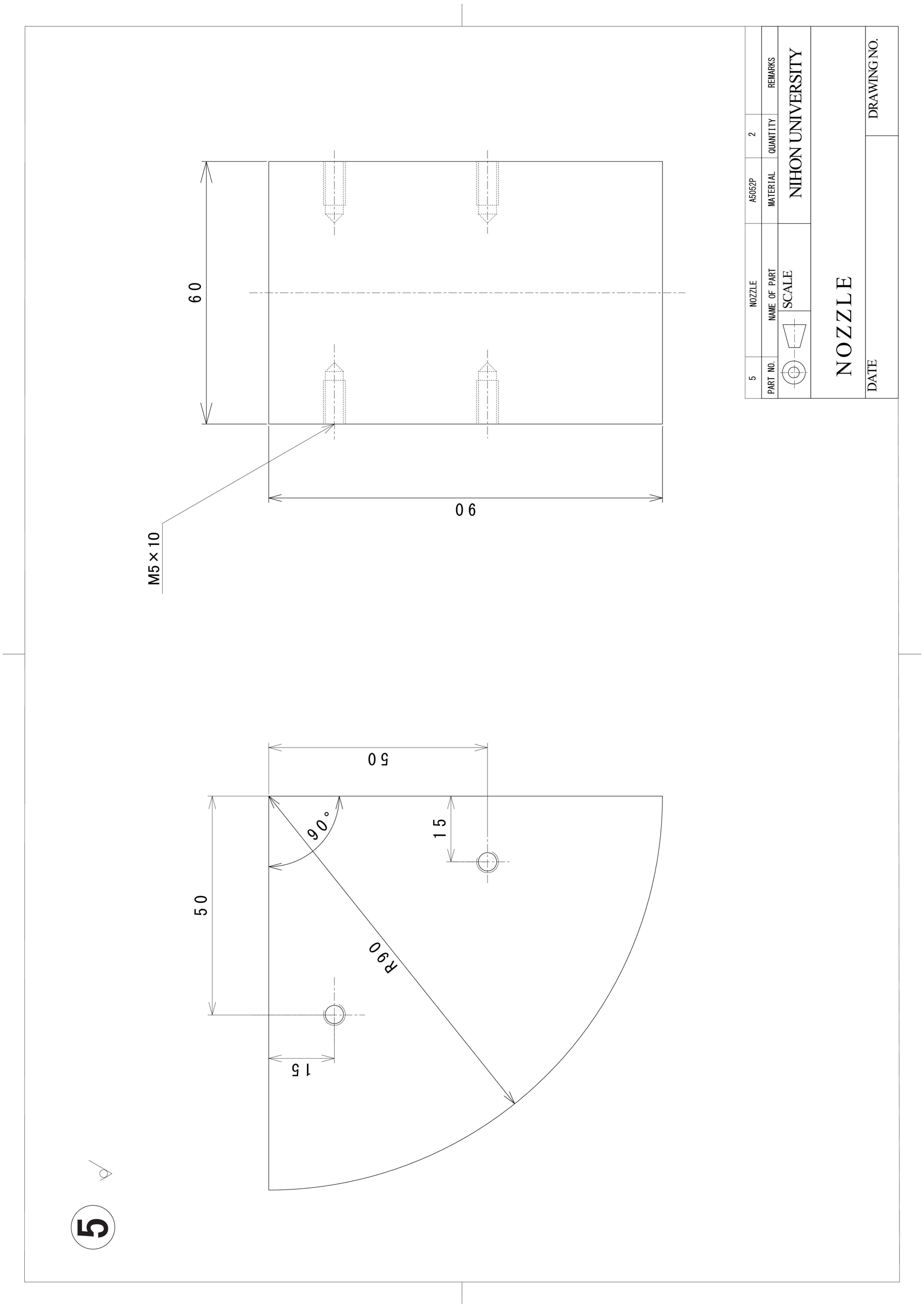

Figure B-6 Drawing of the nozzle

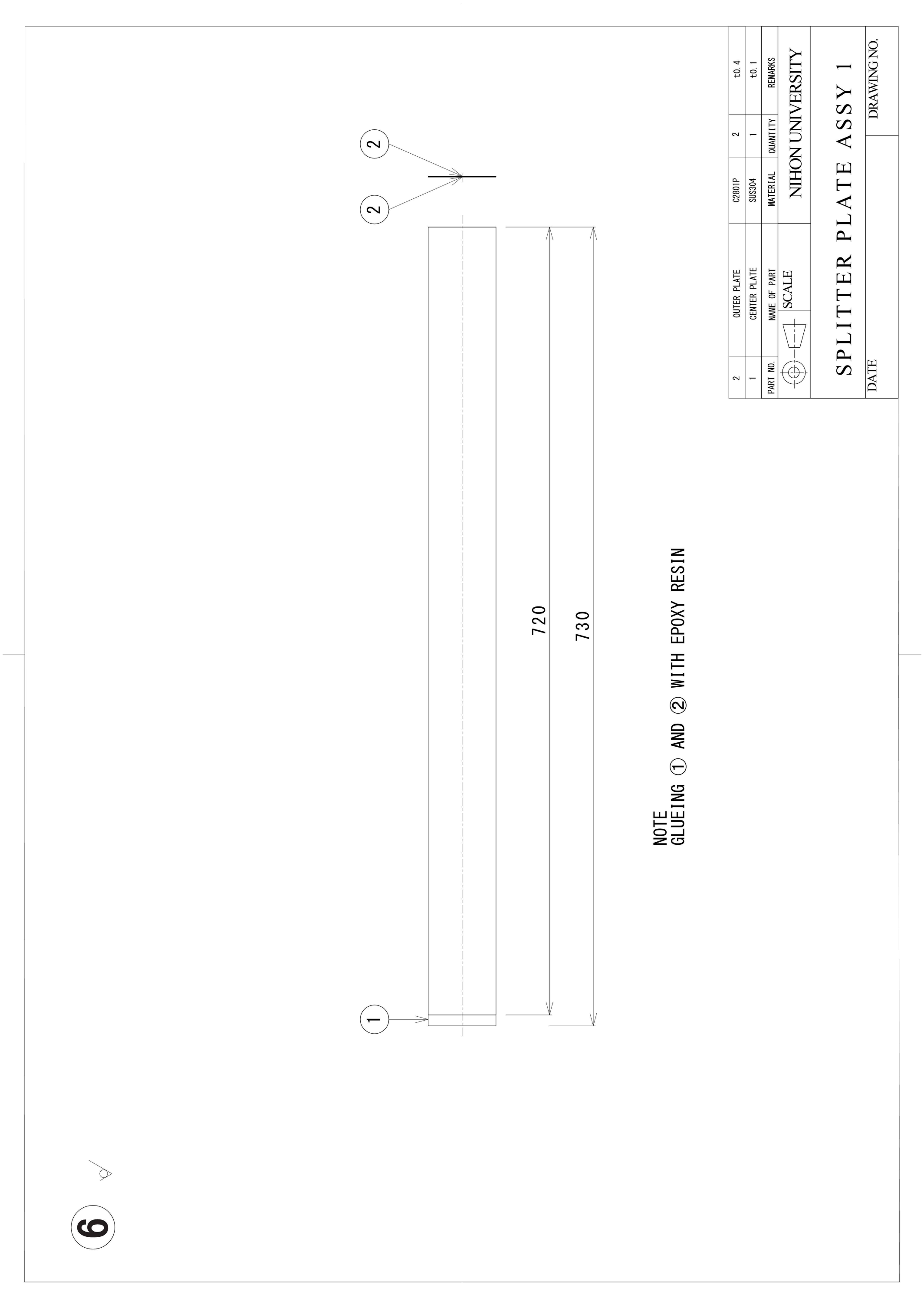

Figure B-7 Drawing of the splitter plate assy 1

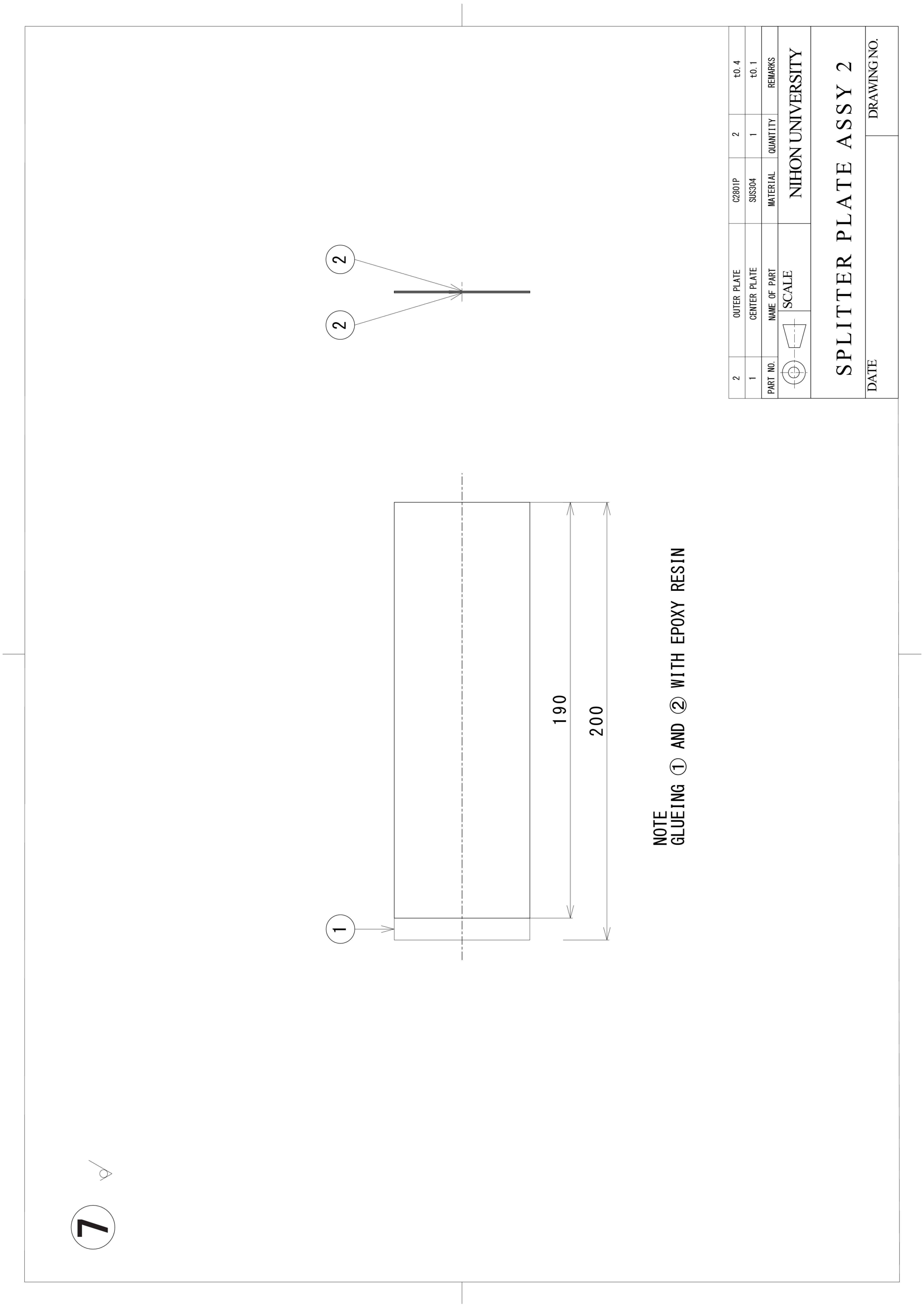

Figure B-8 Drawing of the splitter plate assy 2

Index